Enhancing Platinum-based Nanoarchitectures Electrocatalytic Activity and Durability for Oxygen Reduction Reaction at PEMFC: Investigating the Dual Role of Graphene as a Catalyst Support and a Protective Cap

A Dissertation
Presented to
The Academic Faculty

by

Ali Ahmed Abdelhafiz Mahmoud

In Partial Fulfillment
of the Requirements for the Degree
Doctor of Philosophy in the
Materials Science and Engineering

Georgia Institute of Technology
DECEMBER 2019

Enhancing Platinum-based Nanoarchitectures Electrocatalytic Activity and Durability for Oxygen Reduction Reaction at PEMFC: Investigating the Dual Role of Graphene as a Catalyst Support and Protective Cap

Approved by:

Dr. Meilin Liu, Advisor
School of Materials Science and Engineering
Georgia Institute of Technology

Dr. Sundaresan Jayaraman
School of Materials Science and Engineering
Georgia Institute of Technology

Dr. Faisal Alamgir, Co-advisor
School of Materials Science and Engineering *Georgia Institute of Technology*

Dr. Mostafa El-Sayed
School of Chemistry
Georgia Institute of Technology

Dr. Preet Singh
School of Materials Science and Engineering *Georgia Institute of Technology*

July, 31st 2019

ACKNOWLEDGEMENTS

It is my pleasure to acknowledge, Prof. Meilin Liu and Prof. Faisal Alamgir, my advisors, for their scientific and financial supports during my studies and research at Georgia Institute of Technology. I would also like to recognize my lab mates: Bote Zhao, Nicholas Kane, Luke Soule, Ryan Murphy, Ben DeGlee, Mingyu Li, Xiang Ao, Xiang Deng, Jianhuang Zeng, Adam Vitale, Parker Buntin, Chris Arnold and Hind Murad for their valuable input and stimulating discussions. Adam Vitale and NSLS-I beam line scientists at Brookhaven National Laboratory have all made significant contributions to this work via the X-ray absorption spectroscopy data collection. Dr. Ji Il Choi and Prof. Seung Soon Jang provided meaningful insights through DFT computational analysis. Additionally, I would like to thank Prof. Jamie Warner and Warner's group at the University of Oxford, Dr. Jane Howe at Hitachi, and Dr. Yong Ding at and Georgia Institute of Technology for their significant contribution through TEM imaging. Moreover, I would like to thank my coworkers: Dr. Hang Chen, Dr. Walter Henderson, Eric Woods, Todd Walters, Dr. David Tavakoli, Dr. Gary Spinner, Charlie Turgeon and Rebhadevi Monikandan at the Institute for Electronics and Nanotechnology at Georgia Institute of Technology.

TABLE OF CONTENTS

LIST OF TABLES

LIST OF FIGURES

SUMMARY

Energy demand-supply relationship is a big concern with world's consumption increased over 65% through the past two decades. Polymer Electrolyte Membrane Fuel Cell (PEMFC) possess high energy density with zero carbonaceous emissions. One of the major challenges in PEMFC is concerned with the oxygen reduction reaction (ORR) at the cathode side, where low mass activity and poor stability are key challenges to overcome. Catalyst architectures are composed of two distinctive components: catalyst material and catalyst support. Herein, our objectives are enhancing catalyst stability, catalyst-support interaction, and maximizing catalyst active surface area. In the presented thesis, strain-tuned atomically precise hybrid catalyst architectures are synthesized. Mixed single atomically dispersed up-to a few thick atomic layers Pt catalyst architecture are synthesized using electrochemical layer by layer synthesis or magnetron DC-sputtering techniques. Graphene, due to its mechanical and chemical stability, is used to demonstrating its role as a platform for Pt growth (i.e. catalyst support) and as a protective cap.

Graphene/Pt vicinity dictates Pt adatoms structure. Templated Pt adatoms growth is dictated by graphene epitaxy. TEM analysis shows ripening-free of low-dimensional Pt adatom deposited on graphene, where Pt is fully wetting graphene at ~1 nm thick layer over 1 cm^2 area. Pt/Graphene epitaxy induces compressive strain on Pt-Pt bond distance up to 4%. Compressive strain enhances ORR activity due to down-shifting the d-band center of Pt adatoms, weakens reactions intermediates adsorption at Pt surface.

Templated Pt adatoms grown on graphene shows higher stability due to covalent chemical bond formation between Pt adatoms and underlying graphene substrate. Single layer graphene utilized as a protective cap shows chemical transparency to ORR electroactivity and suppresses catalytic deactivation, wherein graphene does not restrict the access of the reactants but does block Pt from dissolution or agglomeration. Single layer graphene cap enables survival of Pt active surface area by almost zero-loss after 1K testing cycles with on observable mass activity loss within marginal error bars. Sandwiching Pt adatoms between two sets of multi-layered graphene sheets boosts ORR activity and catalyst stability. Thickness of graphene cap influences ORR activity, 3-layers graphene thick marks the threshold to observe ORR activity, where 5-layers graphene shows blockage or ORR activity. Three-layers graphene/Pt Sandwich retains 460% of ECSA after 15K testing cycles and 975% higher mass activity, compared to state-of-the-art commercial Pt/carbon catalyst. Ex-situ Raman analysis suggests catalyst degradation to occur when sufficient point defects are generated within graphene structure, through which Pt single atoms hop through towards the surface. DFT based calculations suggests that dissolution of trapped Pt adatoms at defect-center is activated by Pt clustering right underneath the defect.

CHAPTER 1. INTRODUCTION

Energy demand is immense; however, the supply is limited. The world energy consumption at 1990 was ~ 8 million tons of oil equivalent (Mtoe). On 2017, dramatic increase in energy consumption (~13 Mtoe) was recorded with an ~62.5% increase over 1990. The vast majority of the energy supply resources rely on carbon-based fuels (e.g. oil, coal and natural gas). In consequence severe global weather changes have been observed, associated with the tremendous increase in carbon dioxide (CO_2) emissions. Therefore, a dire need for a renewable, green (i.e. CO_2 emission-free) and cost-effective energy resource is a must.[1–4] Fuel cell technologies arose as a prominent candidate in this regard, where pre-stored chemical energy can be converted into electricity when demanded, with significantly higher efficiencies than current thermal-power plant or hydrocarbon-fueled engine (e.g. diesel engine) technologies. Fuel cells are classified according to the power generated, which dictates the fuel used in the electrochemical reaction, operating temperature and fuel cell design. Fuel cells operate at different temperature ranges to accommodate the energy barrier dictated by the fuel (two major temperature ranges: high (above 500 °C) and low (below 200 °C)). Fuel cell is composed of three major components:

- Anode: where fuel is fed through and oxidized
- Cathode: oxygen fed typically at the cathode for an Oxygen Reduction Reaction (ORR) to occur
- Electrolyte membrane: chemically connects anode and cathode sides of the fuel cell. Generally, fuel cell is named after the type of the membrane.

For high temperature applications, Solid Oxide Fuel Cell (SOFC) usually operates at 600-800 °C temperature range, with dedicated efforts spent to lower the operation temperature down to 500 °C.[5,6] Methane and hydrogen are typical fuels used in SOFC, where a ceramic (i.e. metal oxide) membrane is used. The high operating temperature limits SOFC to stationary applications. In additions, SOFC mostly composed of ceramic materials, where cracking is a major threat.[6] Therefore, electrical energy generated has to be stored in batteries, when energy is demanded for mobile applications (i.e. vehicles: automotive or airplanes). Batteries resemble another viable option for energy , where electrical power can be stored in a form of chemical energy, which is converted electrochemically to electricity when needed. Current battery technologies have major challenges to overcome regarding limited capacity, safety, low efficiency to store electricity for prolonged times and slower charge up rates.[7,8] In addition, battery costs 40-50% of hybrid vehicles run with electricity and use batteries as a power source (e.g. Tesla), however, the transportation aptitude is limited well-below 400 miles.

Low temperature fuel cells operate between 70-200 °C, with the vast majority below 100 °C, rise as prominent candidates to replace batteries for mobile applications. The first effort, famously powered Apollo spacecraft, was Alkali fuel cells (AFCs). Alkali fuel cells uses alkaline solution as an electrolyte (e.g. KOH), where the power output is limited to 3 KW. AFCs operates at 150-200 °C temperature range, while recent efforts developed alkaline-based solid polymer electrolyte to replace liquid electrolyte, however enhancing its conductivity and durability are still challenges to overcome. The low power output and relatively higher operating temperature hinder the spread out of AFCs' technology. Another candidate based on methanol liquid as a fuel is Direct Methanol Fuel Cell

(DMFCs). Operating at slightly lower temperature compared to AFCs, DMFCs operate with methanol fuel which fed at the anode side, where an oxidation reaction occurs; decomposing methanol into CO_2 and H_2. Hydrogen ions transport through a membrane towards the cathode. One of the major shortcomings of DMFCs is methanol crossover towards the cathode. Hence, at the cathode, a complex oxygen reduction and methanol oxidation take apart where the overall cell efficiency drops. One of the possible solutions to limit methanol crossover is to increase the thickness of the electrolyte membrane, which in return increases the ohmic resistance and lower the cell efficiency.[9]

Proton Exchange Membrane Fuel Cell (PEMFC), however possesses challenges, still captures a tremendous interest as a potential clean energy source at lower operating temperature (typically 80 °C). The lower operating temperature enables PEMFCs for cold startup, in addition to faster refueling compared to batteries. Moreover, lower temperature results in slower wear rates to fuel cell components, which relatively boosts its lifetime and endurance. PEMFC have tremendous potential to be the preferred power sources for mobile applications due to the aforementioned advantages, in addition to their high efficiency, high energy density, low to zero carbonaceous emissions and fast start-up and shut-down capability. PEMFC runs through two half reactions: hydrogen gas oxidation at the anode side into protons (H^+) which transports through a Nafion polymeric membrane towards the cathode. At the cathode, oxygen is reduced with H^+ forming water, as the product of the reaction.[9]

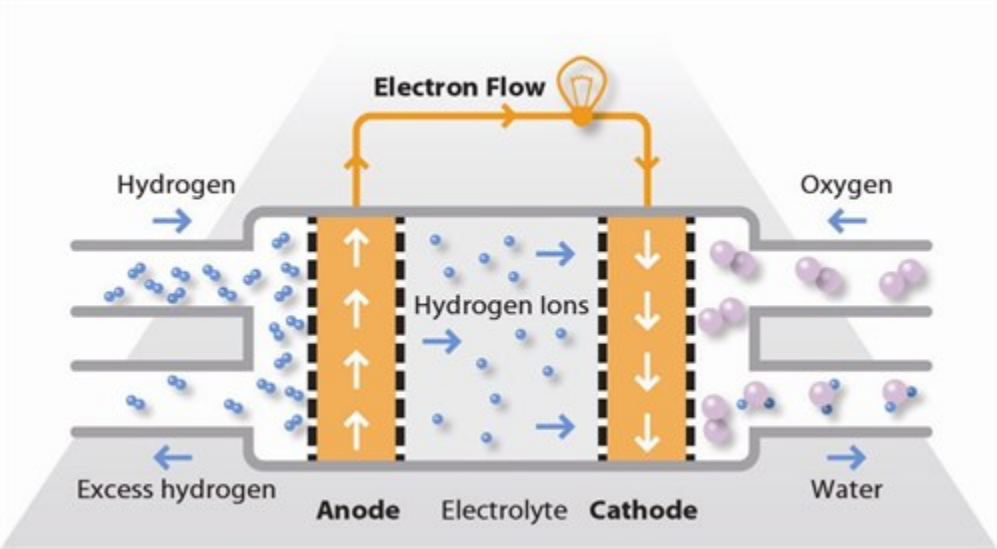

Figure 1: Polymer Electrolyte Membrane Fuel Cell (PEMFC)[9]

Oxygen reduction reaction (ORR) is a typical reaction at the cathode side of PEMFC, which suffers from sluggish kinetic rate. The catalyst of choice for ORR at PEMFCs is platinum and its group metal (PGM). Typically, Pt catalyst is supported on carbon-black which suffers from low corrosion resistance, limiting down the overall Pt/carbon catalyst stability.[10] The cost of the Pt-based catalyst alone constitutes over 40% of the fuel cell stack cost. Therefore, enormous efforts have been devoted to reduce the high cost of catalyst while enhancing its lifetime and overall activity.[11,12] Three main challenges have captured the focus to overcome the commercialization problem of PEMFC: enhancing catalytic activity, catalyst durability and cost reduction.

Enhancing Pt catalyst mass activity (i.e. activity per catalyst loading) has been approached from different directions, however the main focal point to capitalize was strain tuning. Research efforts have been devoted to synthesizing ultra-small Pt nanoparticles with high active surface area. Nanoparticles with high density of steps and kinks possess

higher catalytic aptitude due to localized compressive strain induced at the particle's surface. In addition, synthesis of core@shell structures showed significant effect on ORR activity. Pt monolayers grown on top of different metals suffer from mechanical strain, which is dictated by the underlying substrate. Compressive or tensile strain can be induced according to the lattice mismatch between core and shell materials. [13–18] Nevertheless, the big dilemma of using homogeneous or core@shell structures is limited stability at ORR conditions. Two major factors govern catalyst lifetime: support and catalyst stabilities. Commercial carbon black is a conventional catalyst support used for ORR. Commercial carbon degrades at low pH and high oxidizing potentials, leaving holes within the support structure. Hence, catalyst agglomeration is activated, and surface area is lost. On the other hand, catalyst materials themselves are unstable. Sources of catalyst instability can be seen through particles dissolution in the electrolyte due to poor interaction with the support (i.e. commercial carbon black) or particles ripening where surface area is lost. Moreover, core@shell structure suffers from evolution of core atoms to the surface, where Pt electrochemical active surface area (ECSA) is reduced. Therefore, a need for a sharp well-controlled interface between core and shell materials is desirable. Another dilemma is the phase segregation of Pt-based alloy nanoparticle, which can happen during heating for prolonged periods in typical PEMFC working conditions, losing the synergetic effect from alloying.[19] Therefore, another effective strategy to reduce the Pt particle size and improve the Pt dispersion and utilization is the development of a proper carbon support. In particular, graphene has attracted much attention due to its unique properties, including high conductivity, large surface area, and intrinsic catalytic activity along edge planes and defects.[10,20,21]

In the presented thesis herein, we envision to study the effect of using graphene as a catalyst support and a protective cap for atomically dispersed metal atoms. Graphene has a unique 2D crystal structure which is thoughtful to provide a template for Pt adatom epitaxial growth. Pt epitaxial growth can possess interesting mechanical strain which leads to unprecedented catalytic aptitude. Moreover, due to graphene's mechanical robustness and chemical stability, masking catalyst adatoms with a layer of graphene can enable desired stability to prevent catalyst adatoms dissolution, while withstanding harsh acidic environments and oxidizing potentials. Moreover, graphene's super-aromaticity can provide faster charge transfer than commercial carbon black, in addition to forming a hybridized catalyst with Pt adatoms, where ORR can occur through graphene cap without observing an additional energy penalty.[22]

In the presented thesis herein, we are providing a fundamental understanding of using graphene as both a catalyst support and a protective cap for atomic scale Pt adatom. Fundamental analysis of the dimensional effect of graphene, Pt and graphene/Pt interaction haven been investigated in correlation to their effect on ORR activity. Finally, an optimized structure has been demonstrated with tremendous activity and stability enhancement. Graphene capping enabled 460% and 975% of catalyst stability and mass activity, respectively, when compared to state-of-the-art Pt commercial catalyst (HISPEC4000). Optimal graphene thickness was demonstrated to be 3-layers thick where thicker graphene showed ORR inactivity.

CHAPTER 2. THEORETICAL BACKGROUND

The Sabatier principle draws a roadmap in electrocatalysis by highlighting two of the major steps in catalyzing a chemical reaction. According to Sabatier's, interaction between catalyst materials and reaction species has to be right. An optimum catalyst will bind neither too weak (to give ability to adsorb reaction species firmly to the catalyst active site), nor to strong (to enable facile desorption of products after reaction is completed). Binding affinity between catalyst and reaction species is a function of several factors, primarily the catalyst material, as will be discussed in detail at the literature review section. Guided by Sabatier principle, two fundamental points have to be clarified: a cause of ORR dilemma "reaction overpotential" and an explanation of ORR catalytic enhancement at the enlightenment of "D-band center position theory".[23]

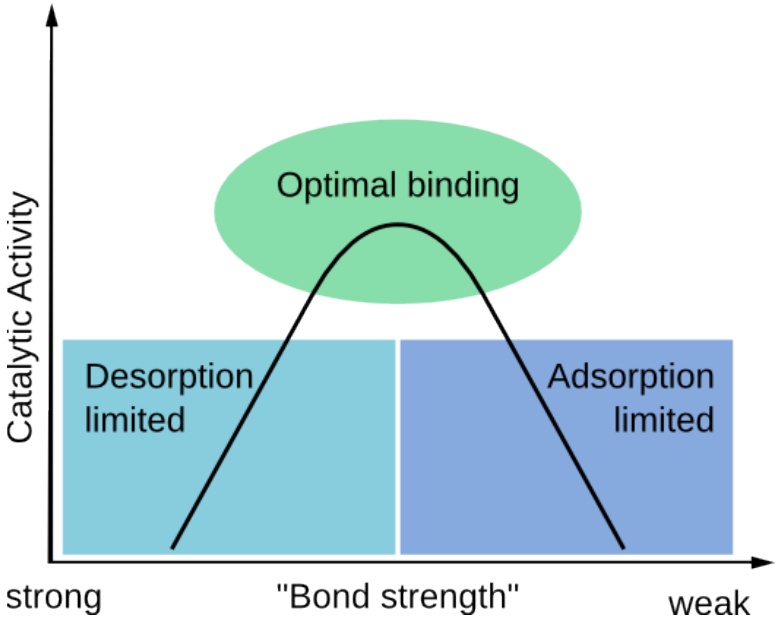

Figure 2: Sabatier principle illustrating reaction rate limiting steps

2.1. Origin of ORR overpotential

For an electrochemical cell, two half reactions occur at the anode and cathode electrodes, separately. Thermodynamics, ignoring loses, quantify the potential of the cell where both reactions are in equilibrium with each other (i.e. cathodic and anodic currents, due to electrochemical reactions, are equal). If the rate of reaction at one electrode is higher/lower, then, the cell deviates from equilibrium conditions. Hence, cell potential (measured experimentally) consequently is different from the predicted potential by thermodynamics. The potential difference between those two cases is the overpotential. Overpotential represents the activation energy barrier for a reaction to occur. The value of overpotential is an explicit comparison showing an easy or difficult reaction pathway. Therefore, a catalyst material is needed to reduce the overpotential. Overpotential is affected by the pH of the reaction medium, reaction environment, reaction species concentration (e.g. oxygen-rich or depleted), reaction temperature and surface chemistry at which reaction occurs. Oxygen reduction reaction (ORR) is a typical reaction at the cathode side of PEMFC. ORR has a sluggish kinetics, compared to the anode side reaction (i.e. hydrogen protonation). Two ORR pathways are proposed in the literature: 4-electrons and 2-electrons pathways. Till the moment, the exact ORR mechanism of the 4-electrons pathway has not been confirmed, rather, two general models are presented: dissociative and associative reaction mechanisms.

2.1.1. Four-electron associative mechanism

The model predicts the oxygen reduction to occur after dissociation of reaction intermediates (i.e. oxygen). Following, are equations representing the proposed mechanism steps: starting with an oxygen molecule dissociation into oxygen atoms and bounds to the catalyst surface (eq.1). Followed by two successive reduction steps when oxygen and hydroxyl react with a proton, eq. 2&3, respectively. An asterisk (*) resembles an active site to which reaction intermediate is bounded at the catalyst surface.[23]

$$\frac{1}{2}O_2 + * \rightarrow O^* \quad (1)$$

$$O^* + H^+ + e^- \longrightarrow OH^* \quad (2)$$

$$OH^* + H^+ + e^- \longrightarrow H_2O + * \quad (3)$$

Nosrskov et al, using DFT calculations, provided an insight about the rate limiting step and overpotential origin. The free energy for the proposed dissociative mechanism steps were calculated at three different cell potentials (i.e. 0, 0.78 and 1.23 V vs RHE) and two oxygen surface coverages (i.e. 0 and 50% surface coverage by a monolayer of oxygen molecule) on Pt (111) surface. Results showed an uphill free energy diagram for steps denoted by equation 2 and 3 for a potential of 1.23V (i.e. spontaneous water dissociation potential). At a potential of 0.78V, an important mark of the maximum positive potential at which all the reaction steps are exothermic (i.e. downhill free energy), which is denoted as the “limiting potential”. The potential window between 0.78:1.23 V resembles the overpotential regime where research efforts have been subjected to narrow down. DFT calculations suggested that both 2nd and 3rd reaction steps have similar activation barrier at

V=1.23, suggesting that both oxygen hydrogenation and OH striping are the reaction rate limiting steps.[23]

However, at 0.78V all reaction steps are exothermic, assuming that Pt surface is oxygen-free (i.e. all the Pt active sites are free for oxygen-bounding). Assuming 50% coverage of Pt active sites by oxygen atoms, switched the oxygen-hydrogenation (i.e. OH formation at step#2) to an uphill free energy step (i.e. activation barrier exists). Rate constant represented by the current density ($i_{(u)}$) of the reaction is given by eq.4, where the availability of catalytic active sites per unit area ($\frac{N}{A}$) is directly proportional to reaction kinetics (k_o) at a given potential (U). The more available sites, the higher the current density is, and the favorable the reaction kinetics will be. Therefore, blocking the catalytic active sites by pre-adsorbed reaction intermediates is a crucial factor that determines the overall reaction kinetics, as will be discussed later explaining the "Sabatier principle".[23] The aforementioned finding suggested that OH liberation is the rate limiting step for catalyst surfaces that bound strongly to oxygen, while oxygen adsorption is the rate limiting step for catalyst that bound loosely to oxygen.

$$i_{(u)} = 2e\,\frac{N}{A}\,k_o\,e^{\frac{\Delta G(U)}{KT}} \qquad (4)$$

2.1.2. Four-electron associative mechanism

The second reaction pathway is the associative mechanism, where oxygen molecule is hydrogenated without breaking O=O bond. Reaction pathway is presented at eqs. 5-9, with eqs. 8-9 are similar to eq. 2-3 of the dissociative mechanism. DFT calculations showed that

the associative mechanism showed same behavior as the dissociative mechanism at the same given potentials.[23] Therefore, no consensus have been established about the existing of one mechanism over the other.

$$O_2 + * \rightarrow O_2^* \quad (5)$$

$$O_2^* + H^+ + e^- \rightarrow H_2O + OOH^* \quad (6)$$

$$OOH^* + H^+ + e^- \rightarrow H_2O + O^* \quad (7)$$

$$O^* + H^+ + e^- \rightarrow OH^* \quad (8)$$

$$OH^* + H^+ + e^- \longrightarrow H_2O + * \quad (9)$$

2.1.3. Two-electron mechanism

Reaction mechanism is a function of catalyst surface (e.g. Pt-Hg_4 and Pt(111) promote the 2 and 4-electron pathways, respectively) or reaction medium (e.g. H_2SO_4 and $HClO_4$ electrolytes promote the 2 and 4-electron pathways, respectively). Thermodynamics equilibrium conditions are established, which marks the 2 and 4-electron reactions to occur at 0.7 and 1.23V vs RHE, given that energy loses are totally absent. Two-electron pathway involves only two reaction steps with H_2O_2 as the oxygen reduction product. However, both 4-electron associative and 2-electron mechanisms involve the formation of OOH* as a reaction intermediate, but H_2O_2 is selectively the reduction product only if the formation energy of OH is more favorable than the dissociation of O=O. For surfaces that bond weakly to oxygen (e.g. Au), oxygen liberation from the surface is easier than O=O bond breakage. Therefore, hydrogenation of OOH* is the reduction product (i.e. H_2O_2).

Hydrogen peroxide is harsh and considerably destructive to the catalyst surface. Therefore, the 4-electrons mechanism is more favorable than the 2-electron reaction pathway.[24]

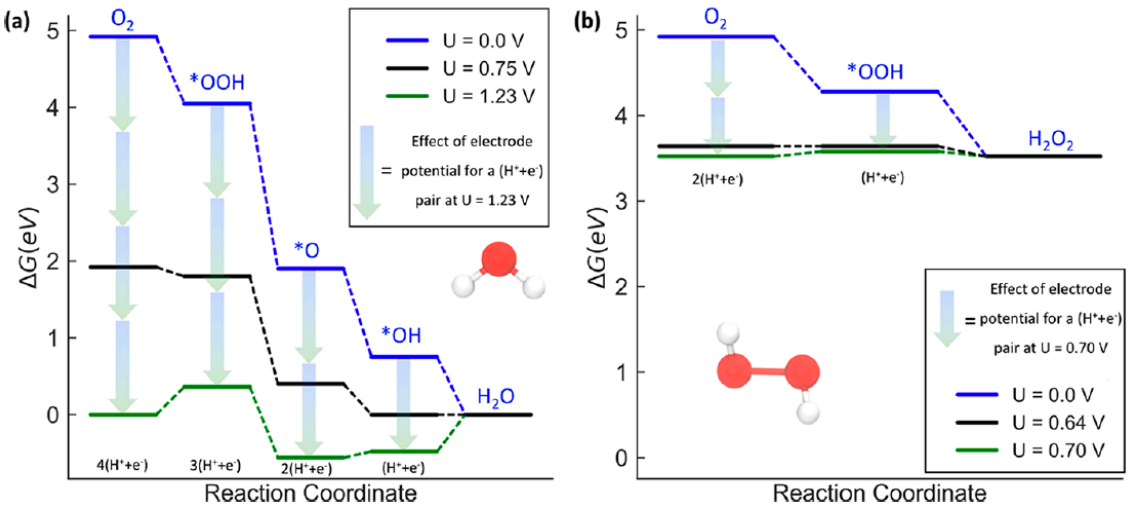

Figure 3: Free energy diagram representing associative ORR mechanism (a) 4-electron pathway on Pt(111) surface (b) 2-electron pathway on Pt-Hg_4 surface. Anode electrode is referenced to RHE (i.e. 0V vs RHE), where measuring the cathode potential represents the full cell potential.[24]

2.2. D-band center theory

Adsorption of molecules on catalyst surface alters the electronic structure of the catalyst materials. Pt as a metal has an electronic structure of [Xe] $4f^{14}$ $5d^{9}$ $6s^{1}$. Adsorbates interact with the 5d orbitals of Pt, forming a hybridized bonding (d-σ) and anti-boding (d-σ*) bands according to molecular orbital theory (MO). The bonding and anti-bonding straddles the Fermi level. The bonding states of the d-band of Pt-adsorbate are be fully

filled, however the anti-bonding is partially or fully filled. The local electronic structure of the catalyst surface (i.e. density of states (DOS) of the near surface atoms) dictates the filling of the anti-bonding band, and so the interaction between catalyst and adsorbate. According to the band order shown at eq 10 (N resembles number of electrons in each state), the larger the value, the more stable the bond between the molecule atoms is and vice versa. Therefore, more filling of the anti-bonding states translates into more repulsion between the two bonded atoms.[25]

$$Band\ Order = \frac{1}{2}\left(N_{bonding} - N_{anti-bonding}\right) \quad (10)$$

In terms of ORR, as denoted earlier by Sabatier principle, the interaction (i.e. weak or strong) between catalyst (e.g. Pt) and reaction intermediates (e.g. O, OH, OOH) has to be optimal. At the enlighten of d-band center position, catalyst-adsorbate interaction can be correlated to ORR activity in general, and overpotential specifically. For a down-shifted d-band center away from the Fermi level, this indicates a high-filling of the anti-bonding states, suggesting a weaker interaction between catalyst and adsorbate. On the contrary, a higher d-band center correlates with less-filled anti-bonding states. This suggests that catalyst-adsorbate is less destabilized (i.e. more stable). Therefore, the interaction between metal and adsorbate is stronger. Hence, ORR overpotential increases, as more energy is needed to liberate the reaction intermediate for oxygen reduction completion. Several research efforts have been directed towards altering the d-band center position through changing the catalyst electronic structure, as will be discussed in detail at the literature review section.[26]

Experimental tools could be difficult to determine the filling extent of the anti-bonding orbitals, while determining the location of the d-band center (i.e. an imaginary location describing the position of the center point between bonding/anti-bonding relatively to the Fermi level) is plausible to unravel this dilemma. X-ray photoelectron spectroscopy (XPS) is a surface analysis technique, however, the x-rays are highly powerful, where core-electrons are excited. To unravel the position of the d-band center, only the position of the outer most electron-shell is desirable (i.e. valence band). Therefore, ultraviolet photoelectron spectroscopy (UPS) is a better candidate, as UV photons are less powerful and barely excites electrons from the valence band. UPS signal is weaker and the difference in energy of valence electrons is very small. Therefore, a bright and sharp energy source, in addition to a highly sensitive detector are needed, which can be performed using a synchrotron energy source.[27]

CHAPTER 3. LITERATURE SURVEY

3.1 Catalyst aspects governing ORR activity

3.1.1 Catalyst materials

According to the Sabatier principle, a major key is the interaction between catalyst material and its support (i.e. substrate), which could alter the structure, chemical and/or electronic state of the catalyst. As described earlier, ORR is a sluggish reaction with multiple electrons (i.e. 4 or 2) steps are involved in the reaction. Nosrkov et al, two decades ago, investigated the ORR mechanism over close packed slabs of pure metals (e.g. Pt, Ni, Au, Rh, Ir, Cu). Ni showed ~ 3 times higher affinity to adsorb oxygen to its surface for dissociation (i.e. O_2 bond breakage into O^- for reduction), however, this resulted in a much stronger energy barrier for OH^- formation and desorption, compared to Pt. Au showed a negative free energy of formation for all the reaction steps after initial oxygen adsorption/dissociation, but the oxygen adsorption step itself has a positive free energy, indicating poor intimacy between O and Au. DFT calculations scanned metal catalysts at two sides of the reaction spectrum (i.e. too weak or too strong); presenting a strong oxygen adsorption (e.g. Ni, Fe, Mo) and weaker adsorbent (e.g. Au, Ag). Figure 4 showing a volcano type plot, resembles at the right-side a weaker affinity to adsorb or an easy desorption of reaction species, and vice versa at the left side. More interestingly, authors reported, according to the dissociative mechanism that after hydrogen bonding to oxygen, OH^- tends to bond more strongly to metal surface (e.g. Pt, Ni or Au). To date, Pt is the best pure element to fulfill Sabatier's principle at the top of the volcano, with the least overpotential needed to overcome the energy barrier for ORR. Authors investigated the

associative mechanism, where an oxygen molecule binds to hydrogen without O_2 bond breakage. Similar trend for a volcano-type relation was generated, with Pt at the top of the volcano hill as well.[23]

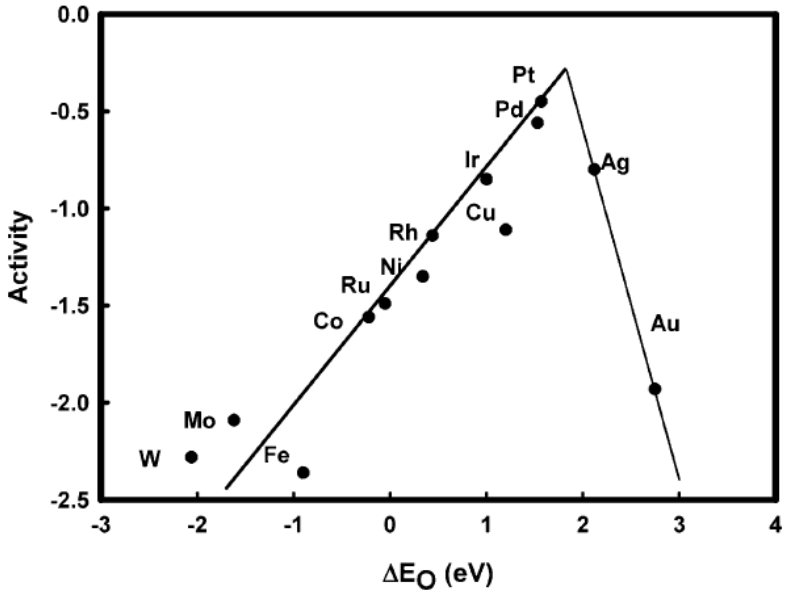

Figure 4: Volcano plot of metal catalysts for ORR as a function of oxygen binding affinity (ΔE_O)

In consequence, Nosrkov et al pointed out that a room is available to engineer metal catalysts that surpass Pt activity. According to their DFT calculations; alloying Pt with metals that have stronger binding affinity to oxygen (e.g. Ni or Co) reduces the over affinity to bind to oxygen and moves uphill in the volcano plot, when surface atoms are Pt rich.[23] In addition, crystal orientation showed significant influence on ORR activity, as different surfaces possess different bonding affinities with ORR intermediates. Enormous research

efforts have been spent to investigate the effect of Pt-alloying, forming layered structure (i.e. core@shell), crystal orientation, particle size and shape on ORR activity, as will be highlighted in the following sections.

3.1.2 Effect of crystal structure

Markovic et al[28] investigated ORR activity at different Pt single crystal surfaces. Specifically (111), (100) and (110) were examined for ORR using rotating disk electrode (RDE) setup. Results showed similar oxygen reduction mechanism following a 4-electron reaction pathway. Examining the half-wave potential (as an indication of ORR overpotential), Pt (110) showed lower overpotential for ORR, as onset potential was ~25-50 mV positive than other two samples (more positive is lower overpotential). Moreover, Pt (111) showed significant reduction in diffusion limiting currents compared to its counterparts (i.e. Pt (100) & (110)). To unravel the reason behind the observed trend, authors investigated the rotational speed of the RDE while observing associated changes on the diffusion limiting current on each surface, where increasing the rotational speed decreased the diffusion limited currents. Authors suggested that the reason behind current decrease is due to blocking the active sites by either hydrogen desorption or contaminants (e.g. Cl^-, NO_3^- or organic compounds) from the electrolyte (acidic or basic). The faster the disk rotates the more adsorbates to accumulate on the electrode surface. Similar observation was reported for oxygen adsorption to the surface, as a dependent on crystallographic orientation. Pt (110) showed an optimal situation with strong interaction with oxygen and hydrogen reactants, and facile desorption of OH^-. In conclusion, each crystallographic orientation, even for the same metal, showed to possess distinguishable

catalytic activity. Other studies reported activity of ORR on different Pt nanoparticles with surfaces of high index planes (e.g. (720), (510), (830)). Results showed high dependency on the presence of high index planes compared to Pt (111) commercial catalyst.[29] Surface with high index planes possess high density of kinks and atomic steps which have high affinity for oxygen adsorption. Oxygen adsorbs firmly to low-coordinate atoms (i.e. lower number of nearest neighbors). In consequence, other oxygen atoms (un-bonded) have no option but move on the surface to bond to atomic sites which have relatively lower adsorption affinity to oxygen (i.e. kink-free or step-free atoms), which yielding an easier desorption of OH^- when reduction occurs. Abdelhafiz et al, reported growth of Pt (100) on graphene, were Pt surface experienced ~4% compressive strain. Results showed that strained Pt (100) had advantage over Pt (111) to catalyze ORR.[12,30] Since, Pt surface crystal orientation shows a significant impact on ORR activity, enormous research efforts have been directed to control catalysts surface orientation and particles shape in particular, as will be discussed in the following section.

3.1.3 Effect of particles shape and size in correlation to crystal orientation

Controlling particles size and shape is of huge interest in electrocatalysis of ORR. Several synthesis parameters can be fine-tuned to give a plethora of catalyst particles' shapes and sizes. Synthesis parameters can be classified into two major categories: chemical and physical. Chemical as reducing agents which react with metal precursors to form metallic nanoparticles, pH (e.g. Pt growth along (111) is prohibited beyond pH of 4.5), capping agents where growth along specific crystal directions can be hindered or promoted, or catalyst support which acts as a seed from which catalyst growth starts.

Physical as temperature or mechanical force (i.e. ultrasonication) which affect the reaction kinetics. Particles shape can be classified into 1D, 2D or 3D dimensional, referring to the Pt growth direction. Nanoparticles with 1D (e.g. rods or wires) or 2D (e.g. sheets) are less favorable since they possess lower surface area per catalyst loading compared to 3D nanoparticles. 3D nanoparticles are more favorable, with abundance of the research literature presented on them, can be classified into four categories: perfect polyhedron (e.g. cubes or octahedron), truncated of over grown polyhedrons, irregular/branched nanoparticles (e.g. multipods and nanoflowers) and spherical nanoparticles. [29,31–35]

Surveying the literature showed discrepancy to conclude the relationship between specific or mass activities and catalyst architecture. Shao-Horn group reported a study on commercial Pt catalyst. Carbon-supported Pt nanoparticles were calcinated in Ar atmosphere for 1 and 120 minutes, where particle size grew from 2 nm to 3 and 4.5 nm, respectively. Authors used XPS to study the chemical state of Pt atoms. Results showed that increasing Pt particles size, increase the ration of metallic Pt (i.e. Pt^0) to cationic Pt species (i.e. Pt^{2+} & Pt^{4+}), with Pt^{4+} diminished with particles enlargement. Authors attributed this observation to the reduction of edge Pt atoms with increasing Pt particles size, where edge sites are more likely to form strong bonds with oxygen. Authors claimed independency of specific ORR activities on Pt particle size, as no trends could be observed for size dependency and activity. In our opinion, the study misinterpreted that data presented in three aspects: first, the TEM data reported Pt particle size with wide polydispersity (e.g. particles annealed for 2 hours at 900 °C had particles ranging 3.5 – 6 nm in size) without providing standard deviation for the observed particles' sizes. Second, authors interpreted the change in edge/surface active size ratio by analyzing XPS data,

relying on the fact that XPS is a surface sensitive technique, although XPS is a near surface sensitive detection technique (i.e. detects few atomic layers thick close to the surface depending on electrons inelastic-mean-free-path). In essence, enlargement of particles size from 2.5 – 4 nm (in average) increase both bulk/surface atomic ratio. Most likely, atoms buried within underneath the surface are in metallic state (Pt^0). Therefore, attributing cationic species to step-edges active sites bonded to oxygen lacks a supportive evidence from TEM analysis. Third, TEM analysis did not show neither diffraction pattern nor particles morphology (e.g. spherical or cubic), where different morphologies possess different densities of edges and specific crystal orientations.[36]

The main reasons behind the lack of ability to establish a solid understanding of size and/or shape relationship to ORR activity goes back to different testing electrolytes. Different mediums (e.g. $HClO_4$ or H_2SO_4) can lead to different ORR mechanisms, 4 or 2 reduction steps pathways, respectively. In addition, mass or specific activities are reported for different Pt morphologies or crystal orientations. Therefore, Shao-horn et al, remarkably, published a fundamental analysis examining Pt size effect on electrocatalytic activity for fully-relaxed (i.e. unstrained) cuboctahedra nanoparticles. Pt nanoparticles with ~1.3 nm in size were used as a seed, on which monolayers of Pt were electrodeposited following an underpotential deposition (UPD) using a sacrificial layer of Cu atoms. As expected, increasing the Pt particles size reduced the ECSA (m^{-2} g^{-1}) monotonically. On the other hand, specific activities increased by 4 folds up to a size of 2.5 nm particle, before it levels off (within the error bars) for further increase of Pt size to ~4.7 nm. Mass activity followed a volcano type relationship, with an activity increase up to 2.2 nm particle size

followed by activity drop for further increase in Pt size. DFT analysis showed that decreasing the size increased the percentage of atoms at edges, which possess high affinity to oxygen binding. Therefore, increasing the particles' size up to 3 nm helped promoting ORR activities by providing more active sites with moderate oxygen binding energy (i.e. neither too strong nor too weak). Further increasing in particles' size larger than 3 nm did not change the percentage of surface/edge active sites, which provides a plausible explanation of the observed specific activity trend. Results unraveled ORR activities on different atomic sites to descend as (111) surface > (100) surface > (111) edge > (100) edge. According to the observation by Shao et al, lower coordinated atoms (i.e. active sites at edges) have narrower and lower-filling d-band which implies stronger Pt-O binding energy.[37]

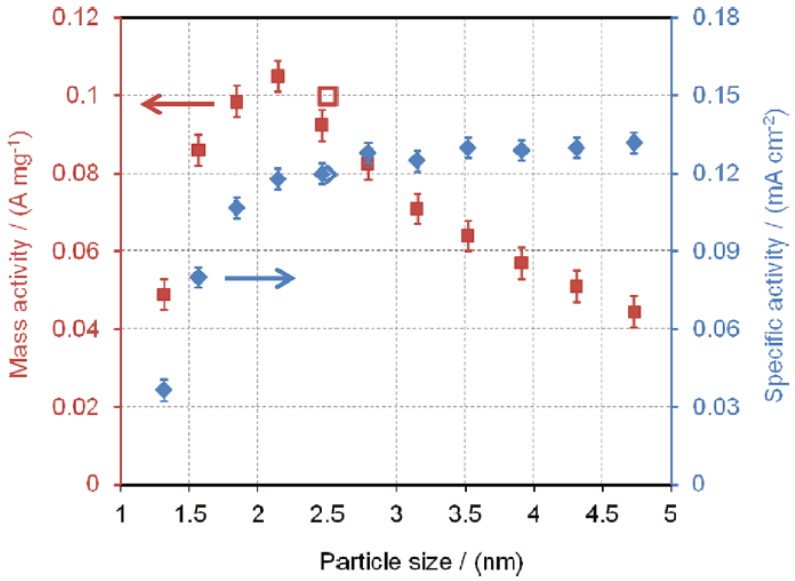

Figure 5: Mass and specific ORR activities for truncated cuboctahedra Pt nanoparticles measured in 0.1M $HClO_4$ at 0.93 V vs RHE

3.2 Catalysts Architectures/Platforms for ORR

Over the past two decades several platforms for low temperature ORR catalysts have been investigated. Catalyst design can be classified into two major categories: alloyed (i.e. random dispersion of two or more metals, including Pt) and Core@Shell[38,39] layered structure with Pt metal sits at the out-most layer of the catalyst (i.e. shell) where a relatively cheaper material is buried inside (i.e. core). Recent efforts have introduced the concept of atomically dispersed catalysts for ORR. At the following sections, a comprehensive literature survey about different catalyst platforms for ORR, indicating their respective catalytic advantages and shortcomings, is summarized.

3.2.1 Pt-based alloyed nanostructures

Mukerjee et al. synthesized Pt-Co alloyed catalyst. Results showed significant enhancement of ORR mass and specific activities for all Pt-Co catalysts. Authors investigated the root cause behind activity enhancement through various Pt/Co molar ratios. Pt-Co catalysts with low Co content (i.e. less than 10%) showed random dispersion of Pt&Co throughout the catalyst particles (i.e. alloy). Increasing the Co ratio till 30% changed the particles composition to a Co-rich core and Pt-rich surface. Authors attributed the activity enhancement to the shortening of Pt-Pt bond distance (i.e. compressive strain effect) due to lattice mismatch between Pt and Co atomic radii. Pt-Pt bond distance was monotonically decreasing with Co ratio increasing. A major drawback of the catalyst was Co leaching at acidic environment, where abundance of Co atoms was lost in the solution. Results showed that various catalyst possessed very similar final Pt/Co ratio after exposing the Pt-Co particles to an acidic environment. This indicates a poor chemical stability for rich-foreign element alloys.[40] Yung et al. investigated the effect of surface composition of Pt-Ni alloy nanoparticles. Synthesized Pt-Ni nanoparticles were heat treated in inert atmosphere. XPS and XANES analyses showed reduction of Pt binding energy, while at the contrary, Ni binding energy increased. Authors attributed the change in Pt and Ni chemistry to change in both chemical and structural states. Pt tend to be more metallic while Ni preferred to bond more to oxygen. In addition, Pt atoms clustered together at the surface. The heat-treated samples showed better ORR activity. This indicates the activity enhancement when Pt/Ni phase segregated to form a Pt rich surface.[41] Stamenkovic et al. studied a specific catalytic system of Pt_3M alloyed systems for ORR, where M is a

transition metal. Authors reported the formation of perfectly random alloyed catalyst through sputtering. Upon thermal treatment, the top atomic layers (i.e. 3 layers) suffered phase segregation: full Pt evolvement to the outermost atomic layer, and a metal-rich alloy (e.g. Fe) occupied the second and third layers from surface. Ultraviolet photoelectron spectroscopy (UPS) showed an interesting phenomenon with downshifting the d-band density of states (DOS) to more negative values from the Fermi level. The downshifting was consistent for all Pt_3M systems, disregard of the M element. This result is a key finding in designing smart catalysts with underlaying 3d metal elements imposed "ligand effect" which altered the d-band center position of the on-top Pt surfaces. Moreover, Pt_3M catalyst showed poor stability of M metal elements in acidic environment (imitating PEMFC working condition), as M metal located near the surface was leached out upon exposure to 0.1M perchloric acid. In correlation, catalyst systems after heat treatment (i.e. fully covered Pt surface with Pt-M alloy underlayer) showed weaker OH^- adsorption energy compared to pure Pt surfaces. This is well aligned with the observation of d-band center downshifting, indicating a relation between the d-band center position and interaction energy between metal-adsorbates. The observation established by Stamenkovic et al was helpful to establish a better insight in correlation with the Sabatier principle. Nevertheless, M elements like Ti and V showed extremely downshifting of the d-band center far from the Fermi level, their Pt_3M compounds showed poor ORR behavior. This can be described by the two opponent factors governing ORR; as shifting the d-band center down weakens the OH^- adsorption where Pt active sites are clear for reaction species access (i.e. O_2), but the adsorption affinity of reaction species is very weak. Therefore, results showed a volcano type relation with Pt_3M based on either Co or Ni located at top of the volcano.[42]

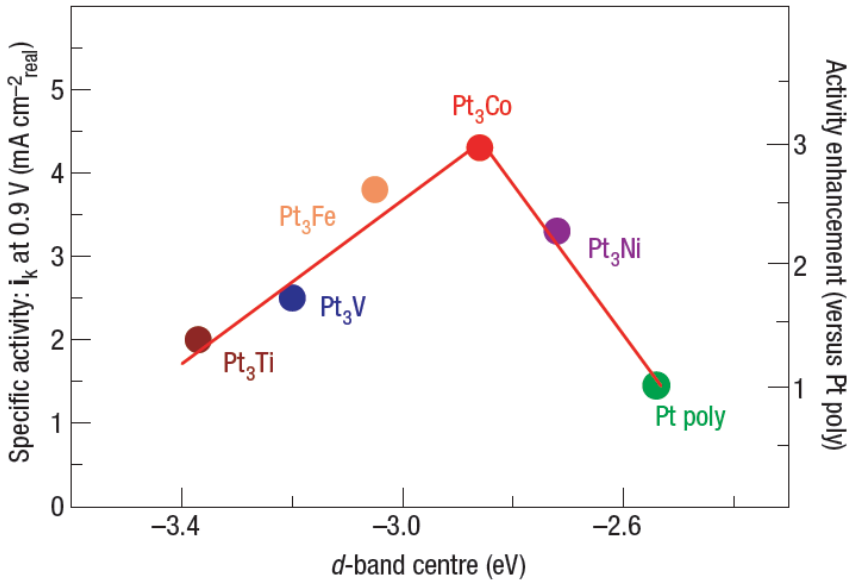

Figure 6: Volcano plot of ORR activity of Pt_3M core@shell structures in correlation to Pt d-band center. At the left-side of the volcano plot; Pt_3M systems showed weaker interaction with reaction intermediates (O2 and OH-), while the right-side resembled stronger interaction (i.e. difficult liberation). Pt_3M consisted of a fully Pt surface at the utmost atomic layer and M-rich cores.[42]

Hwang et al. used a combination of experimental and computational modelling based on DFT calculations to elucidate the advantage of Pt_3M (M is a transition metal) alloyed systems compared to pure Pt slabs. Authors and other reports[43] showed that alloyed catalysts have negative heat of formation which best describes their thermodynamic stabilities. Nevertheless, experiments showed dissolution of dopants (i.e. M elements)

under operating conditions, which was attributed to the more negative dissolution potential of transition metals than Pt (i.e. under operation conditions, potential applied is more positive than the dissolution potential of transition metals).[44] This finding is in agreement with Wang et al. construction of Poubaix diagram for Pt based materials for PEMFC at different pH values. At strong acidic environment, Pt corrosion starts at more positive potential than other transition metals.[45] Calculations by Hwang et al. showed that alloyed systems possess higher cohesive energies (i.e. higher stability, as cohesive energy represents the energy gained when arranging atoms from gaseous phase in crystalline solid) than Pt slabs. Pt_3Y showed the most pronounced catalytic activity, due to downshifting of d-band center of Pt atoms when alloyed with Y, as Y is thought to donate electrons to Pt.[44]

Post thermal treatment is a common technique to alter the alloy from random into an ordered arrangement. Most likely, post treatment occurs in reducing or inert atmospheres (H_2 or N_2/Ar, respectively) to prevent catalyst oxidation within a temperature range of 300-800 °C. Wang et al showed that post treatment modified the structure to form an ordered alloyed core with M_3Pt composition, while catalyst surface was fully Pt (top 3 nm).[46] Doping Pt with early transition elements showed significant enhancement over pure Pt with Pt_5M and Pt_3M for Ga and Y, respectively.[47] Debe at al synthesized Pt-Ni catalyst with 3/7 molar ratio. Results showed significant initial ORR activity enhancement. Following, a dramatic activity loss was observed due to Ni leaching in acidic medium. Ni atoms accumulated at the membrane signified the water rate transported from anode to cathode, which limited the activity accordingly.[48]

The vast majority of the literature is concerned with 3D nanoparticles with various polyhedron; however, several recent efforts have been addressing the synthesis of 1D nanostructure Pt-based alloys. One dimensional nanostructure possesses interesting anisotropic properties which would lead to an unprecedented catalytic activity. Nevertheless, one of the major drawbacks that limits the interest in 1D nano architectures, when compared to 3D nanoparticles, is their lower surface area to volume ratio. Therefore, research efforts have been directed to synthesize ultrathin nanowires/rods. Shaojun Guo et al synthesized ultrathin Pt-Co and Pt-Fe nanowires with ~2.5 nm. Results showed better activity for Pt-Fe over Pt-Co, however Pt-Fe contained less Pt. Authors synthesized 6.3 nm nanowires with double the activity of thinner aforementioned nanowires. Authors claimed 2-fold activity enhancement due to post thermal annealing and acid treatment, however, alloy composition changed with an increase of ~46% Pt, which might occur due to dopant dissolution (i.e. Fe).[49] Huiyuan et al synthesized ultrathin nanowires based on ternary alloys Pt-Fe-Ni and Pt-Fe-Cu. Results showed that for nearly fixed amount of Pt, having a mixture of Fe-Cu in the alloyed nanowire enhanced the stability, more than Fe or Cu alone within the alloy. Pt-Fe-Ni suffered from Ni loss during acid exposure, which suggests that ternary alloys are good candidates, however, with limited choices of dopants.[50]

In conclusion, alloying Pt with transition metals seems to be a plausible technique to enhance ORR activity, however, several factors should to be taken into consideration for an efficient catalyst design:

- Alloying has to possess higher/similar stability relative to Pt under PEMFC operating conditions (i.e. pH and potential) to prevent alloying-elements corrosion.
- Ligand effect composed of stress induced on catalyst surface and/or modifying its electronic configuration (e.g. charge transfer). Therefore, ligand choice (i.e. the few atomic layers sitting at the interface underneath the catalyst) has to be tailored to induce compressive strain, specifically, with a correlated d-band downshifting with an extent that satisfies Sabatier principle.
- Particle size, shape and degree of alloying (e.g. random or ordered, with various stoichiometry) influence the ORR activity. Co-based or Ni-based Pt_3M catalyst showed the best activity, however, no single trend of activity enhancement can be concluded due to the aforementioned factors.
- A Pt-outmost surface purity (i.e. alloy-free) and surface roughness are two competing effects with alloying element detachment under operating conditions. Alloy-free Pt surface showed higher activity than alloyed Pt surface. During PEMFC operation, alloying element will detach, leaving vacant sites behind at the Pt surface. More vacancies will increase Pt ECSA as surface becomes porous. On the other hand, Pt possess strong affinity to bind to oxygen. Hence, activity drops.

Therefore, perfect design of catalyst core material and controlled growth of pure Pt surfaces captured the interest in the past decade, producing “Core@Shell” nanostructures. In the following section a detailed literature survey in this regard is presented.

3.2.2 Core@Shell structures

State of the art commercial catalyst produced by JM company is ~3 nm in diameter. For a 3 nm particle, 30% of Pt atoms are exposed on the surface while 70% of the rest are buried inside, acting as a core. Pt cost is one of the major reasons behind hindering the commercialization of PEMFC. Core@Shell technique showed a breakthrough to resolve this dilemma by using a cheaper core material than Pt to support the growth of few atomic layers of Pt atoms. Core material dictates the growth mode of Pt (i.e. island growth mode or layer-by-layer growth mode), and provide activity enhancement due to inducing strain on overlayer Pt layers and/or electron donation, which both alter the d-band center position of Pt atoms.[12,22,38,51,52] One of the major techniques to synthesize core@shell structure is based on Cu-mediated method. In the aforementioned technique, Cu monolayers are deposited at a potential less negative than their bulk deposition (positive to their Nernst potential) called Under Potential Deposition (UPD) on a noble metal core (e.g. Au or Pd). Following, a replacement takes place to replace Cu with Pt.[52]

A major factor governing the surface reactivity of Pt monolayers (i.e. few atomic layers thick at the core surface) is the core material. Adzic et al. investigated the effect of core material on ORR activity of Pt monolayers in a core@shell fashion. Different noble metals were used as a core material. Pd(111)@Pt showed higher ORR activity than Pt(111), however, the rest of core materials (e.g. (Au (111), Rh(111), Ru (0001) and Ir(111)) showed lower electrocatalytic activity. Authors attributed activity enhancement or deficiency to strain induced on Pt overlayer, due to different crystal mismatch between core and shell materials. Au(111)@Pt showed ~4% tensile strain on Pt monolayers. On the contrary, Pt monolayers grown on Pd(111) showed a compressive strain. With the aid of

DFT calculations, authors were able to demonstrate a correlation between strain and altering the d-band center of Pt, as tensile or compressive strain shifts d-band center up and down, respectively. Results showed less OH coverage on Pt monolayers grown on Pd(111) compared to Pt(111) surfaces, which confirm the ease liberation of OH from Pt monolayers surfaces, satisfying the Sabatier principle.[53]

Stolbov and Zuluaga proposed another factor that affects the ORR activity of core@shell structures. Calculations of the formation energy between Pt monolayers and core materials showed weaker interaction for Pt-Au(111) and stronger interaction for Pt-Ir(111) or Pt-Ru(0001), in comparison to Pt monolayer bonded to Pt(111) surface. Authors claimed that for weak interaction, as between Pt-Au(111), Pt monolayers strain can be mitigated when a foreign influential factor is imposed on the surface, such as OH interaction. During OH adsorption at the surface, authors claimed that Pt-Pt, previously stretched due to Au template, is relaxed. On the other hand, for strongly interacted core-shell materials, not much difference can be seen in Pt-Pt bond distances, however, the d-band center is still shifted. The major key point denoted by the authors from the presented literature is that hybridization effect occurring between core and shell structure has significant influence on the d-band center position than strain effect, since strain can be mitigated during Pt surface interaction with reaction species.[54] To the best of my knowledge, there has been no experimental evidences supporting the authors claims and unravel the activity enhancement mechanism.

Protsailo et al. synthesized Pt monolayers on a dealloyed Pd-Cu core material. Dealloying of Pd-Cu core material, by leaching Cu atoms resulted in a porous structure. Results showed significant enhancement compared to state-of-the-art Pt-carbon commercial catalyst. These research efforts suggested that tailoring the core material can lead to unprecedented catalytic activity for ORR.[55] Inspired by this concept, Stolbov and Ortigoza proposed a tri-layer Pt-free catalyst platform for ORR. Authors based their calculation on a 4-electron ORR process going between each of them "down the hill" without any activation barrier, as all steps showed a negative Gibbs free energy. Top two materials are at single atomic layer thick, while the third (bottom) layer provide the mechanical support. The utmost material on which ORR intermediates will get adsorbed for reaction to occur. The 2nd material, in between, mediate the electronic structure and the binding energy of the top layer to satisfy Sabatier principle. A main concern in the proposed strategy is structure stability. Therefore, the sandwiched metal has to maintain a stronger bond and easier to form with top and bottom metals than what can occur between top-bottom materials. Hence, under processing conditions the sandwiched metal at the middle can evolve to the surface or the top metal sink down, where layered structure is limited. The proposed systems were: Pd/Fe/W and Au/Ru/W. To the best of my knowledge, Au is too noble to catalyze ORR to occur. Moreover, the cost effectiveness has no competitive advantage over Pt, since Au and Ru are quite more expensive. In addition, W at the working conditions (i.e. pH and potential) will be fully oxidized into WO_3, which possesses low electrical conductivity. For the second proposed model, as stated earlier, one of the major problems for Fe as an ORR catalyst (i.e. when alloyed with Pt) is leaching out during operation conditions. Therefore, We don't consider the following model to form a plausible

efficient ORR catalyst towards a real industrial application, as compared to Pt-based catalysts.[56]

One of the major advantages of nanoparticles compared to other nano-architectures, is the ability to mass produce them at industrial scale. The vast majority of the core@shell nanoparticles are synthesized at micro-gram or milligram, at most. Industrial scale application (i.e. practical PEMFC application) requires gram scale production, where, synthesis uniformity is quite poor. Pt monolayer synthesis following a Cu-mediated sacrificial layer involve a displacement step where copper atoms are replaced by Pt atoms. Factors governing Pt mass transport, like solution concentration, Pt-injection speed, solution rotation speed and temperature are difficult to control at larger containers (e.g. 2-3 liters). As a result, Pt atoms might from clusters (i.e. Pt deposit on top of each other instead of the vacant spots left by Cu replacement at core material) rather than forming a fully wetted layer. Another drawback is the dissolution of core material. Core material (e.g. Pd or Ni) is dissolved into the electrolyte under processing conditions. An alternative solution is using an alloyed core material. Sakai et al proposed a Pt monolayer formation on a Pd-rich Au-alloyed core material. According to authors, Au evolve towards the surface during cycling, where Au atoms block the vacancies within Pt-shell surface (from which Pd used to dissolve into the solution).[57] However, this technique helped to stabilize the core-shell structure, but Au atoms are not ORR active, which reduces the number of active sites per particle. A more stable, but yet more expensive, approach was proposed following a dealloying technique. Core material is synthesized from an alloyed Pt-M, which is subjected to acid leaching, where M (e.g. Cu or Ni) is dissolved into the acidic solution.

Thus, core material is a porous Pt-rich core where Pt monolayers are deposited on top, as described earlier. Results showed enhancement of catalyst stability, attributing the activity enhancement to strain effects only, since ligand effect is negligible (as ligand is mostly Pt).[58]

In conclusion, core@shell catalyst platform is a good candidate for efficient ORR applications towards PEMFC, however, some factors have to be well tailored:

- Core material has a significant effect (i.e. ligand effect) on overlayer shell electronic configuration, and catalytic activity in consequence.
- Core shape (e.g. type of polyhedron and radius of curvature of spherical particles) and crystal structure may evolve Pt with either tensile or compressive strain, where the former suppresses ORR activity and the later enhances the activity. Therefore, core material design has to be well tailored
- Core dissolution under operating condition is a crucial factor. Over time, core material diminishes, and losing Pt active surface area.
- Large batch synthesis of core@shell particles at gram scale production is yet a problem to be resolved.

3.2.3 Atomically dispersed catalysts

Three decades ago, nanotechnology introduced a new paradigm of a material utilization, where higher surface area can be provided by dividing a large chunk of a catalyst into significantly smaller nanoparticles. This approach enhanced the mass activity of the catalyst, as only surface atoms are participating into the catalysis process. Three

decades efforts yield optimal size of nano catalysts for ORR ranges 3-4 nm in diameter. State of the art commercial catalyst produced by JM company has an average diameter of 3.4 nm, where ~2/3 of the catalyst atoms are buried under the catalyst surface, omitting the catalysis process. Therefore, research efforts over the past two years have been directed to take a step further, miniaturizing the catalyst particle towards single atomically dispersed catalysts.

Gongquan et al. recently reported the synthesis of single atom carbon-supported Pt electrocatalyst. Authors elaborated on the effect of nitrogen doping on structural and associated ORR activities in alkaline medium. Results showed a poor Pt loading on N-free and N-doped carbon black substrates with 0.4% loading. Upon air exposure, combined TEM and XPS analyses showed more tendency of Pt to form cationic species (i.e. Pt-oxide) for N-free carbon supports, with ~70%. However, Pt loaded on N-doped carbon showed ~15% Pt-O species, where both values are extremely disappointing for ORR performance. In consequence, Pt-loaded N-free samples showed, almost, inert ORR activity. Although, N-doped samples showed enhanced ORR activity, still lower than state of the art Pt-XC commercial catalyst. DFT calculations unraveled the mechanism of Pt loading and ORR activities. Calculations showed that Pt favors anchoring on N-sites of N-doped graphene 3 times easier than Pt bond to pristine graphene (i.e. no N). Moreover, results showed that O-O bond distances stretches to longer bond distances at Pt atoms anchored on N-doped graphene, which facilitates the O-O bond dissociation, compared to Pt atoms anchored directly to graphene without nitrogen. In addition, results showed difficult adsorption of H_2O_2 on Pt sites supported on N-doped graphene, as O-O bond distance stretches to almost the double where H_2O_2 becomes very unstable. Results showed significant effect of

nitrogen doping on Pt dispersion, as N-free samples showed agglomerates of Pt nanoparticles with ~10nm diameters.[59] Sun et al. deposited atomic-layer Pt catalysts on graphene nanosheets. Graphene sheets were initially oxidized to suppress the hydrophobicity of graphene, allowing for Pt growth by Atomic layer deposition (ALD). Results showed the formation of single layer Pt, however, Pt clusters (i.e. nanoparticles) were observed, as well.[60] Single atom Pt was successfully reported by Choi et al. on zeolite-templated carbon. Support was doped with sulfur to enhance the activity and number of active sites for Pt anchoring. The results showed the existence of Pt clusters, as big as, 2 and 4 nm for sulfur-doped and sulfur-free carbon supports, respectively. Moreover, the ORR reaction followed a 2-electron pathway, generating H_2O_2, which is known to be fatal for Pt surface. Sulfur is known as a poison element to Pt surface. This report might suggest the harm effect when using sulfur as a heteroatom dopant.[61]

Pengfei et al. reported the synthesis of single atom Pt catalyst supported on CeO_2. Atomically dispersed Pt atom was synthesized by exsolution of Pt atoms, previously impregnated within porous CeO_2 particles, when heated at 1000 °C. Authors claimed atomic dispersion of Pt on CeO_2 surface with ~0.5-1% mass loading, relying on STEM line scanning. With advancement of STEM imaging techniques nowadays, atomic resolution imaging can be achieved, however, guaranteeing the electron beam scanning along specific line of atoms, yet skeptical. EXAFS analysis showed only Pt-O peak, which suggested the absence of Pt-Pt crystal structure formation, however with very low loading below 1%, signal to noise ratio could be significant.[62] Sungeun et al reported the synthesis of single atom Pt catalyst on two different Ti-based substrates. Results showed catalyst loading of

~0.2% where DFT calculation suggested Pt atom to anchor at N or C vacancies. Single Pt atoms loaded on Ti-carbide samples showed better ORR activities compared to Pt loaded on Ti-nitride samples. DFT calculations showed less energy barrier for ORR process for samples on Ti-carbide due to preferential oxygen adsorption/dissociation according to the Sabatier principle. With visual observation, ORR polarization curves (i.e. linear sweep voltammetry) showed higher overpotential. A comparison with state-of-the-art Pt/XC as a reference is missed to better evaluate the catalysts quantitatively. EXAFS and IR analyses showed Pt-Cl bond existence, which can be attributed to the Pt precursor. These results suggested the failure of reducing Pt from cationic to metallic state, and can explain the high overpotential at ORR measurements.[63]

Yunhu el al. synthesized atomically dispersed Co atoms on carbon nanospheres for ORR applications. Authors deposited Co atoms at hollow and solid carbon spheres (~300 nm in diameter and ~5 nm thick). Results showed enhanced ORR activity for Co deposited on hollow spheres, compared to solid carbon spheres. Co catalyst grown on hollow spheres showed lower ORR activity, compared to state-of-the-art Pt-XC catalyst, however, accelerated durability testing results showed higher stability for Co-based catalysts, attributed to sulfur poisoning Pt catalyst surface (i.e. adsorption of bisulfate). Worth to mention, that catalyst loading (i.e. Co) was not provided by the authors.[64] Dapeng at al. synthesized Fe-based N-doped carbon. Results showed enhanced ORR activities for single atom Fe catalyst compared to Fe-sheets supported on pyrrolic N-doped carbon (i.e. Fe single atoms coordinate with 4 nitrogen carbons, each is a member of 5-atoms ring (4 carbons and one nitrogen)). Results showed that the Fe-N-C bonded were the active sites, emphasizing the role played by nitrogen doping in selectivity of anchoring Fe atoms. [65]

As a major problem towards practicality of single atoms catalysis, dramatically lower catalyst loading is a dilemma to be resolved. Catalyst loading (e.g. metal: Pt, Ru or Au) can reach 20%. Nevertheless, the content of atomically dispersed catalyst is limited below 1% for ORR and 5.9% for other electrochemical reactions, with the rest forming larger agglomerates (i.e. nanoparticles). Typical synthesis following a pyrolysis of a metal organic frameworks (MOF), followed by treatment in a nitrogen-rich environment, where catalyst atoms can be anchored separately to the support (i.e. nitrogenated carbon support). Li et al realized that a major problem is the insufficient nitrogen supplied at post pyrolysis treatment, which limits the number of anchoring sites, at which single catalyst atoms can be attached. Therefore, a synthesis route relying on dicyandiamide as a major source of nitrogen supply have been introduced. Dicyandiamide reacted with Cu-based MOF forming nitrogenated carbon sheets, where Cu atoms were anchored. Successful Cu atoms anchoring with high loading ~20.9% was observed, however, large chunks of Cu microspheres were observed, as well, which required a post acid leaching treatment to remove excess acid generated during MOFs pyrolysis.[66] MOFs pyrolysis is known to generate a hierarchal porous structure, which is thought to act as a host to encapsulate metal atoms or nanoparticles. This gives higher stability against agglomeration under operational conditions (e.g. temperature).[67]

Nitrogen plays a major role, as a heteroatom dopant, as it provides strong anchoring sites to which single atom catalyst (e.g. Cu) can bond strongly. In addition, homogeneous distribution of N hetero-doping across the carbon support ensures uniform distribution of single atom catalysts, since enough wide spaces in between atoms prohibits Oswald ripening, as confirmed by EXAFS analysis where Cu nearest neighbors are only carbons.

Most interestingly, Cu did not show metallic status, rather than cationic species which was confirmed by XANES. This finding resembles a double-edge sword, where strong interaction between catalyst and support is desirable, however, too strong bonding (i.e. ionic or covalent bond) is expected to hinder the catalytic activity for ORR. Electrochemical analysis was performed in alkaline medium. Results showed competitive activity compared to Pt/XC commercial catalyst, however, the long-term stability only lasted for 2.78 hours. This raises questions about the applicability of single atom catalysts at commercial ORR application in PEMFC, where prolonged catalytic durability (i.e. ~133 hours as indicated by DOE) under harsh acidic, humid and hot (i.e. 80 °C) are required. DFT calculations showed the rate limiting step of ORR to be either oxygen adsorption or OOH^+ formation, according to nitrogen content increase.

Major key points taken from the presented survey are:

- Pt loading is limited below 1%. Higher loadings trials tend to have Pt clusters, rather than individual atoms.
- Heteroatom doping is a crucial factor to achieve single atom dispersion. Dopant chemistry can produce undesirable ORR products (e.g. S-doping produce H_2O_2). In addition, doping has to remain within an optimum ratio, where catalyst loading can be maximized (over 1%) while avoiding agglomeration into nanoparticles.
- Anchoring mechanism of single atom catalyst varies according to the substrate. Most likely, metal atoms anchored at vacancies sites of dopants (i.e. N or S vacancies for carbon and N or C for metal nitrides or carbides),

however, the precise anchoring mechanism still needs to be unraveled. This should lead to better design of single atom catalyst where agglomeration is avoided.

3.3 **Catalyst support**

Catalyst support is a crucial factor influencing the overall ORR activity. Support provides a backbone on which catalyst materials can be deposited uniformly. In addition, support acts as a current collector that connect the isolated particles to the overall PEMFC system. Therefore, support has to possess good chemical and mechanical stability. One of the serious problems in PEMFC is support deterioration under operating conditions. As a consequence, catalyst system loses its ECSA by either particles dissolution or agglomeration. Thus, a need for a robust, super conductive and catalytically active support is a must for efficient PEMFC operation.

3.3.1 Carbon-based materials support (GR, CNT, XC)

Carbon materials emerged as the best catalyst support over the past few decades due to their electrical conductivity and high surface area. Carbon black (e.g. XC/72R) is the most readily available and commonly used catalyst support in PEMFC. Carbon black has high surface area with a porous structure. Pores are ~8nm wide, which is a major drawback when Pt particles (typically 3-5 nm) is deposited within the pores, as poor mass transport of reaction species should hinder ORR reaction kinetics. Makoto et al. developed a relation between structure porosity of different carbon black materials and the overall catalytic activity. Results showed that the acetylene black with surface area of 219 m^2/g has higher

activity than similar sample with 779 m^2/g, due to limiting particles accessibility to structure pores.[68] Surface functional groups of carbon black (e.g. COOH, CO) play a major rule, not only in enhancing catalyst particles dispersion, but also enhances the binding affinity between catalyst and support.

Carbon nanostructured materials (i.e. graphene and Carbon Nanotubes (CNT)) emerged as potential replacements of carbon black.[69] Graphene or CNT possess higher mechanical stability, chemical stability against most acids and higher electrical conductivity compared to carbon black. Nevertheless, CNT surface is smoother and more inert (i.e. has less impurities compared to carbon black) which limits its ability to provide anchoring sites for catalyst particles attachment or growth. Therefore, CNT or graphene is subjected to chemical treatment (e.g. acid treatment) where functional groups (e.g. CO, CN, COOH) can be attached to the surface. Functional groups react with catalyst precursor during reduction process which enables stronger interaction with catalyst particles. Du et al synthesized Pt-Ni alloyed nanoparticles supported on multi-walled CNT. Results showed enhanced catalytic activity and stability of the synthesized catalyst in comparison to the commercially available Pt catalyst supported on carbon black.[70] Liu et al. modified CNT surface through heteroatom doping using sulfur. Results showed enhanced catalytic activity for ORR.[71]

Graphene is another top candidate as a carbon support for catalysts in PEMFC application. Graphene provides a large surface area, however, graphene suffers from serious issues: high affinity of graphene layers to restack due to interaction forces,

aggregation of Pt nanoparticles with time due to weak interaction with graphene and difficult dispersion of graphene in solvents. Therefore, similar to CNTs, surface modification of graphene is a must. Heteroatom doping (e.g. N or B) changes the graphene electronic structure due to covalent bonding formed between C and dopant, which perturb the characteristic SP^2 of graphene, in consequence graphene reactivity changes as well as bonding with Pt catalyst material. Experiments showed graphene as an inert electroactive material along its basal plane, however, edge planes are catalytically active. Along the same line, heteroatom doping showed catalytic activity of graphene. Moreover, strong interaction between catalyst atoms and graphene was observed, as a result of defect presence due to heteroatom doping. A major drawback of heteroatom doping is the limitation of doing, which acts as a double-edge sword. Extreme doping introduces many defects which cause excessive perturbation of graphene honeycomb structure (i.e. SP^2) leading to lower charge transfer (i.e. defects act as trap states).[72] Dopant concentration is a crucial factor in catalyst dispersion. Doped sites are more susceptible to catalyst atoms anchoring than un-doped sites. Therefore, if the nominal distance between two doped sites is short, the tendency of catalyst atoms agglomeration increases. Functionalizing graphene surface (e.g. adding COOH or CO) through acid treatment has shown enhancement in catalyst dispersion and catalytic activity. More interestingly, decoration of both graphene and CNT surface with metal oxide or nitride nanoparticles showed better catalytic activity. Decorating graphene and CNT with MnO_2 nanoparticles showed better catalytic activity than both individually, as graphene provides larger surface area, enabled better dispersion of MnO_2.[73] In addition, graphene provides faster current collection to supported metal oxides or nitrides. Pt loaded on metal oxides (e.g. CeO_2) graphene-supported showed

enhancement in ORR activity and stability.[74] In conclusion, an optimal level of dopant is a crucial factor. Excessive dopant will destroy the graphene electronic structure significantly and stimulate catalyst agglomeration due to shortening the distance between anchoring sites. Limited doping limits the number of active sites, and catalyst loading in particular.

3.3.2 Metal-based supports

Carbon black is not stable under PEMFC operation conditions, especially, the acidic environment. Group IV and V metal oxides would rise as potential candidates due to their respective stability in acidic medium, however, they fall short in terms of ORR activity due to the low affinity to adsorb oxygen and low electrical conductivity. Several research efforts proposed modified strategies to enhance metal oxides (MO) ORR activities. Since, one of the drawbacks, is the lack of oxygen adsorption sites, Liu et al. synthesized several metal oxides (e.g. Zr, Co, Sn, Nb and Ti), while annealing them in oxygen deficient environment. In consequence, MO surface had higher density of oxygen vacancies. Results showed good stability for Sn and Nb based oxides when tested in sulfuric acid, while Co showed the worst stability among the tested oxides. In terms of ORR activity, Zr samples showed the smallest overpotential followed by Co oxides sample, while Nb showed the worst ORR activity.[75] Following efforts by Takasu at al. tested metal oxide alloys, where results showed enhancement compared to their native oxides (Zr-Ti-O > ZrO_2 and TiO_2).[76] An interesting modification inspired by photocatalytic electrochemistry was introduced, as doping of N in metal oxides enhances their photocatalytic activities as a consequence of narrowing their bandgap (i.e. enhancing the electrical conductivity). In addition, binary and ternary oxy-nitride alloys were tested for ORR activity. Results showed that alloying Zr

and Ba in Niobate compound boosted the activity further due to suppression of higher cation oxidation states (i.e. more positive) at the surface (i.e. Nb^{4+} rather than Nb^{5+}). Higher oxidation state favors stronger interaction with oxygen, where OH^- liberation is difficult.[77] Ota et al proposed a combinatorial model based on the presented literature, when synthesized metal-oxide cabro-nitrides compounds. Samples were synthesized first in absence of oxygen (i.e. metal carbo-nitrides M-C-N), where results showed poor activity. Composite of partially oxidized metal with carbo-nitrides showed significant enhancement for ORR activity. Surface defects (i.e. oxygen vacancies) originated the activity enhancement while providing active sites for oxygen adsorption.[78,79]

The later finding summarizes the efforts spent on catalyst support. Key outcomes are:

- Partially oxidized metals give better ORR activity
- N-doped carbon enhances ORR activity
- Carbon-based materials are better than metal-based materials due to higher conductivity and activity, however, stability is a major drawback. Yet, that should be tackled by using nanostructured carbons (i.e. graphene and CNT).

CHAPTER 4. EXPERIMENTAL DESIGN

4.1 Research Objectives

Commercialization of PEMFC devices is hindered due to the high cost of PEMFC where 40-50% of the cost is spent on the catalyst component. In addition, with PEMFC operating under harsh acidic conditions, performance drops due to losing the catalytic activity. Catalytic activity loss can be attributed to two main factors: first, the loss of the catalyst material itself when catalyst atoms are washed away in the electrolyte or due to corrosion of the catalyst support (typically carbon black). Second, the loss of ECSA due to particle growth (i.e. ripening). The later can occur as a consequence of facile catalyst atoms diffusion which is agitated by the high surface energy of nanosized particles (i.e. 3-5 nm). Moreover, catalyst material deviates from thermodynamic equilibrium where an overpotential for the PEMFC reaction exists. Therefore, main research objectives are:

i) Enhancing the catalytic activities of Pt ORR to reduce the cell overpotential
ii) Enhancing catalyst material durability to prolonged lifetime (i.e. surviving 60% of ECSA after 30K operational cycle, according to DOE standards)
iii) Reducing the associated cost of catalyst component (i.e. maximizing Pt utilization per surface area, as only surface atoms are valuable for electrocatalysis)

4.2 Hypothesis

- Catalysis occurs at the outmost layer of catalyst material. Therefore, atomic scale Pt architectures (e.g. monolayers or single atoms) are anticipated to maximize Pt utilization. Although, in reality there might be a threshold when a diminishing-activity is observed with minuting Pt size.
- Graphene, due to its high mechanical and chemical stability and with recent advancement in synthesis up to roll-to-roll scale, can act as a robust, highly conductive and cost-effective catalyst support.
- Catalyst adatom expitaxial growth affects catalytic activity by altering metal-metal bond distance. Graphene can provide a template dictating Pt overlayer bond distance. Sign (tensile or compressive) and magnitude of mechanical strain on Pt adatoms can positively or negatively affect ORR activity.
- Capping catalyst with graphene can provide a fence-like barrier to Pt atoms preventing catalyst dissolution. In addition, graphene-Pt intimacy can generate an electronic coupling where a hybrid catalyst forms, on which ORR occurs without an activity loss. Thicker graphene can provide more protection, however, less accessibility of ORR intermediates to Pt.

4.3 Technical Approaches

In guidance of the aforementioned research objective and hypotheses; the research efforts can be subjected at two distinctive components:

4.3.1 Catalyst Synthesis

a) Maximizing Pt utilization per surface area (i.e. increasing the exposure of Pt atoms to ORR reaction species at lower Pt mass loading):
    - Deposition of atomically-flat and fully wetted Pt monolayers using an electrochemical layer-by-layer deposition following a surface limited redox replacement technique. The proposed technique can provide catalyst surface with lower density of kinks and defects, where oxygen interaction with catalyst surface becomes weaker.
    - Synthesis of ultra-small Pt nanoparticles with magnetron plasma sputtering
b) Capping catalyst surface with an ultrathin protective layer that can prevent catalyst dissolution, yet catalytically transparent to allow accessibility of ORR reaction species without an extra-energy barrier (i.e. overpotential).

4.3.2 Catalyst-Support

a) Replacing conventional carbon black supports with a highly durable, conductive and catalytically active support. Graphene promises tremendous interest in electrocatalysis due to super-aromaticity along 2D plane, mechanical robustness, high resistant to many acids and facile large-scale production (i.e. roll-to-roll synthesis).
b) Enhancing support activity through heteroatom doping (e.g. N). Dopant introduce defects in the graphene structure where strong anchoring sites can tightly hold catalyst atoms, hindering their mobility and post ripening.

4.4 **Structure-property relationship establishment**

4.4.1 Structural analysis

(a) Scanning Transmission Electron Microscopy (STEM):

STEM with lower operating voltage mode (e.g. 70 KeV) provides high resolution at sub-nanometer scale without damaging the catalyst/support structure. STEM imaging unravels catalyst dispersion and size distribution. In addition, STEM provides insights about Pt interaction with core atoms and/or support material. Moreover, catalyst atoms mobility is a crucial factor lead to potential agglomeration. Investigating the catalyst architectures under STEM with heating capabilities at 80 °C emulates the degradation mechanism of catalyst activity under PEMFC operating conditions.

(b) Extended X-ray Absorption Fine Structure (EXAFS)

EXAFS analysis provides information about the local surrounding of the catalyst atoms (i.e. nearest neighbors). EXAFS unravel the coordination between Pt shell, core material and support, which indirectly provides information about bonding strengths between the aforementioned three components.

4.4.2 Chemical Analysis

(a) X-ray Absorption Near Edge Structures (XANES)

Interaction between catalyst system components varies from weaker to stronger, chemisorption or physisorption interaction. Those possibilities can be unraveled through XANES where oxidation state changes of each of the catalyst components are detected.

(b) X-ray Photoelectron Spectroscopy (XPS)

Arrangement of the proposed catalyst system (i.e. protection layer/Pt/core/support) and maintain its layered structure is crucial for an efficient electrocatalytic application. EXAFS and XANES access are limited with accessibility at synchrotron facilities, in addition, to relatively tedious tool setup to enhance signal to noise ratio. XPS is a surface sensitive technique which provides high resolution information about the density of states and binding energy of Pt shell, core and support atoms. Thus, chemical interaction between protection layer/Pt/core/support can be unveiled. Ex-situ XPS is a powerful technique which provides insights about structural and chemical changes of the catalyst system along different synthesis and catalyst testing stages.

(c) Raman spectroscopy

Introducing defects or dopant is a crucial factor in modifying carbon-based catalyst support. Distance and concentration of defects/dopants controls the dispersion efficiency of the catalyst atoms (i.e. core and shell) and their tendency toward agglomeration. In addition, the thickness of the protective layer is thoughtful to have an influence on the catalyst performance (i.e. thicker layer blocks the activity and thinner limits the catalyst protection).

Raman provides details about the thickness of graphene layer and the presences of defects, and the distance between two adjacent defects through examining the ratios of D/G/2D peaks.

4.4.3 Electrocatalytic performance

Electrocatalytic testing is performed in 3-electrode electrochemical setup. Information about electrochemical active surface area (ESCA), in addition mass and intrinsic activities of the catalyst can be established.

(a) Rotating Disk Electrode (RDE)

RDE setup enables the control of solution flow towards and across the electrode surface, where the diffusion limited current during linear sweep voltammetry (LSV) is controlled by the flow of the solution rather than the diffusion of the reaction species within the solution. RDE setup enables evaluation of the catalyst performance through examining the onset and half-wave potentials of LSV polarization curves as an indication about ORR overpotential. Controlling the rotational speed (i.e. angular speed) of the disk controls the flow, where insights about reaction mechanism and interaction with foreign species (e.g. ORR intermediates or electrolyte contaminants) are unraveled.

(b) Membrane Electrode Assembly (MEA)

MEA testing is a powerful tool where catalyst material is directly investigated at actual PEMFC operating conditions. Catalyst material is deposited through spray techniques on either electrolyte (i.e. nafion

membrane) or gas diffusion layer (GDL). PEMFC is assembled of nafion membrane with two catalyst layers for anode and cathode, two GDL and current collectors at each side.

CHAPTER 5. RESULTS & DISCUSSION

5.1 Evaluation of graphene as template growth and catalyst support for monolayers Pt catalyst

5.1.1 Experimental section

Individual monolayers of graphene were obtained from American Chemicals Supplier, previously synthesized by chemical vapor deposition over 25 µm Cu-foil. Glass substrates were cleaned in Piranha solution (H_2SO_4: H_2O_2 – 4:1) for 15 minutes, followed by physical vapor deposition of a 15 nm Cr layer and a 50 nm Au layer, successively, using Denton Explorer E-beam Evaporator. A deposition rate of 0.5 Å/sec was used in order to achieve to most uniform Au coating possible. AFM measurements of deposited Au on glass substrates show an RMS value of less than 1 nm (RMS). XRD analysis shows that the deposited Au surface is largely of a (111) orientation. The chromium acts as an adhesion layer for the Au, which acts as our core metal.

For Pt/GR/Au samples, a 100 nm thick PMMA (Polymethyl Methacrylate) layer was spin coated over graphene/Cu foil and left over-night to dry. The underlying Cu foil was then etched away by floating on nitric acid, with the coated PMMA layer facing up, followed by floating overnight in an ammonium persulfate solution. This was succeeded by cleaning in deionized water bath and isopropyl alcohol. After etching, the PMMA/graphene film was then transferred over to the

Au substrate. The PMMA/graphene/substrate was then baked at 220°C for 15 min with a ramp up from room temperature at 20°C/min. After baking, the substrate was placed in acetone to etch away the PMMA for 8 hours.

Once the substrate was ready for Pt deposition, Cu UPD was used to grow a sacrificial layer followed by galvanic replacement of Pt. By stopping the voltage sweep at a potential between the bulk removal and the UPD removal potentials for Cu, the surface coverage of the Cu UPD layer is self-limiting. The resulting Cu surface was then galvanically replaced by Pt atoms from solution. SLRR procedure was repeated to grow the Pt overlayer with monolayer-scale precision. All synthesis was done at room temperature in a glass cell with a hanging meniscus arrangement. All solutions used were deaerated by bubbling with ultra-high purity nitrogen before any chemical processes. Any potentials are reported relative to homemade Ag/AgCl reference electrodes. Pt wire was used for the counter electrodes. The solution used for Cu UPD was 10mM $CuSO_4$ + 50mM H_2SO_4 and Pt galvanic replacement of the Cu utilized 1 mM H_2PtCl_6.

The core-level electronic structure of the samples was examined by (XPS) via a Thermo K-Alpha XPS system using an Al Kα source. Cyclic voltammetry was employed to evaluate the surface coverage of Pt. EXAFS spectra at the Pt L3 edge was obtain at Brookhaven National Lab's National Synchrotron Light Source beamline X3B. Data was collected in fluorescence mode using a 13 element solid

state detector. Data handling for EXAFS was done using the ATHENA package. Linear sweep voltammetry was used to observe the sample surface activity by probing the oxygen reduction reaction. Finally, surface durability was examined via cycling tests in sulfuric acid. All potentials reported here are relative to homemade Ag/AgCl reference electrodes. The studied sets will be referred to as 'Pt/Au' and 'Pt/GR/Au' samples, respectively.

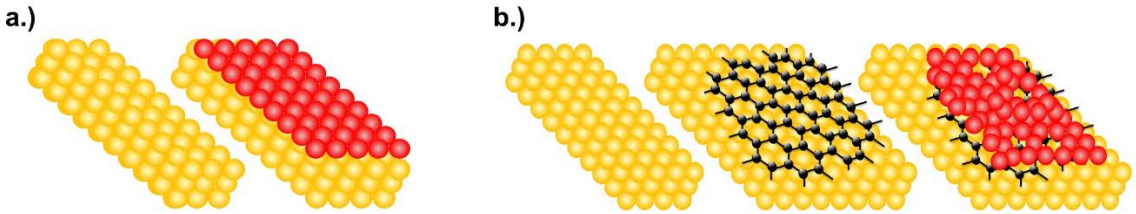

Figure 7 a) Represents Pt/Au samples, where Pt is grown directly on a bare Au substrate by SLRR. b) Represents Pt/GR/Au samples, where graphene is first transferred on top of the Au substrate before Pt deposition by SLRR.

5.1.2 Results and Discussion

5.1.2.1 Cyclic voltammetry

The Pt surface coverage of samples was examined via cyclic voltammetry (CV). Voltammograms were conducted in N_2-saturated 0.1 M H_2SO_4 by sweeping from 0 V to 1.2 V at a scan rate of 20 mV/s. The results for 2, 3, 4, and 5 MLs for both sample sets can be seen in Figure 8. CV is a surface-sensitive technique, as currents seen are generated from reactions at the metal-electrolyte interface. Thus, the Pt

surface area can be tracked by studying the Pt oxide reduction feature at 0.45 V against Ag/AgCl reference electrode. Similarly, the presence of a small Au reduction feature at 0.9 V indicates when Pt deposits are not fully masking the underlying Au.

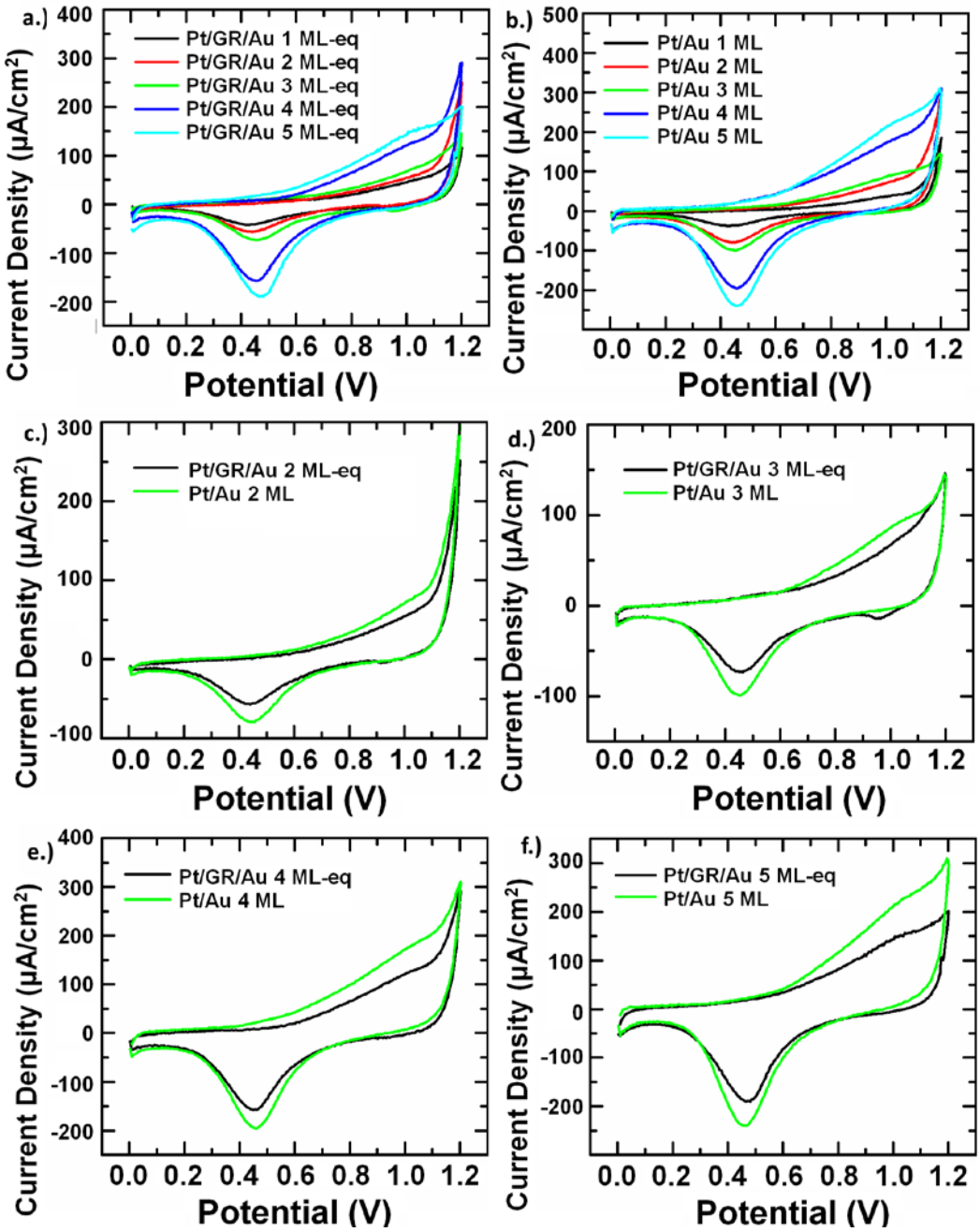

Figure 8. Cyclic Voltammograms for a.) Pt/Au samples b.) Pt/GR/Au samples, c-f.) 2, 3, 4, 5 ML samples respectively, comparing samples with graphene to those

without. CVs were performed in N^2-saturated 0.1 M H_2SO_4. Voltages are referenced to a Ag/AgCl electrode.

From Figure 8a and 8b, it is clear that the total surface coverage of Pt increases with SLRR iterations in both sample cases. Figure 8c-8f shows that Pt/GR/Au consistently exhibit a smaller Pt oxide reduction current density when compared to Pt/Au. A small Au reduction peak is seen around 0.95 V for 2 ML and 3 ML Pt/GR/Au samples. This is likely due to the sacrificial Cu layer clustering upon initial deposition and leaving exposed Au in patches on the surface, as mentioned by Liu *et al*.[80] For the Pt/GR/Au samples, a slight increase in the Au feature is seen from 2 ML to 3 ML despite a larger Pt reduction feature. This indicates a further tendency of contraction or clustering of Pt atoms rather than its wetting over Au. Beginning at 4 ML in the Pt/GR/Au case, the Au reduction peak disappears in CV, which indicates an eventual total coverage of Pt over graphene. This observation proves that an ultra-thin layer of Pt at 4 ML (1-2 nm thick) was able to fully mask the graphene/Au substrate. To our knowledge, this is the first reported full coverage of a metal on graphene at such low dimension over macroscopic surfaces areas. Pt/Au do not exhibit an Au reduction peak in CV even at 1 ML, which indicates that the Au must be fully masked by a wetted Pt layer by the first monolayer.

5.1.2.2 X-ray Photoelectron Spectroscopy

In addition to characterization by cyclic voltammetry, synthesized samples were also examined using XPS in order to determine the chemical state of the overlayer. In Figure 9, Pt is represented as a 4f electron doublet ($4f_{7/2,\ 5/2}$) at ~71 eV and ~74 eV, while the Au $4f_{7/2}$ photoemission is seen at ~84 eV.[81] Due to the surface sensitive nature of electron photoemissions, the relative peak size of the Pt $4f_{7/2}$ photoemission to that of the Au $4f_{7/2}$ photoemission is related to the average thickness of the surface shell. Figure 9 shows that, for both sample cases, Pt $4f_{7/2}$ grows in intensity relative to the Au $4f_{7/2}$ when more Pt monolayers are deposited on the surface.

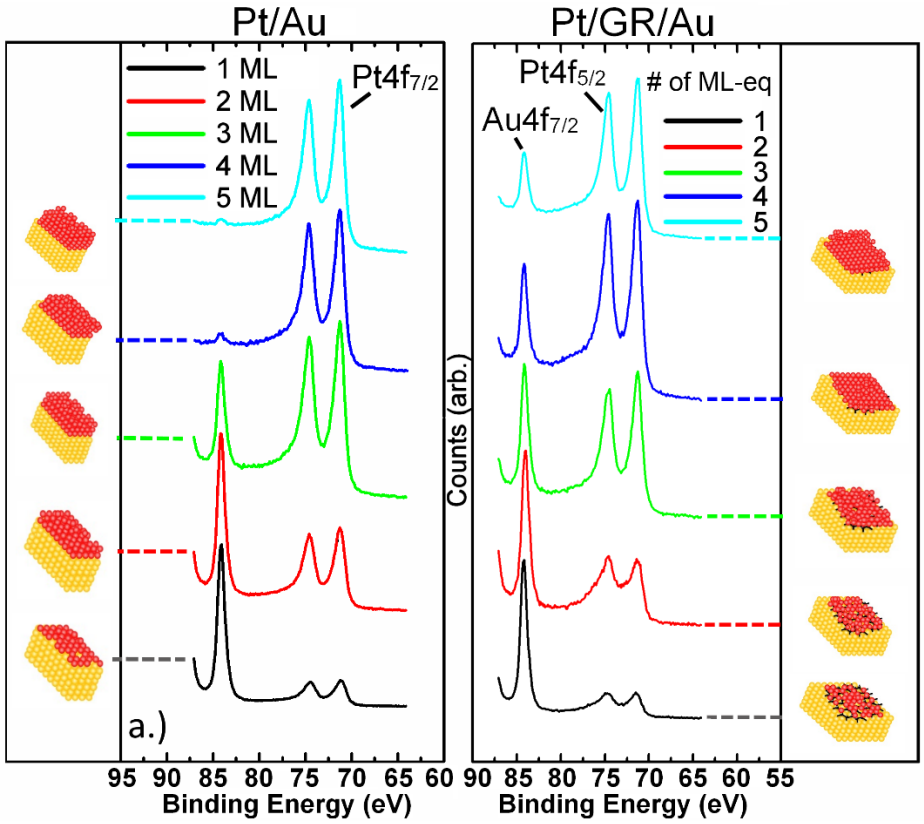

Figure 9. X-Ray Photoelectron Spectra of Pt $4f_{7/2}$, Pt $4f_{5/2}$ and Au $4f_{7/2}$, sequentially shown from low to high binding energy, for a)1, 2, 3, 4, and 5 ML Pt/Au samples and

b)1, 2, 3, 4, and 5 ML-eq Pt/GR/Au samples. Side bars show expected sample architecture of grown Pt overlayers.

However, the intensity increase is not growing at the same rate between the two sample sets. When comparing the 4 ML and 5 ML samples, the Au photoemission is almost completely masked for Pt/Au. This indicates that there are very few core electrons from Au that are emitted beyond the top few nanometers of the surface. For the Pt/GR/Au samples, the Au photoemission is not fully diminished even at 5 ML. This indicates that more Au is near the surface allowing its bound electrons to be detected. This could be due to a relatively thinner Pt overlayer in some regions that allow more Au 4f electrons through than in the graphene-free case. The peak area between Pt and Au comparisons were made via peak fitting using a Shirley background, and are shown in Figure 10.

Both the CV and XPS results show that growth process is not identical between the two sample cases. Cyclic voltammograms (Figure 8) show exposed Au on the surface for low monolayer Pt/GR/Au samples. XPS results cannot give an indication of surface wetting, but the data shows lower average Pt thickness in the core-shell structure for the Pt/GR/Au samples as evidenced by less intense Pt photoemissions relative to Au. This supports the findings made by Liu *et al*, which expected Cu to form more clustered structures on top of graphene, as SLRR in our case was by depositing Cu first which was replaced galvanically afterwards by Pt. The sidebars on Figure 9

represent the expected surface architecture for our sample set. We surmise these representations for our samples based on the data achieved and the conclusions made by Liu *et al*.[82]

Figure 10 represents the Pt $4f_{7/2}$ peak area normalized to the Au $4f_{7/2}$ peak areas. It can be seen that Pt/Au samples exhibit a larger relative Pt area and that the difference becomes more pronounced at 4 and 5 MLs. As previously mentioned, this might be due to Pt contraction for Pt/GR/Au samples, while Pt/Au continue to create well-wetted layers. A complete coverage of the underlying Au is seen in CV only after 4 monolayers were deposited on Pt/GR/Au samples. Pt/Au show nearly full wetting after only 1 ML, while Pt/GR/Au samples show clustered and/or compacted Pt island growth up to 3 ML. Only once the islands reach a certain threshold size (in between 3 ML and 4 ML) is a fully wetted layer eventually achieved, evidenced by lack of an Au oxide reduction peak in CV.

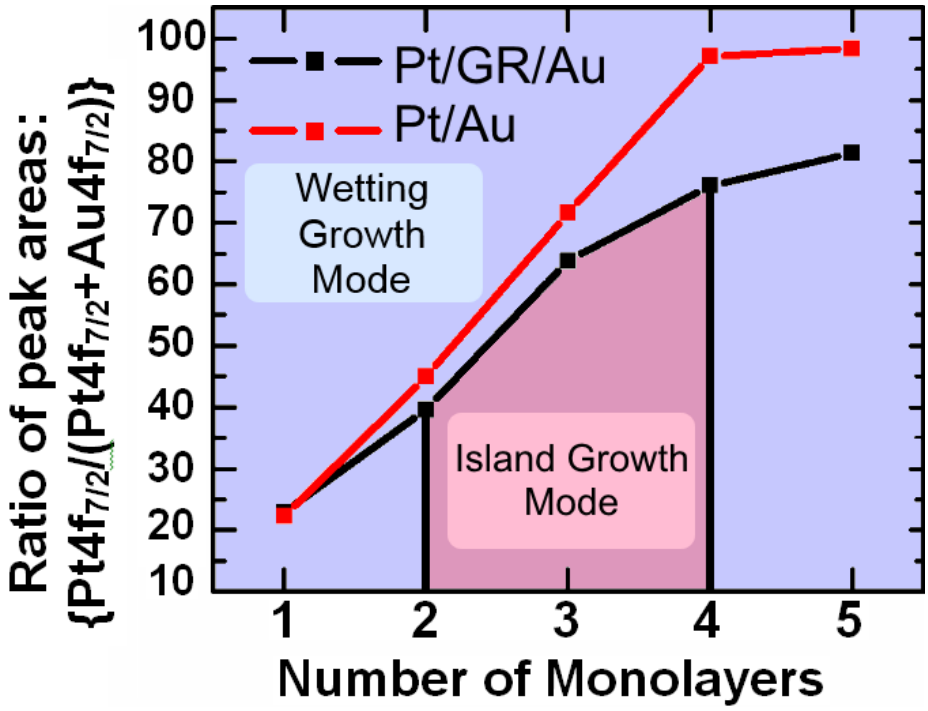

Figure 10 Representation of Pt to Au ratio by comparing the $4f_{7/2}$ peak area of Pt to the total $4f_{7/2}$ peak area of both Pt and Au as a percentage.

5.1.2.3 X-ray Absorption Spectroscopy

The local atomic structure around an average Pt atom was investigated using EXAFS for Pt adlayers in a subset of the Pt/GR/Au samples {XAS measurements in the presented thesis was performed at NSLS-I beam line at Brookhaven National Laboratory}. In Figure 11a, we see the R-space spectra for Pt/GR/Au samples as well as for Pt foil. The y-axis in the plot is proportional to a weighted partial radial distribution function around an average Pt atom. Bulk Pt (Pt foil) exhibits an apparent nearest neighbor (nn) distance of about 2.2 Å, consistent with previous work,[16] which is actually at a Pt-Pt bond distance of 2.78 Å when corrected for the

phase shifts of the electron waves in XAS. In Figure 11a we see that the 1 ML sample exhibits the nn distance of bulk Pt. This is interesting because, based on the preference of Pt to adsorb onto the bridge sites of graphene.[83] A flat, close-packed, Pt layer arrived at by populating every other bridge site with a Pt atom (Figure 11b), would exhibit a Pt-Pt nn distance of 2.14 Å instead of the 2.78 Å (phase shift corrected) nn distance we observe. At a 2.14 Å nn distance, the 1 ML Pt film would under a large compressive strain (Figure 11b). We propose, instead, that this 1 ML Pt film utilizes its degrees of freedom normal to the film plane to buckle, alternately adjusting the Pt-bridge distances and arriving at the 2.78 Å nn average bond length for Pt-Pt (schematically shown in Figure 11a).

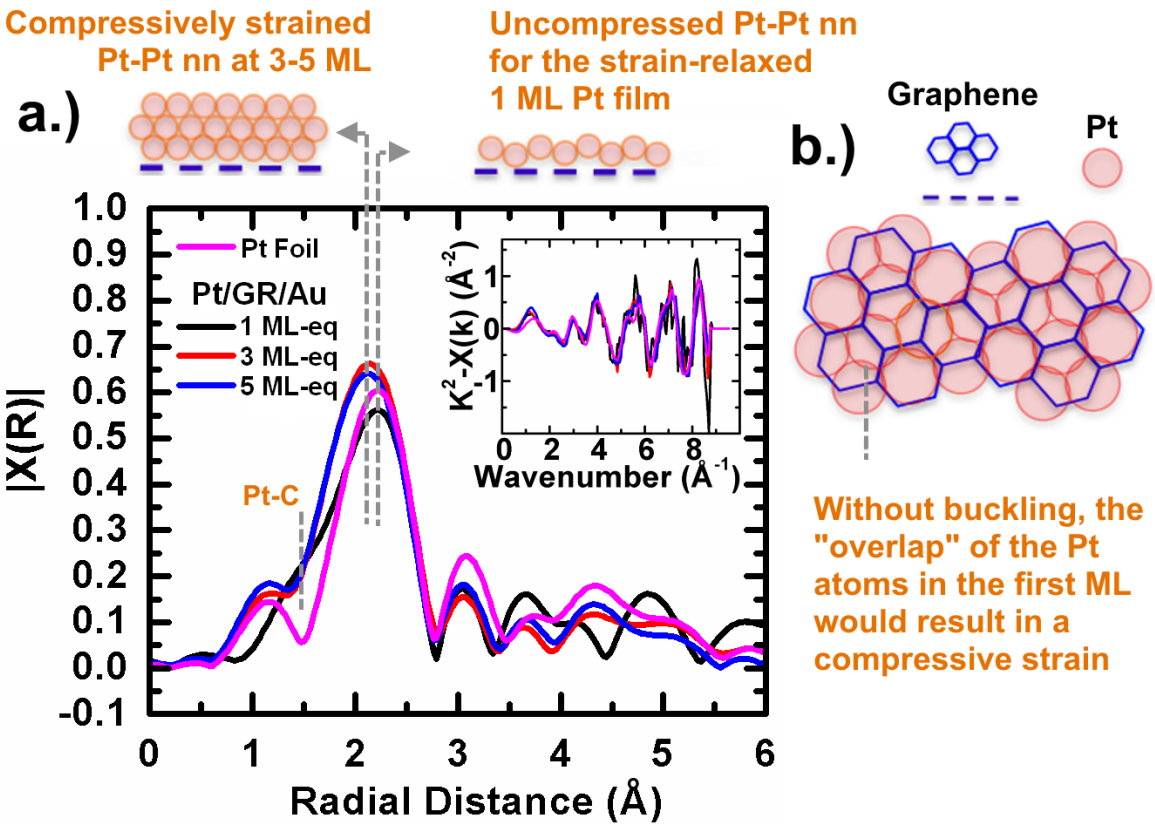

Figure 11 a) EXAFS spectra for Pt/GR/Au samples of 1, 3, and 5 ML and a Pt foil reference. Inset: The corresponding k-space data. b) Schematic of Pt atoms on graphene.

The structural similarity between the buckled 1 ML Pt/GR/Au Pt film and the bulk 3D structure of Pt foil is mainly restricted to the Pt-Pt nn bond. The 1 ML Pt film shows a Pt-C peak shoulder at about 1.5 Å, due to its bond with graphene, which is obviously absent in the Pt foil. Furthermore, the long-range order of bonding is quite different in comparison, highlighted by the window in the observed 3.5 to 5.5 Å range Figure 11a). In this R range, the spectra for the reference foil, the nominally 3 ML, and 5 ML samples all line up peak for peak, but the 1 ML case shows a variant long-range order. With only a single layer of Pt atoms, 1 ML film does not have an evolved long-range structure resembling that of bulk Pt.

When the Pt overlayer is several monolayers thick and distanced from the underlying graphene sheet, the atoms reject the buckled template of the 1 ML film and instead choose a strained face centered cubic (FCC) structure. While the 3 ML and 5 ML samples exhibit Pt FCC configuration, they however show a ~ 0.1 Å (or about 3.5%) compressive strain in the nn bond. This aligns with previous observations in CV where the Au reduction peak increased at 3 ML. Pt atoms were subjected to more compressive stresses, increasing the exposed Au surface as a consequence. Beyond 3 ML, further addition of Pt retains the compressive stress achieved at the 3 ML stage,

but additional Pt begin to fill in the exposed Au spots and maintain a full mask of Pt over graphene, as indicated by CV in Figure 8. By introducing graphene at the interface between Pt and Au, therefore, we have effectively created a new Pt-based species, one that has the electronic configuration and atomic structure of bulk Pt, but with higher electron density than due to its inherent compressive strain.

5.1.2.4 Catalyst Performance

When we look closer at the Pt photoemission binding energies in XPS, we see opposing trends emerging between the two sample sets, shown in Figure 12.

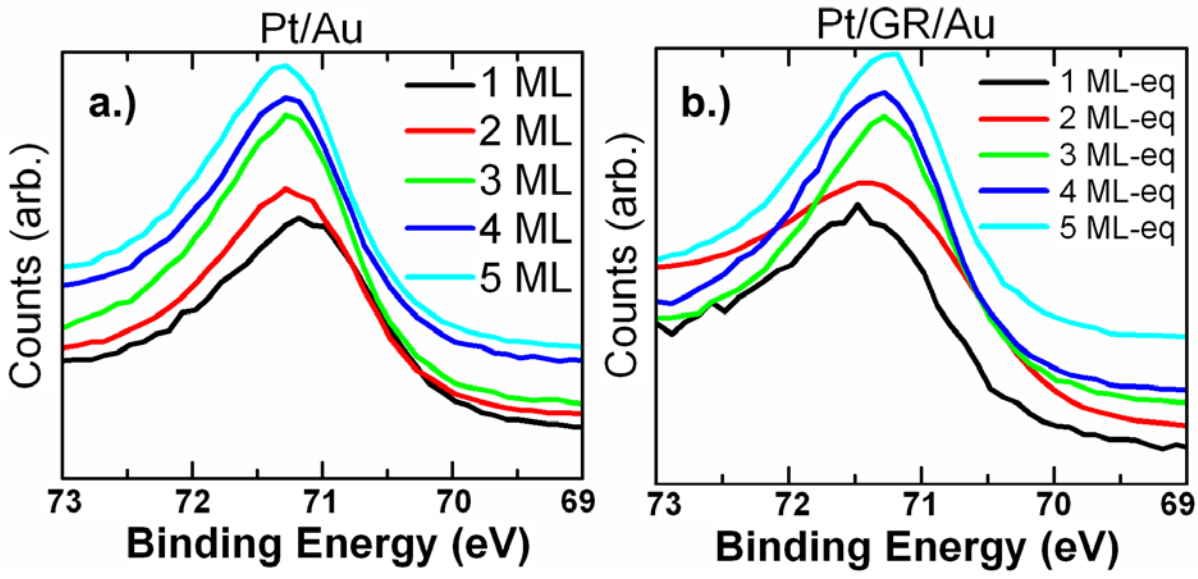

Figure 12 Platinum $4f_{7/2}$ photoemission from XPS for a) Pt/Au samples b) Pt/GR/Au

For Pt/Au samples, the binding energy shifts higher, from ~71.1 eV to 71.3 eV, with increasing overlayer thickness. This trend has been attributed to low-dimensional electron transfer effects from Au.[51] The Au substrate transfers charge to the adsorbed

Pt, an effect which diminishes with increasing Pt overlayer thickness. Pt/GR/Au samples instead show a shift to lower binding energy, from 71.3 eV to 71.2 eV. These results are also shown in Figure 12. We explore next whether these observed shifts in electron binding energy directly influences catalyst performance.

Electrocatalytic activity tests were conducted by performing linear sweep voltammetry (LSV), in oxygen-saturated 0.1 M H_2SO_4 at room temperature, from 0.8 V to -0.1 V, in order to analyze the ORR. The experimental results for each sample are shown in Figure 13. By following the first derivative peak of the ORR polarization curves, we measure the overpotential needed to catalyze the reaction. Because we sweep negatively, a higher reported potential denotes a lower required overpotential for the ORR. In order to make a comparison between the two sample cases, the Pt reduction shape in Figure 8 was used to normalize the ORR current densities with the relative amount of Pt present on the surface. Those results are shown in Figure 13, with potentials reported against Ag/AgCl reference electrodes.

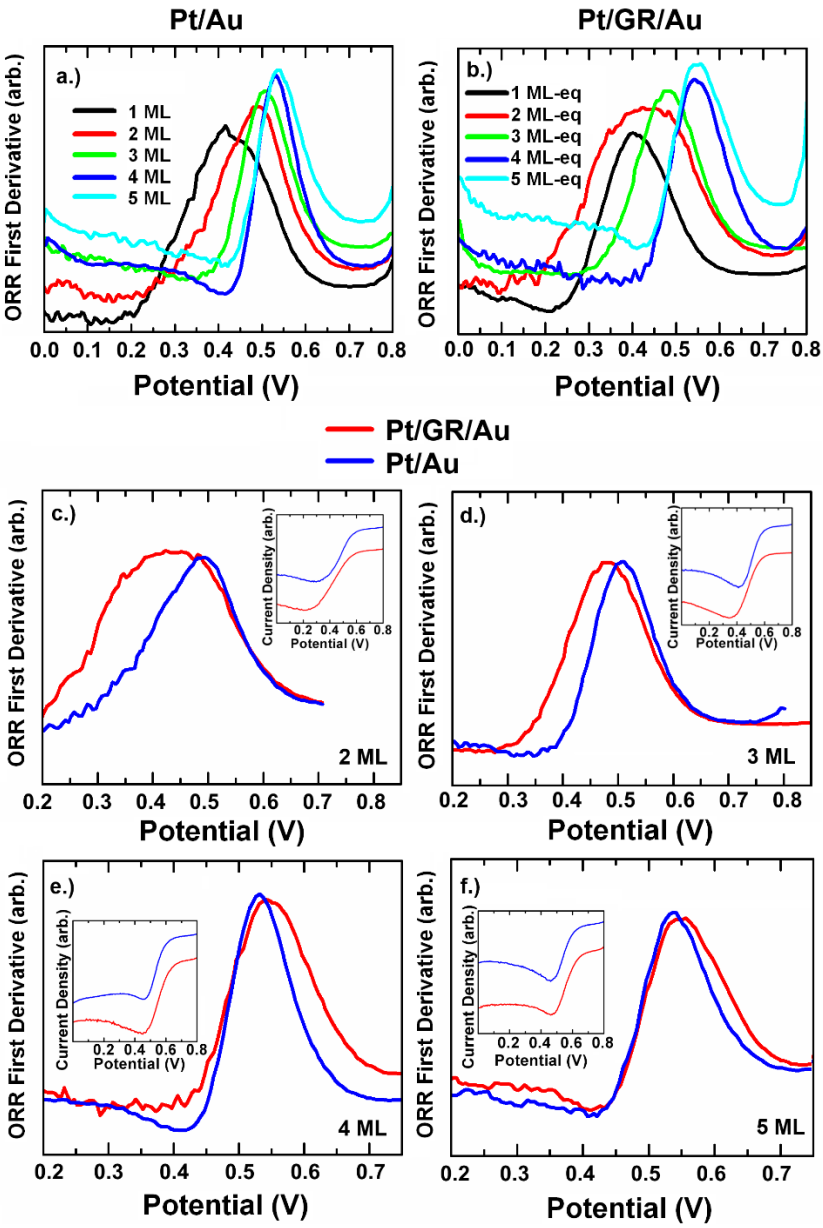

Figure 13 First derivative of oxygen reduction reaction polarization curves (against a Ag/AgCl reference electrode) obtained by linear sweep voltammetry in O^2-saturated 0.1 M H_2SO_4. a.) Pt/Au samples. b.) Pt/GR/Au samples. c-f.) 2, 3, 4, and 5 ML respectively. Insets) ORR polarization curves for each sample pair. The sweep rate is 20 mV/s. These curves have been normalized by the Pt surface charge obtained from the CV curves in Figure 2.

Figure 13 shows that for both sample cases, increasing the number of Pt monolayers results in higher potential values for the inflection point. For the 2 and 3 ML cases, the Pt/Au showed a notably higher ORR potential compared to Pt/GR/Au samples. However, for the 4 and 5 ML cases, the inverse is observed, where Pt/GR/Au samples show higher potentials when compared to Pt/Au samples. In terms of overpotential, the Pt/GR/Au samples demonstrate appreciably lower overpotential required once a sufficient amount of Pt is achieved on the surface. This correlates well with the binding energy values recorded, and a comparison between these experiments can be seen in Figure 14.

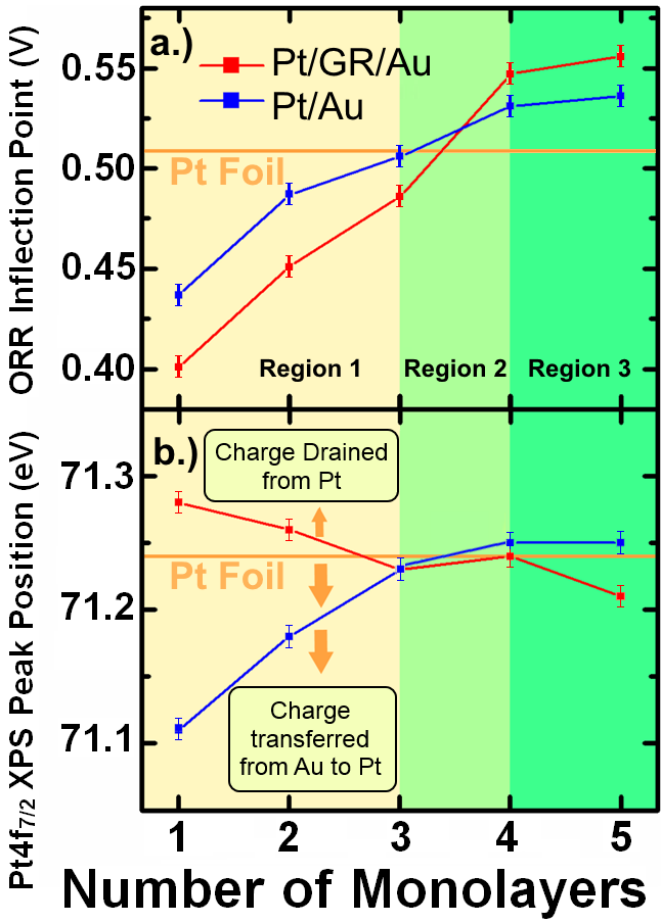

Figure 14 a) The inflection point of the ORR polarization curves and b) the Pt $4f_{7/2}$ photoemission binding energy for each sample case. A horizontal line is used to reference the binding energy of bulk Pt foil. Region 1 is explained by charge transfer mechanisms, from Au to Pt in the case of Pt/Au samples, and from Pt to graphene in the Pt/GR/Au case. Region 2 shows where charge transfer mechanisms have significantly diminished into Region 3, where graphene interfacial strain is lowering the binding energy of the Pt overlayer and ORR overpotential surpasses that of bulk Pt.

We see a convergence and eventual crossover of the ORR potential, as indicated by the polarization curve inflection points. This is represented in Figure 14a. Additionally, as seen earlier in Figure 12, we see opposite trends in binding energy between the two sample cases (Figure 14b). In Pt/Au samples, the low-dimensionality of the Pt overlayer allows charge transfer from the underlying Au causing a negative shift core electron binding energy of the Pt monolayers. This negative shift of binding energy for 1 and 2 ML Pt/Au indicates that adsorbed OH- species on the surface of the platinum require more energy to be removed than from a bulk Pt surface.[51] As the overlayer thickness grows, this low-dimensional effect diminishes, resulting in a binding energy which increases to that of bulk Pt as the net charge transfer approaches zero. Desorption of OH^- species from the catalyst surface is known to be a crucial element in allowing completion of the electronic reduction of O_2 to H_2O.[84]

In Pt/GR/Au samples, Pt overlayers of low ML thickness exhibit increased binding energies in comparison to Pt/Au. This is seen in Region 1 of Figure 14. This binding energy increase can be explained by surface charge calculations for noble metals adsorbed on graphene. Thermodynamically, Pt favors adsorbing on the graphene at the bridge site between two C atoms, as mentioned earlier when discussing our EXAFS data. A Pt atom forms a polarized covalent bond with the C atoms underneath and pushes them to move apart from one another. This bonding has been calculated to lower the charge of the adsorbed Pt by 0.108 electrons.[85] With this diminished

surface charge, we expect the binding energy of Pt photoemissions in XPS to be slightly increased as the data shows.

The XPS data indicates that this electron donation from Pt to graphene is diminished with increasing monolayer thickness, and the binding energy trends to that of bulk Pt foil. Assuming that the unoccupied densities of states in graphene is already saturated by the available electron density from 1 ML of Pt, any additional Pt deposited will diminish the share of electron density transferred to graphene per Pt adatom. Thus, for the Pt/GR/Au sample set, the binding energy of Pt electrons diminishes as the overlayer thickness grows. The binding energies of the two sample sets converge at 3 ML. We also see the convergence of the overpotential point between 3 and 4 ML. These two phenomena are represented by the Region 2. The Pt is no longer donating any electron density once it achieves 4 ML in thickness but is still affected by partially strained early monolayers, which causes a lattice mismatch resulting in increasing the ORR potential.

The 4 and 5 ML samples for both Pt/GR/Au and Pt/Au cases show lower ORR overpotential than bulk Pt foil. Monolayer catalyst architectures are noted for their smooth and ordered surfaces. The less the amount of imperfections and the more ordered the surface, the better it can be active towards ORR due to weaker OH^- binding. Both our monolayer architectures can be expected to be more ordered and more defect free than Pt foil, and show higher ORR potentials at 4 and 5 MLs. Thanks

to a compressed overlayer, as inferred from EXAFS data, it is also clear that 4 & 5 ML-eq Pt/GR/Au samples exhibit the lowest overpotential towards catalyzing the ORR. A compressive strain caused by the graphene will cause a decrease of Pt reactivity of the Pt–OH bond, further reducing the coverage of OH- species on the surface that inhibit the oxygen reduction.[86] Monolayer Pt shells templated by graphene achieve an additional boost in catalytic aptitude due to their compressive strain. This agrees with EXAFS analysis which shows the nearest neighbor Pt-Pt bond length to be constrained for these samples. This explains how the binding energy for 4 and 5ML Pt/GR/Au samples remain shifted to lower values in comparison to Pt/Au and bulk Pt-Foil. Region 3 shows when the Pt overlayer achieved is no longer expected to be affected significantly by graphene charge transfer effects, but Pt/GR/Au samples maintain lower binding energies as well as higher ORR potentials.

5.1.2.5 Catalyst Durability

One of the major requirements for an effective catalyst is its durability. Earlier efforts looked to using carbon support materials, such as carbon black, in order to enhance Pt retention.[87] While some improvement of catalytic activity was achieved, the durability of Pt catalysts remains a critical issue. Graphene has already been shown to improve catalyst durability in a variety of configurations.[88] We investigated the durability of our synthesized graphene supported Pt ML catalysts by cycling in acidic media.

Samples were cycled long-term from 0.4 V to 0.75 V in oxygen-saturated 0.1 M H_2SO_4, with a total of 1000 cycles performed on each sample. A characterization CV curve from 0 V to 1.20 V was taken in nitrogen-saturated 0.1 M H_2SO_4, once before cycling and once after 1000 cycles in order to examine the changes in the Pt reduction shape. By measuring the integrated Pt reduction charge before and after cycling, we can obtain an illustrative representation of the amount of surface coverage of Pt remaining on these samples. This is shown in Figure 15, where total Pt retention is displayed as a percentage its original integrated area. For the 1 ML Pt/GR/Au sample, the Pt reduction curve reduces more than 50% after 1000 cycles, showing low durability for the overlayer and is consistent with previous Pt monolayer experiments. This could be due to the unevolved metallic bonding of the 1 ML Pt film. The 3, 4, and 5 ML Pt/GR/Au samples retain Pt much more strongly than 1 ML, although there is still about a ~25% loss in electrochemically active surface area after 1000 cycles.

Pt/Au samples were examined in the same fashion. The 1 ML sample showed improved retention over its Pt/GR/Au counterpart, although it achieves only 50% retention after 1000 cycles. The advantage could be due to better wetting of the initial overlayer. 1 ML Pt/Gr/Au is buckled and should have poorer adherence to GR/Au than its 1ML Pt/Au counterpart. 4 and 5ML Pt/Au samples showed improved Pt retention, but remain lower than the corresponding Pt/GR/Au samples. For the 4 and 5ML cases, Pt/GR/Au showed improved Pt retention relative to Pt/Au with the

largest difference (of about 20%) for the 3ML case. The results indicate that loss of Pt is dictated mostly by bonding to other Pt atoms, an effect which is seemingly amplified in the graphene template multilayer Pt due to the compressive strain. This observation is worth further investigation in future research.

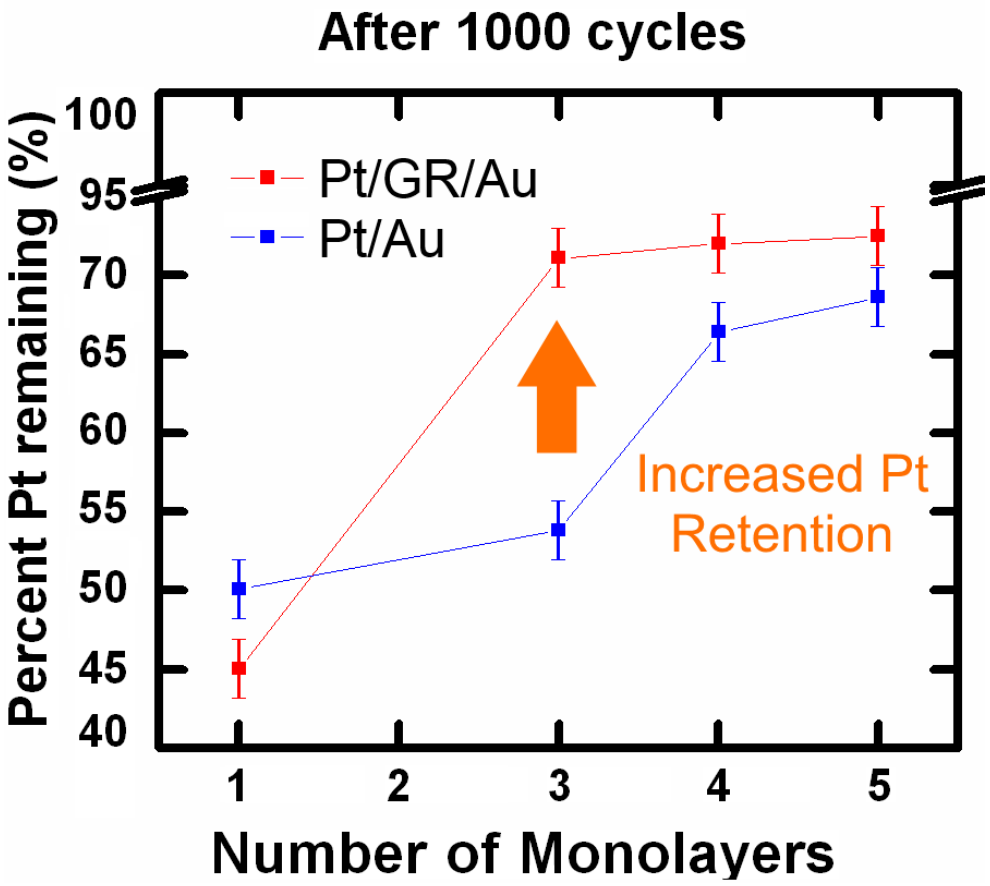

Figure 15 Using the Pt reduction shape in CV, the percentage of surface Pt is calculated after 1000 cycles in acidic media. Cycles were performed from .4 V to .75 V in O^2-saturated H_2SO_4.

This study embodies a systematic examination on the effects of graphene when incorporated into core-shell Pt monolayer catalysts. We have grown for the first time

(to the best of our knowledge) a fully wetted ultra-thin layer of a metal over graphene that is nominally 4 monolayers (less than 2 nm) thick. At such low dimensions, we approach the theoretical limits of Pt loading, thereby significantly increasing the activity per Pt atom. Moreover, due to a compressive strain of the Pt surface of about 3.5%, we observe an observable enhancement of the catalytic activity of this low-dimensional Pt relative to its bulk counterpart due to the compression from its graphene templated growth. In addition, samples seated on graphene have shown a higher Pt retention than those without, when subjected to long-term cycling experiments.

5.2 Enhancement of catalyst durability with graphene capping

5.2.1 Experimental section

In the presented study, Pt monolayers are electrochemically grown on 50 nm thick Au (111) thin films grown by electron beam evaporation, supported on glass substrates, using surface limited redox replacement (SLRR) as the primary synthesis method. Detailed methodology about Pt monolayer synthesis and Au films PVD are published elsewhere.[89] The study embodies three main sample architectures to examine the incorporation of graphene with Pt monolayers as a catalyst system. The first sample case consists of Pt monolayers grown without graphene (Pt_ML). The second case includes Pt monolayers grown on a graphene template (Pt_ML/GR), and

the third sample case includes Pt monolayers covered with a single-layer graphene placed on top (GR/Pt_ML).

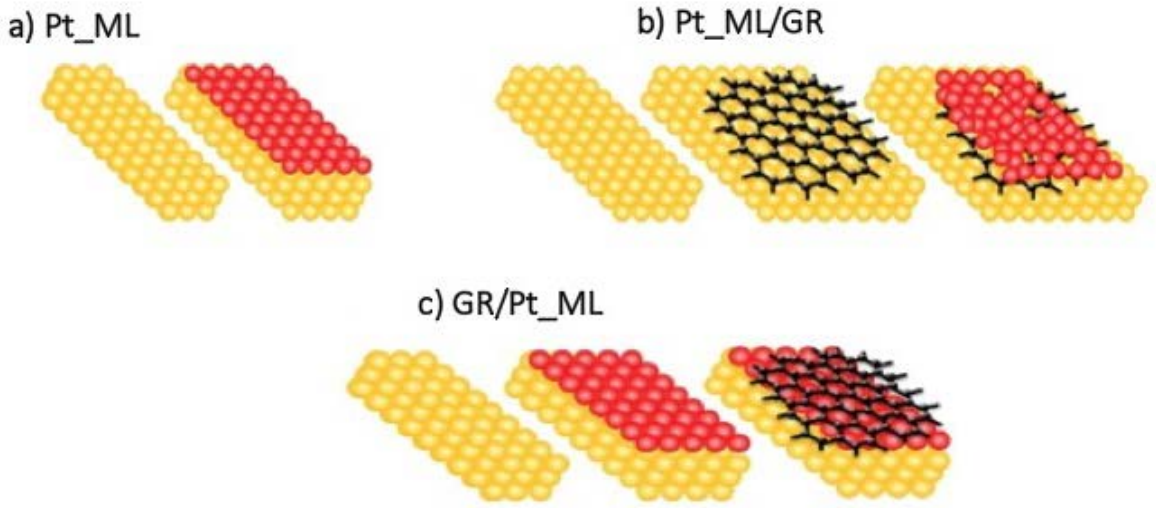

Figure 16: Studied samples architectures: a) Graphene-free Pt monolayers (red) electrochemically grown on (111) Au film (yellow) supported on a glass substrate. b) Pt monolayers grown on a graphene template at interface with Au substrate. c) single-layer graphene capping Pt monolayers.

ORR was probed through linear sweep voltammetry (LSV) for two sample sets with and without a single-layer graphene cap (i.e. GR/Pt_ML and Pt_ML, respectively) in O_2-saturated 0.1 M H_2SO_4. ORR polarization curves were generated by linearly sweeping voltage negatively from 800 mV to -100 mV (vs. Ag/AgCl). The resulting current achieved during the potential sweep has been attributed to the oxygen reduction reaction. By taking the first derivative of the ORR polarization curves, the peak position represents the inflection point of the current reaction curve and can be used to evaluate the required overpotential needed to catalyze the

ORR. Since a negative potential sweep (i.e. cathodic reaction probing) was used, the higher the reported potential values are for the first derivative peak position, the lower the required overpotential is for the ORR to take place. An overlay of the original ORR curves can be seen in Figure 2S of Supporting Information.

5.2.2 Results and discussion

5.2.2.1 Structural Analysis

In the previous chapter, we found that wetted Pt monolayers can be deposited on a graphene template supported by an Au substrate, in a wetted, layer-by-layer, fashion.[12] Here we explore the morphology at different length scales of the Pt_ML/GR structure using atomic force microscopy, AFM, (Figure 17a) and high resolution transmission electron microscopy, STEM, and associated simulations (Figure 17b-h). STEM analysis was performed in collaboration with Warner's group at Oxford University.

Surface roughness was measured by AFM for 3, 5 and 8 Pt monolayers (MLs) thick, electrochemically grown on a graphene monolayer supported on a glass substrate. Samples with surface thicknesses of 3 through 8 MLs showed an increase in the average root mean squared (rms) roughness from 2.6 to 3.1 nm. All AFM scans showed a fully wetted conformal coating of Pt MLs on the graphene surface. Taking the starting roughness of the graphene and glass substrate into account, the actual rms roughness of our 5 ML Pt film was found to be about ± 0.2 nm. In other words,

the layer-by-layer growth on graphene is smooth to about ± one atomic layer of Pt over at least 4 μm^2 regions (Figure 17-a). The change in surface roughness from 3 to 8 MLs confirmed the 2D wetted growth that avoids island formation or agglomeration (i.e. Ostwald ripening). Figure 17-i shows cyclic voltammograms (CV) of Pt_ML/GR sample case. Once the overlayer is around 4 ML in thickness, the Au reduction peak disappears in CV, which indicates an eventual total coverage of Pt over graphene. This observation shows that an ultrathin layer of Pt at 4 ML – roughly equivalent to ~1 nm thick, is able to fully mask the graphene template, i.e. pinhole free. The epitaxy with graphene further increases the activity of the monolayer catalyst for ORR (Figure 17-j). To our knowledge, this is the first reported full coverage of a metal on graphene at such low dimension over macroscopic surfaces areas (i.e. 1 cm^2),[89] and is believed to be directed by a graphene epitaxy. The finding opens the door to host potential applications beyond catalysis, such as in property-tunable transparent electrodes and atomically thin interconnects.

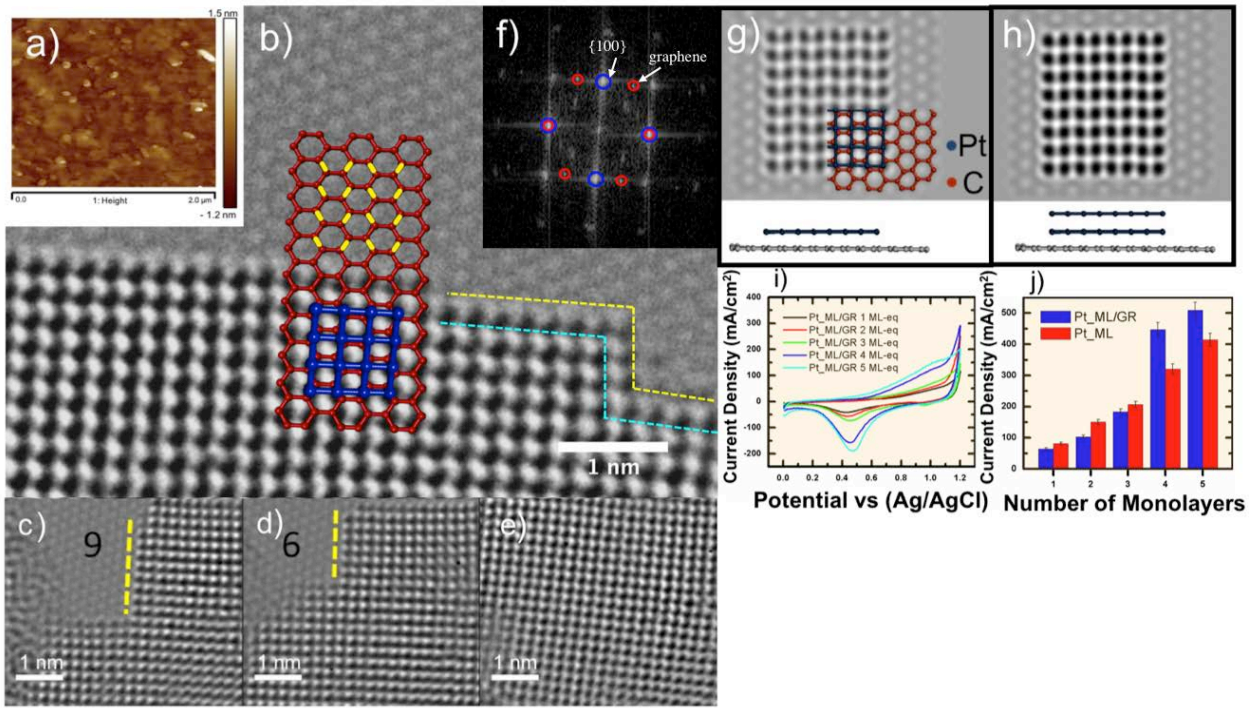

Figure 17 a) AFM over 2x2 µm for 5 ML of Pt on single layer graphene. b-e) Dark atom contrast TEM image of Pt ML on pristine graphene. b) TEM image of templated Pt ML on graphene (the growth front outlined by the yellow dotted line). A single-atom thick row of atoms is highlighted between the dashed turquoise and dotted yellow lines. Beyond that row, the stacking of the second layer atoms occupies atop positions over the first layer atoms. The superimposed red graphene lattice shows the Pt/GR registry with Pt occupying bridge sites (yellow for would-be and blue for actual locations) on graphene, along the zigzag and the armchair directions. c-e) Pt growth evolution with the leading-edge transitioning between 9 (c) through 6 (d) to zero (e) empty rows. f) Fast Fourier Transform (FFT) of TEM image with highlighted diffraction spots of graphene in red and {100} Pt in blue. g&h) Simulated phase contrast images of 1 and 2 ML thick Pt on graphene,

respectively, in {100} stacking. i) CV sweeps of Pt_ML/GR samples show the layer-by-layer evolution of Pt reduction peak ~0.45V and diminishing of Au reduction peak ~0.95 V with successive Pt MLs. j) ORR current density comparison of Pt MLs grown with or without graphene (i.e. Pt_ML/GR and Pt_ML, respectively), and the activity enhancement due to a graphene-induced compressive strain on Pt MLs.

STEM analysis of the Pt ML architecture on single-layer graphene provides insight into the Pt-GR bonding and the resulting epitaxial growth of Pt MLs. The dotted yellow line in Figure 17-b illustrates the atomically sharp edges and corners of the Pt growth-front that the graphene templating provided. The simulated red graphene lattice was overlaid on the graphene in Figure 17-b to illustrate how the Pt-GR registry was maintained throughout the Pt ML. The Pt atoms were seen to stabilize on the bridge site of above every other C-C bond in the zigzag direction and over each C-C bond in the armchair direction. These C-C bonds were highlighted in yellow and an example of Pt lattice that sits over these bonds is shown in blue. Based on phase contrast simulation, the contrast difference between a carbon with different number of Pt atoms on top (e.g. one and two Pt atomic-layer thick on top of a single-layer graphene, as shown in Figure 17-g&h, respectively) was established. Atoms in regions of one-layer thick (e.g. atoms between yellow and turquoise lines) can be differentiated form those in double layer stacking (e.g. beyond turquoise line). Beyond that row, the second layer atoms maintain the template of the first layer by occupying atop positions. This

stacking was seen over a mixed zone of 1-2 ML thick for 2-3 rows away from the growth front, beyond which a continuous 2 ML thick of Pt is observed over the remaining Pt layer imaged.

Figure 17-f shows the reciprocal space information obtained by an FFT of TEM image shown in Figure 17-b. The graphene diffraction pattern aligns with the Pt {100}, supporting observation from Fig. 17-b that graphene provides an epitaxial template for Pt atoms growth. Though the more efficiently-packed {111} planes, when stacked, would evolve the bulk face-centered cubic (FCC) structure of Pt, a marked absence of {111} diffraction spots were observed for one and two Pt monolayers thick. Due to epitaxial stabilization from graphene, the first two layers of Pt resist a transition away from the {100} stacking even at the cost of having lower Pt-Pt coordination (4 and 5 for single and double layers, respectively) relative to the close-packed {111} arrangement (6 and 9 for the single and double layers, respectively). Our Pt_ML/GR architecture opens the door to grow atomic-thin and wetted metal layers on 2D or 3D (i.e. foam-like) graphene with and without support, that can be transferred to a plethora of substrates[90] for various applications.

5.2.2.2 Structure-property relationship

In order to investigate the role of graphene capping on the catalytic activity of Pt monolayers catalysts, electrocatalytic activity towards ORR was investigated. For GR/Pt_ML samples, despite the Pt overlayer surface being fully capped by graphene, it was able to catalyze the ORR with no additional energy barrier. A reflection of the

energy barrier is the onset potential of ORR. The description of the method for identifying the onset potential is provided at supporting information. In both the GR/Pt_ML and Pt_ML cases, the onset potential shifted positively as the number of Pt MLs increase, which is equivalent to a lower overpotential required to catalyze the ORR. For 1, 2, and 3 Pt MLs, the onset potential value of the GR/Pt_ML samples lies at a higher positive potential than corresponding Pt_ML samples. At 4 and 5 MLs, the two samples share similar overpotential values. This indicates that the presence of graphene at the surface of the Pt has either a beneficial or no harmful effect on the required overpotential towards catalyzing the ORR. Results are depicted by blue triangles in Figure 4-b. GR/Pt_ML sample of 5 atomic layer thick showed showed similar ORR current density, however, with a slight negative overpotential than state of the art Pt-carbon commercial catalyst. This can be attributed to difference in samples nature. Pt-carbon commercial ink contained nafion which is widely known to enhance ORR activity due to better conductivity and contact of ORR species with the catalyst active sites, however GR/Pt_ML was tested for ORR without nafion.

In order to further investigate the surface chemistry of the monolayer catalyst platforms, X-ray photoelectron spectroscopy (XPS) was used to evaluate the electronic state of Pt MLs. Noticeable shifts can be seen in the binding energies of the Pt $4f_{7/2}$ photoemission for both sample sets as seen in Figure 18-b. The Pt_ML sample set showed a slight shift towards lower binding energies with increasing number of Pt monolayers, flattening out within a .05 eV margin of error at around 71.15 eV. On the

other hand, GR/Pt_ML samples exhibited significantly lowered binding energies in all cases. The lowest binding energy is at ~70.8 eV for the 1 ML sample (~0.4 eV lower than its graphene-less counterpart), but this energy shifts higher with the addition of Pt, as seen in Figure 18-b insets. This decrease in binding energy for GR/Pt_ML samples can be explained by considering charge transfer. With this architecture, it is expected that graphene will have a net donation of electron density to Pt.[85] Such a transfer would affect the electron charge of the Pt monolayer shell, which creates a negative shift in its effective binding energy (i.e. to lower binding energy values), as measured in XPS. When only a single Pt ML is present, this negative shift was most significant as seen in Figure 4-b. As the Pt layer grew in thickness, the cumulative effect of this electron density transfer was diminished and nearly vanish by the 5th monolayer.

These binding energies for GR/Pt_ML samples can correlate with the advantage in ORR overpotential as discussed earlier. Lower Pt 4f binding energies indicate a metal *d* band shift towards the Fermi level, which can lead to higher activity by enhancing the kinetics for ORR.[84] Others have shown that changes in the d-band structure can be obtained indirectly using shifts in XPS core-level binding energies that are sensitive to d-band structure[91], but we take it further a step further. We show that the shifts in Pt 4f binding energies, directly controlled by the dimensionality of Pt_ML catalysts in the presence/absence of graphene, and corresponding shifts in ORR overpotentials can be made. Figure 18-b shows how for each monolayer sample comparison, lower binding

energy correlates to a positive shift in ORR overpotential, as depicted in green squares. Since adsorption of oxygen species plays a major role in determining the kinetics of ORR at Pt electrodes, maintaining access of Pt atoms to the electrolyte is necessary. Our data shows that the epitaxy between graphene and Pt allow the Pt atoms to be in sufficient electronic intimacy through the graphene with the incoming ORR reactant species, and the graphene-Pt hybrid surface is able to catalyze oxygen at an overpotential advantage when compared to a bare Pt surface.

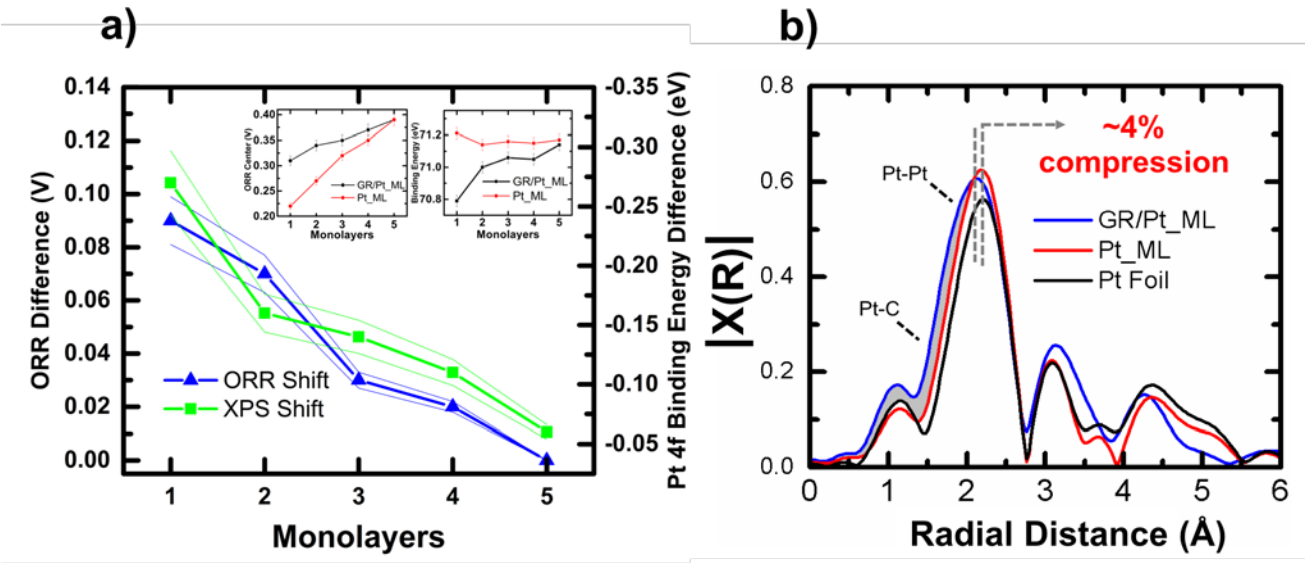

Figure 18 a) The difference in Pt 4f binding energy (blue triangles) plotted with the difference in ORR overpotential (green squares) between GR/Pt_ML and Pt_ML samples. Outer thin lines indicate a 10% margin of error. 4-a Left inset) XPS binding energy for each sample. 4-a Right inset) ORR overpotential for each sample. b) Real-space EXAFS spectra comparing 5 MLs of Pt with and without a single-layer graphene cap to that

of a reference bulk Pt foil. The local structure of the GR/Pt_ML and the Pt/ML samples matches that of FCC Pt (Pt foil), with the former showing a compressive strain of ~4% and also exhibiting a shoulder due to Pt-C bonds (marked grey).

Strain tuning of Pt monolayers, particularly inducing compressive strain on Pt-Pt atomic bond, has been of a great interest due to its associated electrocatalytic enhancement, especially for ORR. Two major research routes have been under investigation to engineer the strain induced on Pt adatoms: first, alloying Pt with other metals (e.g. first row transition metals[92] or Lanthanides[93]). Second, modifying the catalyst support (e.g. graphene[12], metal-oxide[94], metal-nitride[95]). Eelectrocatalytic enhancement following those two routes can be attributed to crystal mismatch between Pt and its vicinity through dictating Pt growth following the underlayment substrate epitaxy, respectively. Extended x-ray absorption fine-structure (EXAFS) was used to measure the average local atomic structure around Pt atoms. In Figure 18-a, bulk Pt (i.e. Pt foil) exhibited an observed nearest Pt-Pt nearest neighbor (nn) Pt-Pt distance, which was well aligned at the same position for Pt-Pt nn of 5 Pt_ML sample. However, for the GR/Pt_ML samples, the nn peak was shifted towards a lower value that translated to a compressive strain of the Pt-Pt nn by ~4%. ur previous work showed that compressive strain can positively affect Pt catalytic. There was also a widening of GR/Pt_ML peak on the lower-distance side (shaded in grey) where the Pt-C bond is expected, as an indication about Pt-graphene chemical bonding. This

bonding can be the source of the observed strain as the Pt followed the graphene templated epitaxy.[12] The structure beyond the nn peak is still very similar to that of Pt foil indicating that Pt MLs overall strive to obtain a face centered cube-like close-packed structure.

5.2.2.3 Catalyst Durability

Catalyst platforms were subjected to accelerated durability tests (ADT),[12] experimental details can be found in supporting information. XPS spectra of the samples before and after 1000 cycles were taken to evaluate the surface architecture of each sample. Because our sample architecture is that of a Pt-Au core-shell, by comparing the relative photoemission intensity of the Pt overlayer to the underlying Au photoemission, the relative average thickness of the Pt shell can be determined. Figure 19-a shows a comparison of before/after ADT of GR/Pt_ML and their Pt_ML counterparts. After 1000 cycles, the XPS spectra for the GR/Pt_ML samples were almost identical to their spectra prior to ADT, as the peak intensity for the Pt 4f was unchanged relative to that of the Au 4f. This indicates the Pt atoms remain pinned to their original lattice on average, resulting in high resistance to both dissolution but ripening. On the other hand, Pt_ML samples without graphene clearly showed dramatic reduction in Pt peak intensity relative to Au. This indicates that, in the Pt_ML case, the Pt overlayer was on average much thinner (i.e. a large amount of Pt loss and/or ripening occurred due to ADT). The results here clearly show that the graphene

cap works to effectively lock the Pt atoms in place, and dramatically improves the retention of Pt at a variety of monolayer thicknesses.

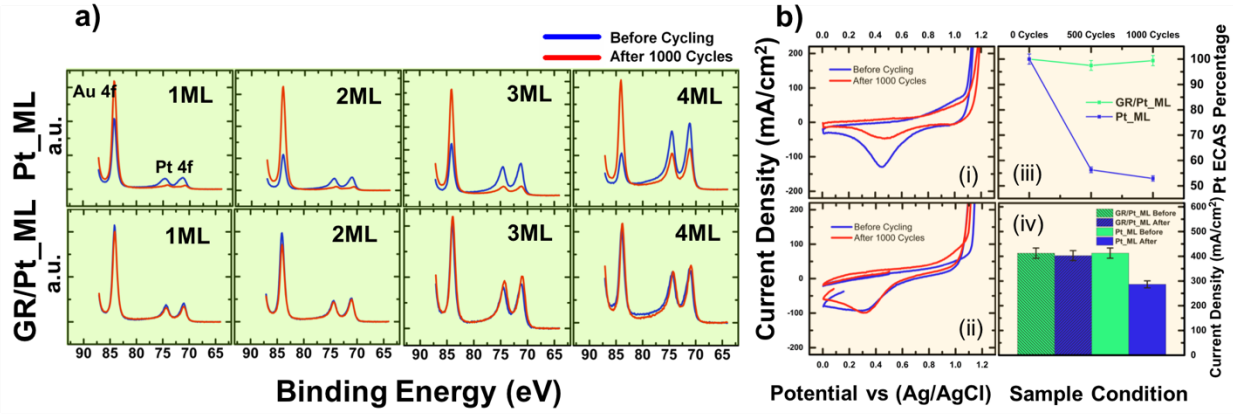

Figure 19 a) The Pt $4f_{7/2, 5/2}$ pair and the Au $4f_{7/2}$ XPS spectra for GR/Pt_ML samples and Pt_ML samples are shown before and after ORR cycling. b) (i & ii) CV sweeps before and after cycling for 4 ML GR/Pt_ML and 4 ML Pt_ML sample, respectively. (iii) ECSA percentage of Pt monolayers depicted from CV scans represented in (i&ii). (iv) current density obtained from LSV sweeps before and after 1000 cycles, indicates Pt monolayer activity towards ORR.

Integrating the Pt reduction peaks from cyclic voltammetry (CV) scans provided a representation of the amount of active Pt on the surface. GR/Pt_ML samples showed enhancement of ECSA and catalyst durability after 1000 cycles by 43% and 170%, respectively, compared to Pt-carbon commercial catalyst, as shown in Figure 20.

Results for the 4 ML sample are shown in Figure 19-b. GR/Pt_ML samples showed that the reduction peak of Pt was maintained during 1000 cycles, however, Pt_ML samples showed significant decrease of the peak area, indicating a significant amount of electrochemical active surface area (ECSA) loss due to Pt dissolution into the electrolyte. ADT test was performed in H_2SO_4 acidic medium, which is known to promote an indirect two-electron ORR mechanism with H_2O_2 as intermediate species that degenerates the Pt electrode.[96] Despite the presence of this corrosive environment, graphene showed excellent protection to Pt with minimal or no loss up to 1000 cycles. These initial harsh cycling results show a promise for using graphene-capped as a protection for extended ADT. Linear potential sweeps investigating the ORR also showed about a 30% decrease in current for the 4 ML Pt_ML samples after cycling, while GR/Pt_ML counterpart maintained its ORR current as seen in Figure 5-b (iv). In corroboration with the XPS results shown in Figure 19-a, it is clear that the graphene acting as a transparent catalytic barrier for Pt monolayers dissolution.

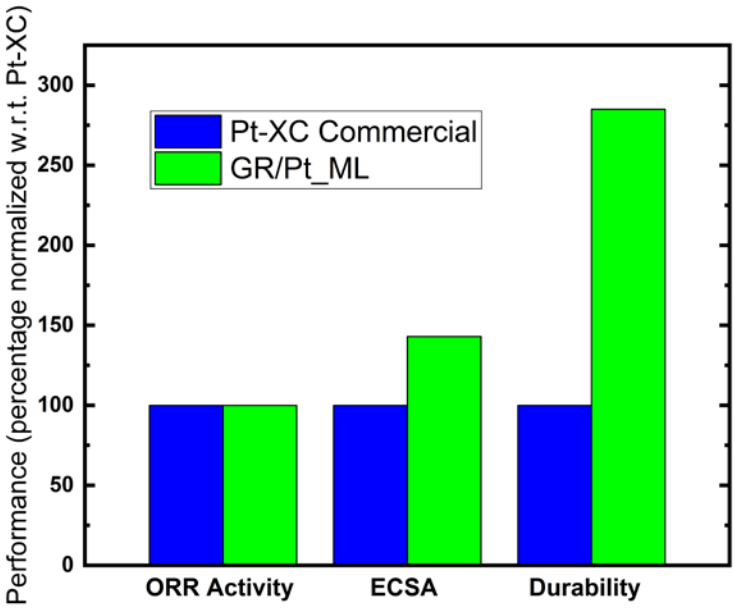

Figure 20 Comparison between Pt-carbon commercial nanoparticles (Pt-XC Commercial) and 5 atomic layer thick Pt capped with graphene (GR/Pt_ML). For each comparison, Pt-XC commercial was set as a reference with 100% performance and GR/Pt_ML was evaluated accordingly.

A new paradigm has been demonstrated for graphene-templated, wetted, dimensionally-tunable, atomically-thin catalyst system that is support-flexible in design. We show systems with monolayer to few multilayers of Pt (Pt_ML) sharing an interface with single-layer graphene (GR), and find that epitaxial nature of the interface imposes a compressive strain on the Pt that lowers the required overpotential for ORR at thinner Pt loading (4 ML or less). At the same time, the epitaxy renders the Pt_ML/GR or GR/Pt_ML system to be one electronically-coupled catalyst system that exhibits no sacrifice in activity when reactants approach from the

GR end. From the perspective of the reactants, the GR capping layer is 'chemically transparent' that provides 'infinite' resistance to activity loss from Pt dissolution, agglomeration through Ostwald ripening, and carbon corrosion (graphene, in our case), as evidenced by no activity loss within 1000 ORR cycles (within measurement errors). These combined results show obvious promise for incorporating graphene as a template at various catalyst interfaces as a catalyst support and as a surface cap that restrains catalyst loss down to negligible amount that can help transcend the activity-stability dilemma.

5.3 Atomic Scale Metal-sandwiched Graphene Architectures: Cultivating the Catalytic Activity & Transcending Catalyst Stability for Oxygen Reduction Reaction

Tremendous increase in energy demand over the past few decades, associated with an enormous increase in CO2 emissions directed the efforts towards enabling renewable energy harvesting and/or storage. Fuel cells converts chemical energy into electricity is a promising candidate, however, technological challenges yet to be resolved, before technology widespread at a commercial level[9]. Low temperature fuel cells operate below 100 °C (e.g. Proton Exchange Membrane (PEMFC)) have a great potential for mobile applications. Oxygen Reduction Reaction (ORR) is a typical electrochemical reaction at the cathode side of PEMFC, which suffers from sluggish kinetics rate. A catalyst addition is essential to lower the activation energy barrier for ORR. Immense research efforts have been presented to optimize ORR catalyst, where highest performed catalyst is based on Pt and Pt-group metals elements. Nevertheless, three major shortcomings, associated with ORR catalyst, are hindering PEMFC from dominating the market: a) low performance, b) poor stability and c) high cost[97–99].

Numerous efforts have been presented to enhance ORR catalyst activity and lifetime. Alloying of Pt-based catalyst with secondary metals (e.g. Co[100,101] , Pd[13,102] or Ni[32,103]) or forming a core@shell[50,104,105] structure where Pt resembles the shell layer and secondary metals act as a core support. Nevertheless, the aforementioned architectures showed enhancement of ORR activity, secondary metals suffered from

low stability at harsh acidic and oxidizing working potentials of PEMFC. Therefore, metals leached out into the electrolyte, causing the catalyst structure to collapse, which entails significant deterioration of performance due to loss of electrochemical active surface area (ECSA)[40,45,49,57]. Moreover, Pt-based catalyst suffered from low stability due to rapid corrosion of carbon catalyst-support. Hence, nanoparticles are either washed away into the electrolyte or agglomerate into bigger nanoparticles, where both mass loading and ECSA dramatically decrease[99].

Graphene has shown great promise to replace conventional carbon black catalyst supports due to mechanical robustness and chemical stability against most of acids[72]. Recent efforts demonstrated graphene utilization as a support which enhanced catalyst activity due to inducing compressive mechanical strain on catalyst adatom[12,39]. In addition, Graphene provided a template for large-area catalyst growth at atomic scale thickness without ripening. Moreover, graphene showed promising enhancement of catalyst lifetime when used as a cap protecting catalyst material underneath[30]. Results demonstrated that single layer of graphene can transcend catalyst lifetime with no penalty to ORR activity. Graphene is thin-enough, forming a hybrid catalyst with Pt atoms underneath, without blocking reaction intermediates interaction with Pt catalyst[30].

In the presented thesis, we are demonstrating the utilization of graphene as a sandwich (i.e. support and cap) for mixed single atomically dispersed and ultra-small

Pt nanocatalysts. Herein, we examine the effect of graphene thickness on catalyst stability and electrocatalytic activity for ORR. A combination of experimental and computational analysis presented to unravel the degradation mechanism of ECSA and identifying the origin of electrocatalytic activity enhancement.

5.3.1 Experimental Section

Copper foil 20 μu thick was cleaned by immersing for 10 min in glacial acetic acid to remove native oxide layer, followed by successive washing under De-Ionized water. CVD chamber is pumped down for 10 minutes, before Cu foil is heated to 1000 °C with a ramping rate of 7 °C/min under a mixture of Hydrogen/Argon (37/63, respectively). Afterwards Cu was annealed at 1000 °C for 30 minutes, before introducing CVD gas mixture ($CH_4/H_2/Ar$). controlling the reaction gases ratios and CVD time enabled fine-tune of graphene thickness (e.g. 1, 3 and 5 layers thick). Finally, temperature is ramped down with an effective rate of 3 °C/min under a stream of H_2/Ar of 2/10, respectively. Graphene transfer on gold stubs was performed by etching copper foil in acid bath published elsewhere.[12]

Pt (99.99%) target was used for sputtering under room temperature on Graphene supported on gold stubs. The sputtering chamber was pumped down to $4e^{-5}$ Torr and kept under vacuum for 1 hour. DC-magnetron sputtering was performed at 3.4 e^{-3} Torr and 3-Watt DC power for 26 seconds, yielding an effective deposition 1 $\mu g/cm^2$. Following, graphene capping layer was transferred on top of Pt nanoparticles. Three different graphene-cap thicknesses were used (1, 3 or 5 layers thick), denoted as shown in the following table.

Table 1: Sample annotation of graphene/Pt/graphene sandwich structure

Notation	Graphene support layer number	Graphene cap layer number
GR1/Pt/GR	**3**	**1**
GR3/Pt/GR	**3**	**3**
GR5/Pt/GR	**3**	**5**

Electrochemical measurements were performed in 3-electrode setup with a graphite rod and Ag/AgCl as counter and reference electrodes, respectively. Accelerated durability testing (ADT) and Oxygen Reduction Reaction probing were measured in 0.1M HClO4 electrolyte, saturated with nitrogen and oxygen, respectively. ADT was performed using CV scans 0.4-0.8 V vs Ag/AgCl as a scan rate of 50 mV/s. Changes in ECSA during ADT were investigated by tracking hydrogen adsorption/desorption waves (Hupd) at both positive and negative sweeps at the interval of -0.2:0.0 V vs Ag/AgCl by integrating area under the peak. ECSA was tracked after 1, 5, 10, 15 and 20K cycles. ORR was probed at rotating disk setup (RDE) at 1600 rpm, using liner sweep voltammetry (LSV) 0.9:-0.1 V at a scan rate of 10mV/s.

5.3.2 Results & Discussion

Three sample sets synthesized with Pt ultra-small nanoparticles sandwiched between two graphene sheets (GR/Pt/GR), as shown in Figure 1. Bottom sheet (i.e. support) is 3-layers thick graphene for all cases of studies, while top sheet (i.e. protective cap) varied from 1, 3 to 5-layers thick graphene, each represents a sample set. Table 1 gives a notation for each sample set, as will be referred to in the presented thesis herein.

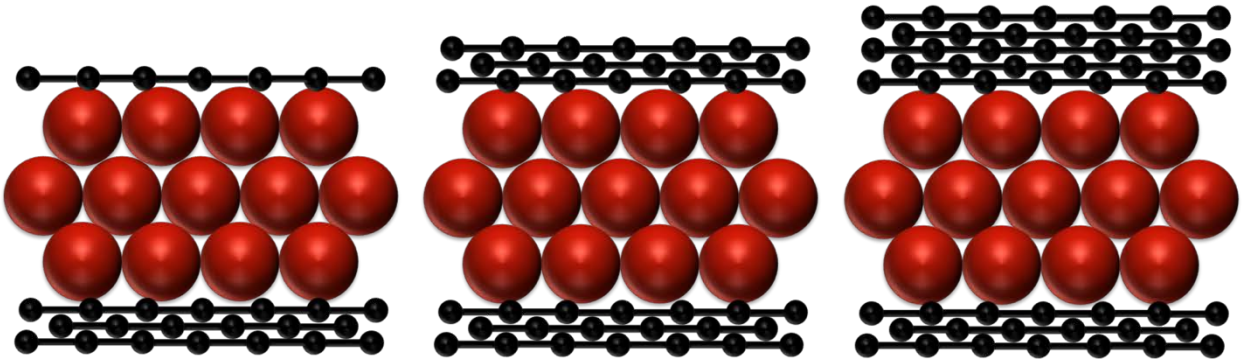

Figure 21: Pt-sandwiched graphene structure with different graphene-thick layers (black) covering Pt-adatoms (red spheres)

5.3.2.1 Structural Analysis

GR/Pt/GR sandwich structure was investigated using High Resolution Transmission Electron Microscopy (HRTEM) and Scanning Transmission Electron Microscopy (STEM) (accelerating voltage 300 and 200 KeV, respectively) to unravel the morphology of Pt adatoms and their distribution on 2D graphene films. Sputtering

power and deposition time were varied incrementally to monitor the growth mode of Pt nanoparticles on graphene. A set of samples was sputtered for 6, 15, 26 and 60 sec at 3-Watt power. Results shown in Figure 22-a shows a high mono-dispersity of the deposited Pt nanoparticles, with abundance of spherically shaped nanoparticles. The sputtering deposition time affected the density of the particles loading (i.e. particles coverage on graphene surface), rather than particle's size. TEM images showed Pt with a shape of rod-like interconnects (i.e. multi-pods). Statistical analysis of TEM images showed an average particle size of 2.19 nm, where vast majority (~79%) of the particles had a diameter range 1.6-2.4 nm.

Fast Fourier Transform (FFT) analysis of STEM images showed that Pt nanoparticles grew along (110) and (111) crystal orientations, both known to possess higher electrocatalytic activity for ORR [23,106]. Multi-pods interconnects (Figure 22-d) were observed with polycrystalline structure. This, hypothetically, infers that Pt nanoparticles started growing as spheres initially, before Pt nanoparticles within close proximity merged together forming multi-pod interconnects. The observation of Pt-Pt lattice parameter deduced from STEM and FFT analysis Figure 22-b, along with the literature [30,39], suggests Pt epitaxial-growth, dictated by the graphene honeycomb structure. Pt preferred to be deposited at the bridge site between C-C bonds.[12,30,39] The interplanar distance deduced from FFT (inset Figure 2-b) of Pt adatoms showed a compressive strain with shorter Pt-Pt bond distance. The induced compressive strain on Pt adatoms have shown an effect towards enhancement of ORR activity [12,30,39,107].

Successful synthesis of GR/Pt/GR sandwich structure was confirmed by HRTEM imaging. Figure 22-c shows a bent cross-section edge of the sandwich structure with two graphene sheets (top and bottom with 5 and 3-layers graphene thick, respectively) highlighted with green and red brackets. FFT inset of Figure 22-c shows two sets of hexagonal diffraction patterns which were attributed to miss-oriented top and bottom graphene sheets of the sandwich structure (highlighted in red and green circles) [108–110]. In addition, each hexagonal diffraction pattern showed diffuse rather than sharp diffraction spots, as an indication of miss-alignments of each layer of graphene within top or bottom sheets (i.e. carbon atoms of a graphene do not maintain a top position on adjacent carbon atoms of other graphene layers within the same sheet).

STEM analysis of GR/Pt/GR sandwich structure showed a very interesting observation consistently. All Pt nanoparticles, disregard of their morphologies, showed a halo of individual Pt atoms surrounding particles' periphery. This observation implies the high stability of GR/Pt/GR sandwich structure. Samples were subjected to 300 and 200 KeV for 2 hours, with 10 days apart, however single atomically dispersed Pt halo remained intact. This promises with high stability when using sandwich structure for encapsulating single atom materials, which can have interesting applications, not limiting to electrocatalysis. The aforementioned observation indicating the existence of a mixture single atomically dispersed and ultra-small nanoparticles Pt which are supposed to increase the density of catalytically active sites. This is plausible to have significant influence effect on electrochemical performance of GR/Pt/GR sandwich structure as will be discussed in the following sections.

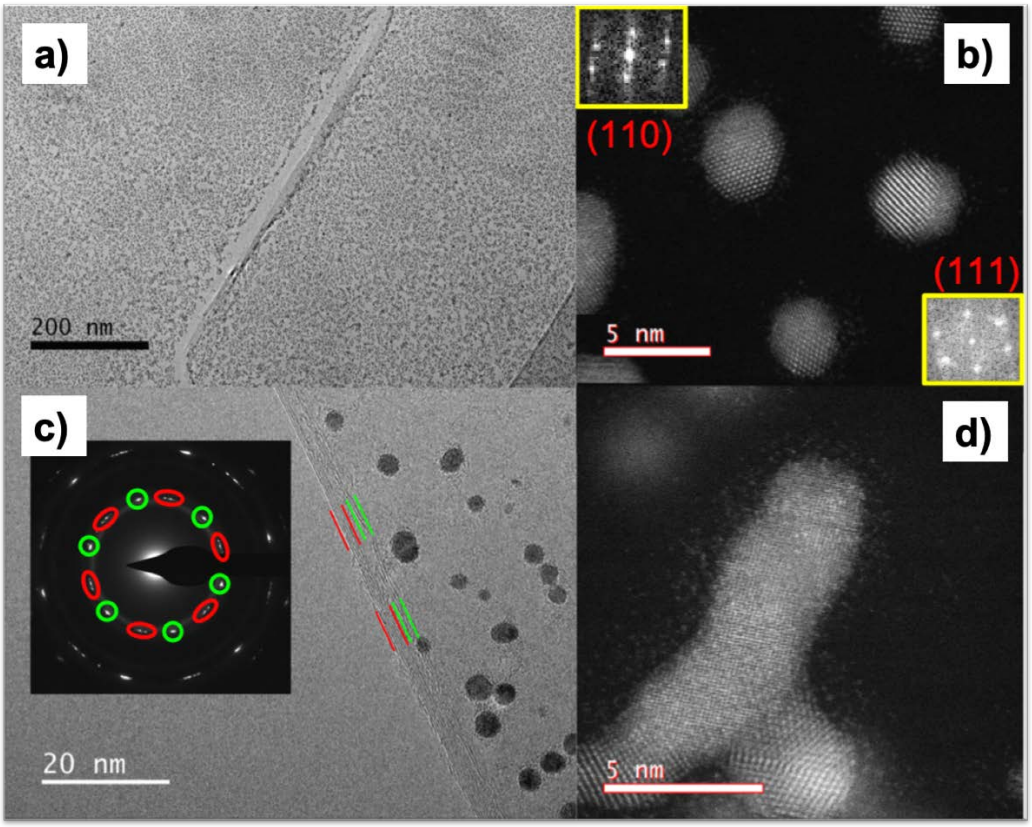

Figure 22: (a) TEM image showing monodispersity and high-coverage of GR/Pt/GR sandwich structure with Pt sputtering for 26 seconds. (b) STEM image of Pt spherical nanoparticles with FFT insets showing Pt growth along (111) and (110) crystal orientations. (c) Bent-edge showing a cross-section of GR5/Pt/GR sandwich structure with top and bottom graphene sheets highlighted with pairs red and green lines. FFT inset showing superimposing two distinct hexagonal diffraction patterns for top and bottom graphene sheets, each highlighted with green circles and red ovals. (d) STEM imaging shows a halo of single atomically dispersed Pt atom surrounding Pt interconnects (multi-pod) periphery.

5.3.2.2 Electrochemical Stability Testing

Electrochemical Active Surface Area (ECSA) was tracked through observing changes of hydrogen waves (H_{upd}) peaks area (0.0 : -0.2 V vs Ag/AgCl as a ref electrode)[39,89,111,112]. Electrochemical testing was performed in a nitrogen saturated 0.1M $HClO_4$. Cyclic voltammetry (CV) characterization scans were obtained at a rate of 50 mV/s from -0.2 : 1.2 V vs Ag/AgCl. Accelerated durability testing (ADT) was performed following department of energy (DOE) protocols: CV 0.4:0.8 V with a scan rate of 50 mV/s [30,39,89,112]. Direct comparison between state-of-the-art commercial Pt/carbon (HISPEC4000) with GR/Pt/GR sandwich structure showed superior catalyst stability for our sandwich structure for all graphene-cap samples with different thicknesses. ADT results showed good stability for GR1/Pt/GR sandwich structure, surviving ~78% of ECSA after 5K cycles, however, ECSA suffered from rapid ECSA loss in the subsequent cycles up to 15K cycles, as depicted in Figure-23. This is plausible due to presence of defects within graphene, as will be discussed in detail with an aid of an ex-situ Raman analysis.

ADT results showed tremendous stability of GR3/Pt/GR sandwich structure with ECSA increasing by 7% during first 5K testing cycles. Sandwich structure with 3-layers graphene survived 84% and 75% of ECSA after 15 and 20K ADT cycles. This result is a key feature towards establishing state of the art catalyst platforms for oxygen reduction reaction application, where catalyst lifetime is prolonged. Sandwich structure with 5-layers graphene thick (GR5/Pt/GR) showed an interesting and different behavior from other GR/Pt/GR sandwich structures counterparts during ADT cycles. Through CV scans before ADT, no H_{upd} was observed, similarly no observation of Pt-O

reduction peak (0.4:0.6V) were cited, however, XPS analysis confirmed Pt presence within the surface vicinity. Increasing ADT cycles showed pronounced Pt-O reduction peak around 0.45V, with signal enhancement monotonically with ADT cycling up to 30K cycles. Simultaneously, no H_{upd} was observed before ADT cycling or after 30K cycles.

The aforementioned observation is well aligned with literature reports [111,113–115]; as single atomically dispersed Pt catalyst possess a fast hydrogen-spillover rate, which eliminates the observation of H_{upd}. Pt nano-clusters sandwiched between two graphene sheets (i.e. top and bottom bands) are protected by top graphene band, which acts as a shield suppressing Pt atoms dissolution in the electrolyte. During ADT, graphene suffered from rupture due to harsh acidic and oxidizing potential, where point defects were introduced as carbon atoms removed from graphene's structure. Thicker graphene (i.e. 3 and 5-layers band) slow down the severity of ORR, providing more barriers to reach bare-Pt surface, which better describes the longevity of catalyst lifetime inferred from ADT analysis depicted in Figure 3. Nevertheless, point defects provide a pathway for Pt single atoms to hop through vertically between graphene layers till reaching sample's surface, before being washed away in the electrolyte. GR5/Pt/GR showed no observation of H_{upd} up to 30K cycles, which shows graphene robustness as a shield protecting bulk Pt (i.e. nano-clusters) from accessibility of H^+, where Pt-O reduction peak charge can be attributed only to single atomically dispersed Pt atoms hops through top layers within the graphene cap. As an agreement with the aforementioned hypothesis, observed ECSA increase of GR3/Pt/GR sandwich structure up to 5K cycles with 7%, indicates Pt nanoparticles rearrangement between

top and bottom graphene sheets (i.e. cap and support). To our favor, Pt rearrangement occurred in a non-agglomeration fashion (i.e. ripening-free), where Pt atoms preferred to wet graphene sheets instead, in agreement with early reported observation of Pt-graphene epitaxial intimacy [30,39]. To validate the proposed hypotheses, ex-situ Raman analysis was performed within electrochemical ADT cycles and will be discussed in the following section.

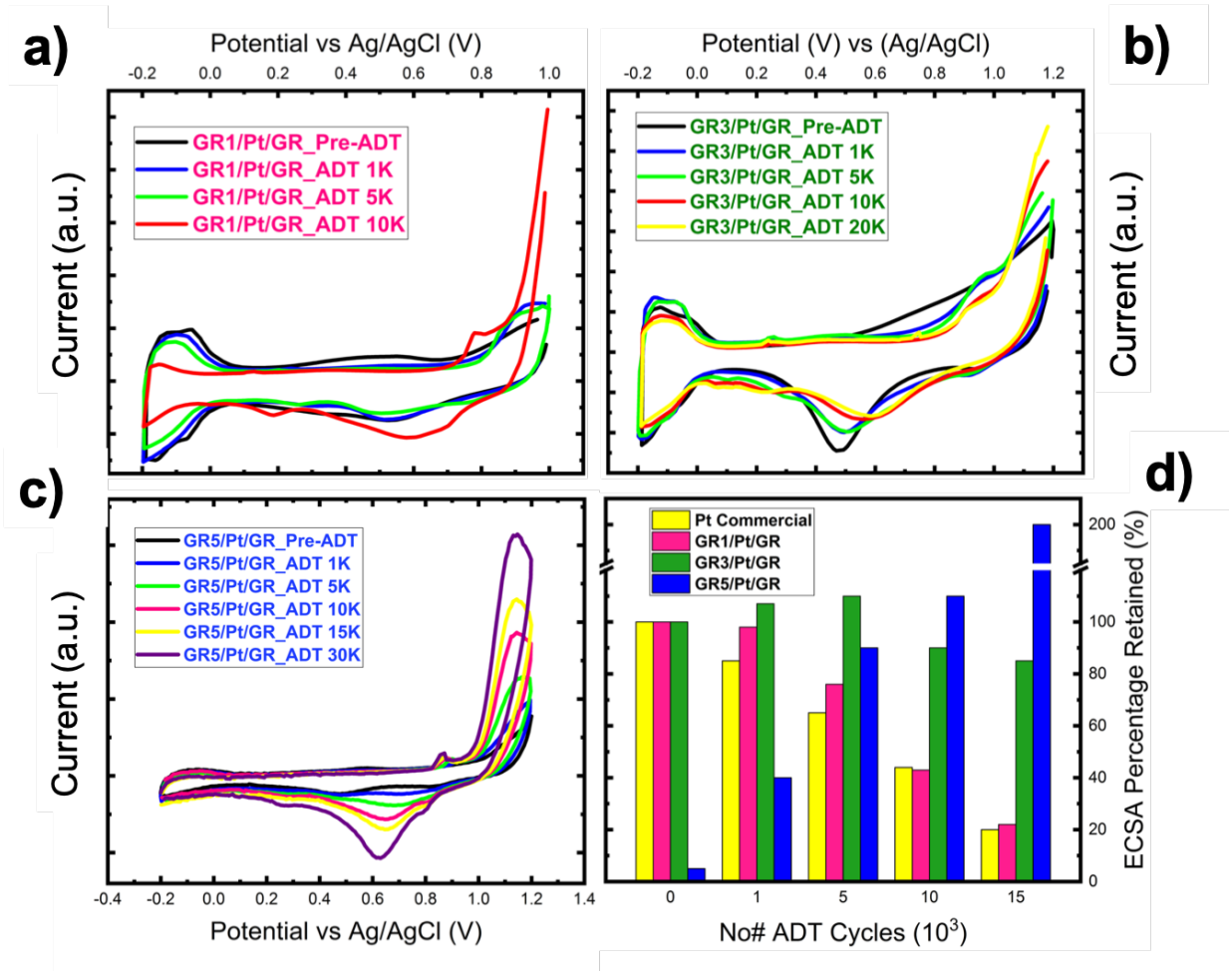

Figure 23: a-c) Cyclic voltammetry scans of GR/Pt/GR sandwich structure with different graphene cap thickness 1, 3 and 5, respectively. (d) Bar-chart of ECSA percent change with ADT cycling comparing different graphene thicknesses to the stability of state-of-the-art Pt/carbon commercial catalyst

5.3.2.3 Ex-situ Raman Analysis

Sandwich structure capped with single-layer graphene (GR1/Pt/GR) experienced a blue shift of 2D-peak towards lower Raman shifts. Blue shift observed for 2D-peak of GR1/Pt/GR can be attributed to compressive strain induced on graphene

structure (i.e. C-C shorter bond distance) due to asymmetric nature or graphene under strain [116–118]. This observation was validated by examining C 1s peak position from X-ray photoelectron spectroscopy (XPS) which shifted towards higher binding energies, in a similar observation to Ganesan et al [117]. Graphene is believed to reorient to form an epitaxial intimate bond with Pt adatoms. Similar behavior was observed through Extended X-ray Absorption Fine Structure (EXAFS) with Pt-Pt bond distance compressed and Pt-C bond evolved; indicating chemical covalent bonding between Pt and carbon of graphene [12,30].

Ex-situ Raman analysis performed during ADT cycles at intervals similar to ECSA analysis reported earlier (i.e. before ADT, 1K, 5K, 10K). Ex-situ Raman analysis showed shifts of graphene's 2D-peak towards higher Raman shifts (i.e. red shift) with ADT cycling, as shown in Figure-24. Pronounced red shift was observed systematically for GR1/Pt/GR with increasing ADT cycles. Raman analysis of 2D-peak for GR1/Pt/GR sample after 10K cycles showed a shift of ~77 cm^{-1} compared to 2D-peak position before performing ADT. ADT is believed to introduce point defects, which was observed by an increase in D-peak intensity, relative to constant G-peak.[119–121] Single layer mask showed significant change in graphene nature after 1K cycles, with IG/I2D increased significantly [119–121]. Point defect presence within graphene is thoughtful to decompress graphene samples, providing more relaxation for carbon atoms in the vicinity of the defect. However, 2D-peak of GR3/Pt/GR sample showed similar behavior to single layer graphene-covered GR1/Pt/GR, but Raman shifts was lower (less than 10 cm^{-1}) which might fall within measurement error.

GR5/Pt/GR sandwich structure with 5-layers graphene thick showed an opposite trend, where Raman 2D-peak shifted towards lower Raman shifts with cycling up to 30K cycles. GR5/Pt/GR 2D-peak was shifted by ~71 cm^{-1}. In addition, D-peak intensity increased significantly after 10K cycles, indicting presence of enormous amount of point defects within graphene's honeycomb structure.[119] D-peak intensity increased by a total of ~4.6 folds after 30K ADT cycles. Blue shift, as described earlier, is attributed to graphene compression, however, point defects density is increasing. On the other hand, 2D-peak of graphene reported to be affected by the number of graphene layers. Monolayer graphene thick reported to have 2D-peak at lower raman shifts, while 2D-peak position red-shifts systematically with increasing graphene's thickness (i.e. 2D-peak position order: Monolayer < Bi-layer < Tri-layer graphene) [122]. Therefore, our observation of 2D=peak blue shift (i.e. to lower raman shifts) with ADT cycles for GR5/Pt/GR can be attributed to increasing the amount of Pt single atoms intercalating/diffusing between graphene sheets. Thus, two possible scenarios can be present: first, larger Pt atoms, compared to carbon, squeezed within defect site inducing localized compressive strain on graphene. Second, Pt intercalation increased the interplanar distances between graphene layers, where 5-layers graphene behave as free-float monolayer graphene.

Raman analysis supports our hypothesis mentioned earlier about the electrochemical performance observed for GR5/Pt/GR with absence of H_{upd} signal [111]. As defect's density increased, more Pt single atoms were stimulated to hop through graphene. Hence, single Pt atoms trapped within graphene defect site or intercalated between graphene layers at the surface vicinity acted as a catalytic spot for

electrochemical ORR. Concerned about prolonged catalyst durability, GR5/Pt/GR after 30K ADT cycles reserved the relative intensities of G/2D peaks, indicating that graphene preserving its nature regardless of defects presence [119–121]. This is a plausible demonstration of using graphene as a catalyst-support, replacing easily-corroded and unstable commercial carbon black (e.g. Vulcan XC/72R), which entails boosting catalyst lifetime with both aspects of graphene: as a support and a spectacular protective cap.

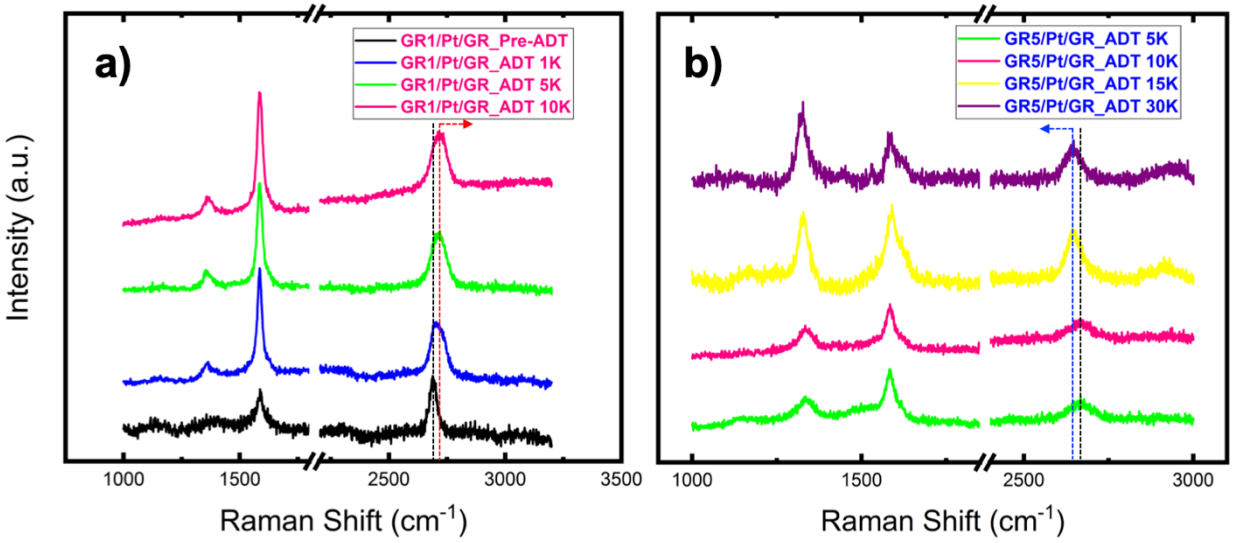

Figure 24 Ex-situ Raman analysis performed during ADT to investigate structural changes in graphene: (a) GR1/Pt/GR 2D-peak shifting to higher Raman shifts with ADT. In addition to, increase of D-peak intensity and IG/I2D ratio after 1K ADT cycles. (b) GR5/Pt/GR showing 2D-peak shift to lower Raman shift with ADT cycling. In addition, D-peak increased significantly after 10K ADT cycles.

5.3.2.4 Computational Analysis

Density Functional Theory (DFT) was used to investigate the atomic migration of Pt atom in a multiple atom defect site. DFT analysis herein was performed by Jang's group at Georgia Institute of Technology. We used the VASP [123,124] software package, where the electronic interactions and geometric optimization about the Pt atoms on graphene defects are performed using Perdew-Burke-Erzenhof (PBE) exchange-correlation functional within the Generalized Gradient Approximation (GGA) [125]. Atomic interaction energies between atomic species are obtained using a dispersive forces correction method by Grimme [126], and the core and valence electrons are handled by the Projector Augmented Wave (PAW) method [127]. The plane-wave energy cutoff of 450 eV was adopted, and the Brillouin zone was sampled with 2×2×1 Monkhorst-Pack *k*-point mesh with spin polarization. Computational models as shown at Fig 1(a) and 1(b), where the dimension of graphene is selected to have 12.30 Å × 12.30 Å wide to accommodate the defect and Pt clusters.

Various types of defect can be introduced on the graphene during growth or processing [128], affecting electronic or mechanical properties of the graphene. In this computational study, we use a double vacancy model as an exemplary multiple atomic defect without dangling carbon atom. The model schematic is given at Figure 5-a, showing two pentagons in symmetric mirrored positions due to structural reconstruction. Pt atom on defect center (Pt_D) and introduced cluster models are optimized in structures that are presented at Figure 5-b. For a single Pt atom binding, model Pt_0 at Figure 5-b, a Pt atom occupies the central position of defect forming strong bonds with four carbon atoms, where the bond length is measured around ~ 1.96

Å. Pt-C length between C of defect and Pt of Pt clusters is also ranged between 1.96 Å and 2.07 Å, which is in a good agreement with experimental observation stated earlier. However, it is found that the number of Pt coordination decreases dramatically (an order of magnitude lower) as the size of Pt cluster increases. Our calculations for Pt adatom interaction with graphene is well supported by literature reports for other metal adatoms (e.g. Au or Ni) [129,130]. Diffusion of metal adatoms was reported be two orders of magnitude lower, when metal adatoms is trapped between two defect-free graphene sheets compared to the energy required to liberate an adatom trapped within a graphene defect. Pristine graphene with limited amount of defect has low diffusion energy barrier, where atoms off Pt nanoparticles can diffuse freely [130–132]. This better explains the increase of Pt ECSA for GR3/Pt/GR sample with initial 5K ADT cycles, before a critical threshold of defects-concentration was reached where Pt adatoms became more prone to get trapped within defect sites.

In the same context, our DFT analysis implies that Pt clustering or agglomeration at a defect site of a graphene layer of multi-thick graphene is less favorable. Figure 5-c shows the highest energy variation of 4.76 eV from the model Pt_0 of Figure 5-b. It is found that all of active atoms on the defect are strongly interacting with the single Pt atom. As the Pt clusters are introduced, the reaction energy difference linearly decreases up to Pt_3 from 0.67 eV, 0.57 eV, and 0.47 eV for the Pt_1, Pt_2, and Pt_3, respectively. Pt atoms trapped at a top of a graphene defect is prone to diffuse when another Pt atom reaches defect center from the bottom side of the defect (Figure 5-b). Hence, top Pt atom diffuse between graphene layer till reach another defect site, while the bottom Pt atom hops towards the upper side of the

graphene defect. Similar observation was shown for other metals adatoms to have less energy barrier to migrate vertically from bottom to top site of a defect than lateral diffusion off the defect[130]. In addition, our DFT analysis showed that Pt-atoms clustering at the bottom side of the defect leads to rearrangement of atomic configuration at the defect that shift the Pt atom (Pt_D) to an off-center position in between graphene layers. This gives an explanation about the expected facilitated Pt migration through the graphene layers. Figure 5-c depicts the reaction energy variation (i.e. energy barrier to liberate Pt atoms from defect site) for the Pt migration from the defect site to an adjacent position where the Pt atom binds with *sp*2 carbon atoms of the graphene layers.

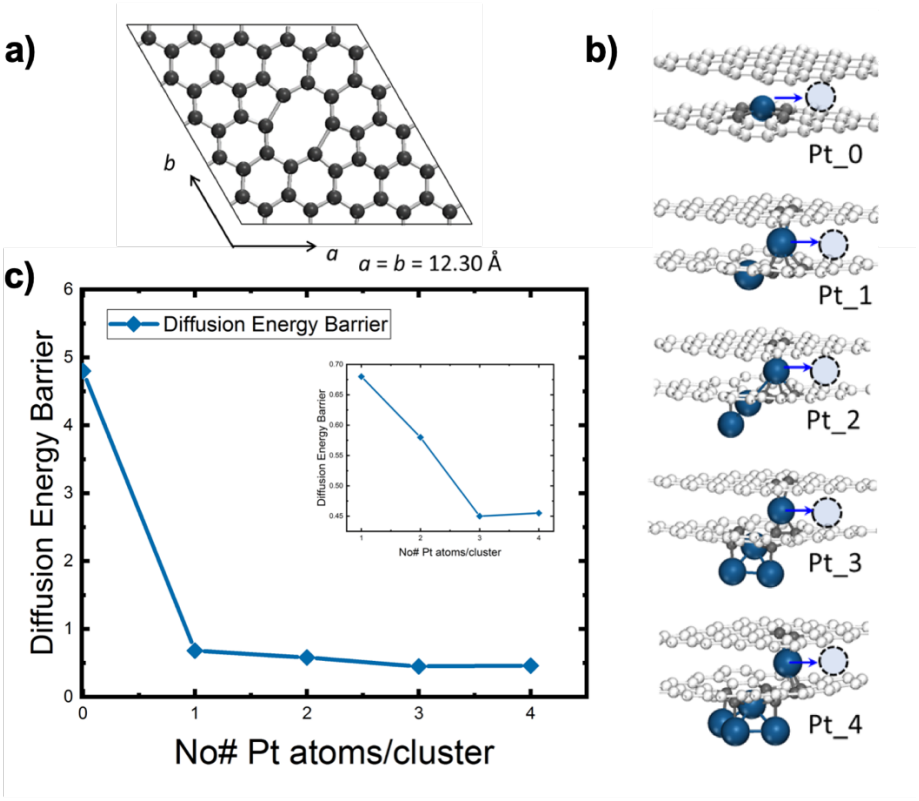

Figure 25(a) shows the computational model of graphene defect. Multi-atomic defect is introduced on the graphene. (b) shows Pt clusters formed at the bottom of graphene layers. Pt_n (n = 0~4) indicates the number Pt atoms of each cluster. Dotted circle indicates the position after the Pt migration. Single Pt atom at Pt_0 locates in the middle of defect site forming strong Pt-C covalent bonds, and it is found to deviate from the central binding position by introducing the Pt clusters. (c) plots the reaction energy change for the migration of a Pt atom. The energy change becomes saturated since Pt_4.

5.3.2.5 ORR Electrocatalytic activity

Fulfilling two desired objectives to synthesize commercially competitive catalyst are stability and activity enhancement. GR/Pt/GR sandwich structure showed better stability and prolonged lifetime compared to state-of-the-art commercial Pt/carbon catalyst, as discussed earlier. ORR catalytic activity was tested in an oxygen saturated 0.1M $HClO_4$ with a negative going sweep (0.9: -0.1 V) at 10 mV/s rate. Samples with 5-layers thick graphene (i.e. GR5/Pt/GR) showed no ORR activity. This finding agrees with blockage of Pt active sites by graphene before defects presence. On the other hand, samples with single layer graphene (i.e. GR1/Pt/GR) showed clear activity towards ORR, which is in agreement of other literature reports confirming ORR activity for similar case scenario [30]. Astonishingly, GR3/Pt/GR sandwich structure with 3-layers thick graphene showed catalytic activity towards ORR. Raman analysis and ECSA measurements discussed earlier showed that GR had very high quality with a limited defect's density (Figure 24-b shows a minute D-peak intensity) before ADT. This observation confirms that ORR exclusively occurred on top of graphene, with no possibility for ORR intermediates to penetrate through graphene to occur between top and bottom graphene sheets.

Mass activity of sandwich structure outperformed its Pt/carbon commercial catalyst counterpart. As a universal metric to evaluate ORR mass activity, current density measured at 0.9 V vs RHE reference electrode (0.7 V vs Ag/AgCl reference electrode used in the presented thesis) showed 7-folds enhancement for GR3/Pt/GR sandwich structure over state-of-the-art commercial Pt/carbon catalyst, as shown in Figure 26. Origin of activity enhancement is believed to be due to intimate contact between Pt and graphene, where Pt-Pt is affected by templated growth on graphene

[12,30,39]. TEM analysis showed shrinkage of Pt-Pt bond distance, observed earlier for Pt grown on graphene when compressive strain was induced on Pt adatoms [12,39]. Pt metal is at the strong Pt-Oxygen interaction side of the volcano plot [23–25,47]. To enhance ORR activity, oxygen bonding to Pt should be weakened to allow for facile desorption of ORR reaction intermediates. Compressive strain affects metal adatoms d-band center position, pushing d-band center down (further away) from the fermi level [42,107,133]. Thus, anti-bonding states of metal adatoms are more filled where interaction with reaction intermediates (i.e. oxygen) becomes weaker. Moreover, defective graphene showed higher ORR electrocatalytic activity at edge-plane and defects sites due to dangling bonds. Therefore, enrichment of graphene defect density, enhanced the overall ORR activity of GR/Pt/GR sandwich structure [134,135]. In addition, the synthesized mixed single atomically dispersed and small nanoparticles promoted higher precious metal catalyst (i.e. Pt) utilization with larger surface area exposed per mass loading.

Combining the demonstrated superior catalytic activity and durability, GR/Pt/GR sandwich structure opens the door to design smart hybrid platforms that are well protected, highly stable, accessible and transferrable, not only for catalysis applications but electronics, environmental, biomedical and sensing applications.

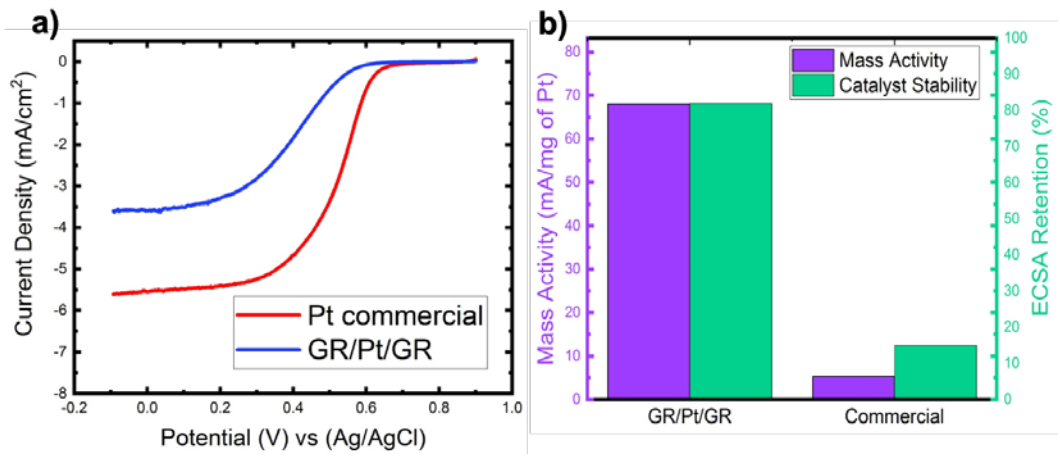

Figure 26 ORR Activity of GR/Pt/GR (red) and state of the art Pt-XC/72R commercial catalysts: (a) Current density depicted through linear sweep voltammetry of GR3/Pt/GR with an order of magnitude lower mass loading compared to commercial Pt catalyst. (b) Bar-chart comparing mass activity (purple) and catalyst lifetime stability represented by ECSA survived after 15K ADT cycles.

Conclusion

Pt-wrapped catalyst was successively protected by two graphene sheets. GR/Pt/GR Sandwich structure showed significant enhancement of catalyst stability. Graphene cap worked as a shield preventing the loss of Pt atoms. Optimal thickness of graphene cap was found to be 3-layers thick, where GR3/Pt behaved as a hybrid catalyst to catalyze ORR. At the same time, 3-layers thick graphene showed remarkable stability, surviving 640% more Pt ECSA compared to state-of-the-art commercial Pt/carbon catalyst. Pt ORR activity enhancement was attributed to graphene/Pt intimacy resulting in

compressive strain. In addition to enhance Pt utilization through mixed nanoparticle and highly stable single Pt-atoms trapped within graphene defects. Degradation mechanism of catalyst stability is thought to be through introduction of defects within graphene's structure, where Pt atoms migrates towards the surface through, before leaching out in the electrolyte. The demonstrated GR/Pt/GR sandwich structure provides a versatile material platform that can be tailored not only for electrocatalytic application, but others including environmental, biomedical and sensing applications.

5.4 Synthesis of highly active and commercially competitive ORR Catalyst

Catalyst development is key factor in success of commercializing PEMFC and other electrocatalytic devices. State-of-the-art material for ORR, which is the major problem in reducing PEMFC cost is Pt and its group-metals. During the past chapters we have been demonstrating the effect of the support on catalytic performance at both activity and stability aspects. However, major influence comes from the catalyst itself; specifically, morphology, and surface properties. Research efforts demonstrated intimate relation of Pt-based materials activity and stability with morphology. Higher catalytic activity was reported by Mufan Li and coworkers for developing ultra-jagged Pt nanowires.[14] Ultra-jagged nanowires showed an order of magnitude enhancement in mass activity compared to spherically-shaped state-of-the-art Pt/carbon commercial catalyst. In addition, Pt nanowires showed higher stability with a loss of 7% of ECSA, compared to 30% loss for state-of-the-art Pt/carbon commercial catalyst. Other reports focusing on dendritic nano-architectures showed ~6 folds enhancement of mass activity compared to state-of-the-art Pt/carbon commercial catalyst. Xia's group and coworkers demonstrated enhancement of ORR activity by introducing Pt-Pd nano-cages where Pd metal actd as a framework on which atomic scale layers of Pt were deposited.[112]

However, synthesis protocols by Xia et. al and others showed significant enhancement of ORR activity, yet, complicated synthesis techniques were used. Synthesis protocols involved heating beyond boiling point of water (>100 °C), several steps to produce final product, or materials etching of templates and sacrificial layers which entailed loss of precious metals (e.g. Pd). Hence, facile and cost-effective production of catalysts is still a challenge. Presented herein, a one-pot synthesis of

highly branched Pt-nanoflower catalyst with a simple and straight forward chemistry protocol. Several factors have been studied to enhance catalyst activity while maintaining an easy one-step nanoparticle reduction step. In the following sections, details about synthesis efforts and associated structural and electrocatalytic activity results will be discussed in detail.

5.4.1 Experimental Section

5.4.1.1 Controlled synthesis of Pt-nanoflowers

Carbon black XC/72R (11.4 mg) was sonicated in 17 mL DI-water for 3 hours. Afterwards, 1 mL of 38 mM Pt precursor ($PtCl_3.6H_2O$) was added to the carbon suspension with the addition of 1 mL of 38 mM formic acid and 1 mL of 76 mM sodium citrate. The effect of solution temperature, reduction agent chemistry, medium hydrophilicity, catalyst composition and catalyst-support on ORR were investigated. Further details about the synthesis and testing procedure will be discussed in detail at the relevant sections for each effect in the presented thesis.

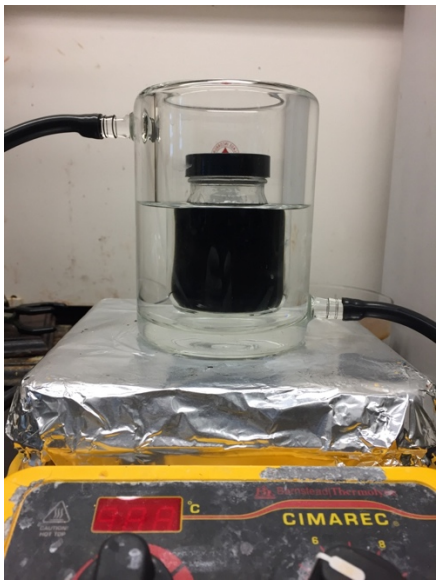

Figure 27: Jacketed beaker temperature-controlled water bath for catalyst synthesis

5.4.2 Results

5.4.2.1 Effect of Temperature

Synthesis of Pt-nanoflower under room temperature conditions showed huge discrepancies in ORR electrocatalytic activity. An important factor to consider is the fluctuation of room temperature during summer/winter time when air condition is alternating from cold to hot, hence, slight change in temperature (i.e. $\pm$ 2 °C) can affect the reaction time (i.e. time needed for complete reduction of Pt precursor). Therefore, the reaction solution was mixed under controlled temperature using a jacketed beaker at 15, 20, 25 and 30 ^{o}C. Reaction time was monitored and depicted in Figure 28 with a nearly linear, inversely proportional relationship. For reactions occurred at 15, 20, 25 and 30 ^{o}C the time observed to fully reduce the same amount of Pt precursor was 42,

30, 17 and 12 hours, respectively. To further explore the reaction kinetics and effect of temperature, catalysts synthesized at significantly lower temperature (~4 °C) showed no reduction of Pt precursor up to 168 hours, which indicated intimate correlation of reaction kinetics and temperatures. After reduction occurred, Pt nanoparticles were washed successively by DI-water during centrifugation for 3 times. Catalysts were extracted and dried under vacuum before further electrochemical testing. Thermogravimetric analysis showed that the synthesized nanoparticles had an effective Pt loading of 38% and 62% carbon black.

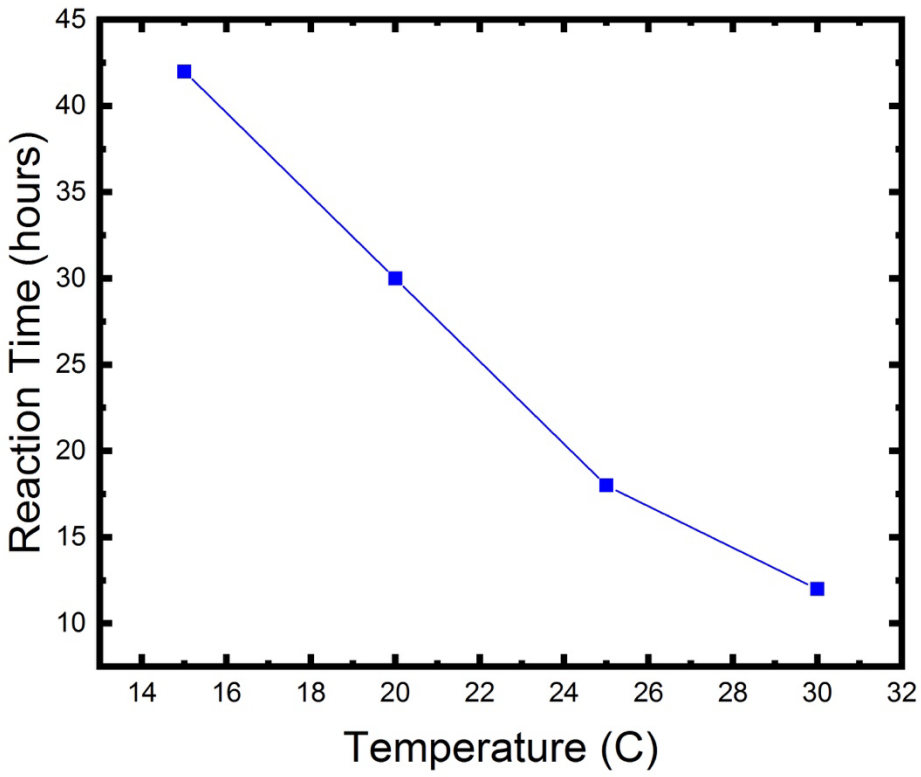

Figure 28: Linear relationship showing the effect of reaction temperature on reaction time needed to fully reduce Pt-nanoflower particles.

Electrochemical analysis was performed in 3-electrode setup using 0.1M

$HClO_4$ as an electrolyte, graphite rod as a counter electrode and Ag/AgCl as a reference electrode. Catalyst ink was prepared by addition of 1.00 mg of Pt-nanoflower carbon-supported catalyst to 0.75 ml of DI-water, 0.25 ml of IPA and 20 μl of Nafion solution (5% wt. dissolved in ethanol). Catalyst ink was sonicated for four times, each of 30 minutes. Water in the ultrasonication bath was replaced between each sonication cycle (i.e. 30 min) to avoid excessive temperature increase which could decompose the Nafion compound. 10 μl of the catalyst ink was drop-coated on mirror polished 5 mm glassy carbon electrode. Catalyst ink was dried under room temperature atmosphere for few hours before testing. Similar composition of ink is used throughout the study, with an exception of changing the catalyst compound, as denoted later. ORR activity was probed in an oxygen saturated electrolyte (i.e. 30 min bubbling before testing) at 1600 rpm, using linear sweep voltammetry (LSV) 0.9:-0.1V with a scan rate of 10 mV/s. examining the half-wave potential of LSV curves for Pt-nanoflower catalysts synthesized at 15, 20, 25 and 30 °C showed best activity for catalyst synthesized at 25 °C, followed by 20, 30 and 15 °C, as the lowest as shown in Figure-29.

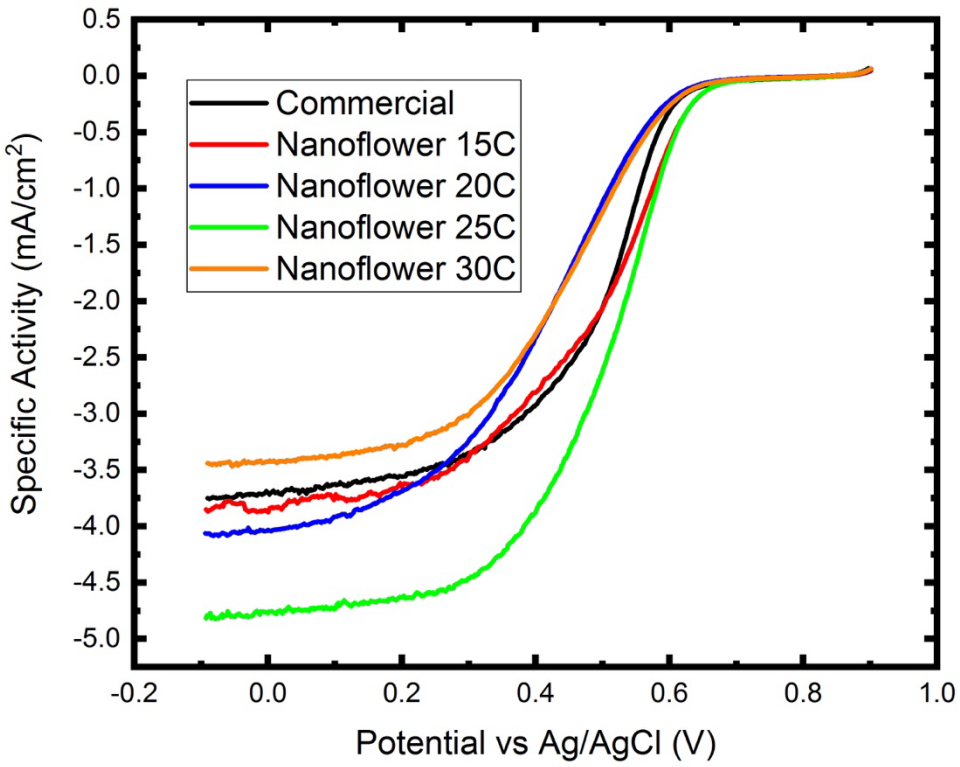

Figure 29: LSV scans for Pt-nanoflower catalyst synthesized at 15, 20, 25 and 30 C, compared to commercial Pt/carbon HISPEC4000 catalyst by JM company

TEM analysis showed that Pt nanoparticles grown at temperature of 25 °C possesses shape of nanorods or multipods (i.e. nanorod interconnects) which are denoted throughout the study herein as nanoflower. Anisotropic nature of the nanoparticles showed enhancement of electrocatalytic activity towards ORR compared to spherical particles of Pt/carbon commercial catalyst. In addition, Pt-nanoflower periphery possess high density of high-index crystallographic family planes. High-index planes showed step terrace within surface atoms where surface atoms suffer from compressive strain to accommodate for the step terrace. Compressive strain enhances

ORR activity of Pt based catalyst by altering the d-band center position, shifting downward away from the fermi level, as described earlier in the background section.

5.4.2.2 Effect of alloying

Cheaper metals (Ni, Co and Fe) precursors were added to Pt-nanoflower synthesis mixture, as discussed earlier. Pt/M (i.e. M = metal) alloy was synthesized with a 3/1 molar ratio at different reaction temperature (i.e. 20 and 25 ^{o}C). In addition, different molar ratios were investigated at a fixed temperature of 25 ^{o}C. Two sample sets were prepared following the formula $Pt_{1-X}M_X$ (i.e. M = Co or Ni). Pt-Ni alloy showed interesting activity due to synergistic effect and electron donation between Ni and Pt. X-ray diffraction analysis of the synthesized powder was performed, as shown in Figure 30. XRD spectra analysis showed preservation of peak's relative intensities for each sample set. In addition, no observation of Ni metal peak was observed, however, Pt peak shifted systematically towards higher 2-theta values. Shifting peak position to higher 2-theta values is an indicative of shrinkage of crystal's lattice parameter, according to Bragg's law. The aforementioned observation hypothetically suggesting alloying of Ni within Pt FCC lattice. Ni atomic radius is shorter than Pt's. Therefore, doping Ni substitutional atoms with Pt yields a contraction of Pt FCC lattice parameter.

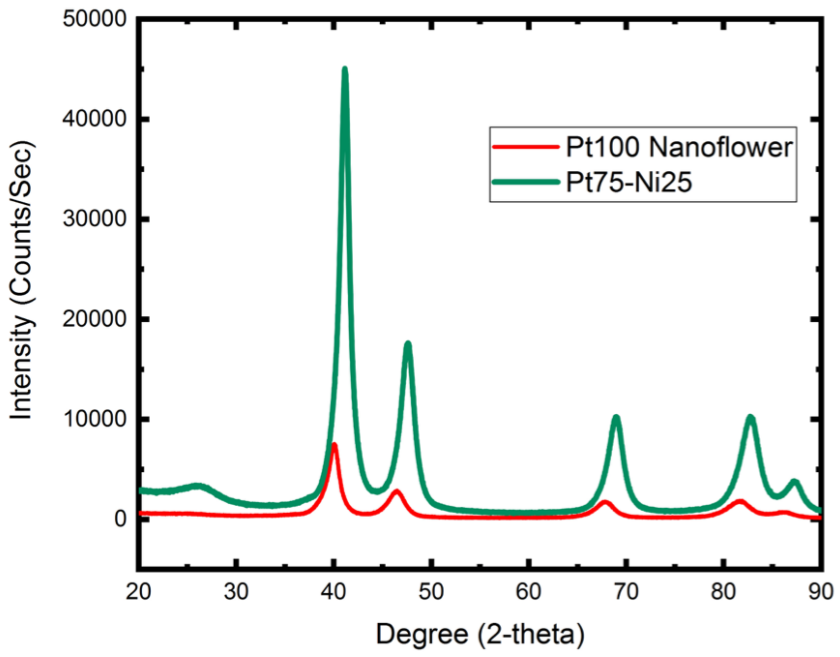

Figure 30: XRD of Pt3Ni1 alloy and Pt-nanoflower spectra

To confirm the alloy formation, XPS analysis was performed Figure-31. Surprisingly, XPS high resolution scans showed no detection of Ni 2P or Co photoemissions, however, pronounced Pt 4f signal was observed.

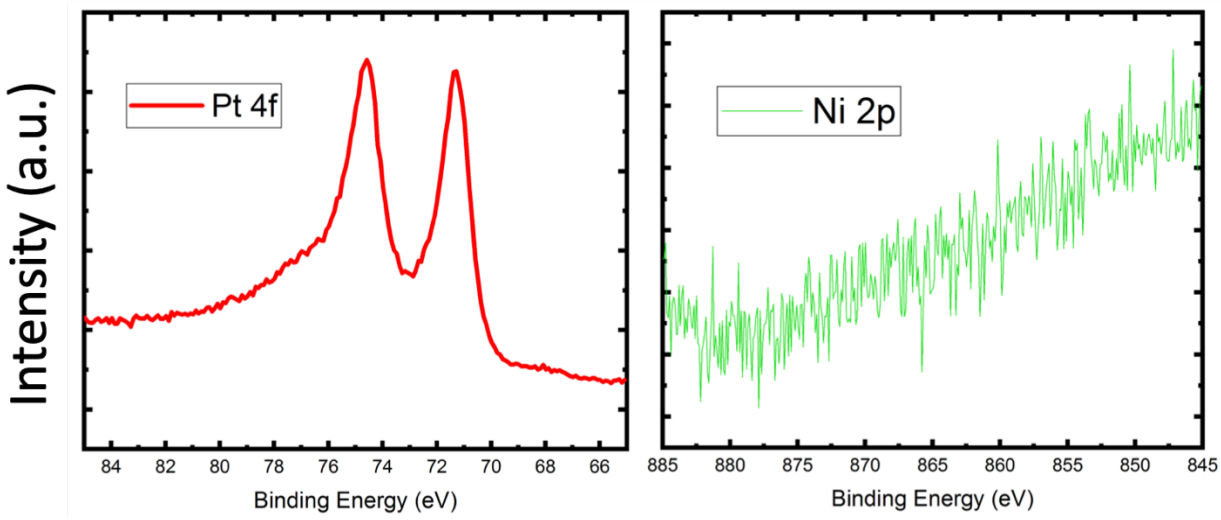

Figure 31: XPS high resolution spectra of Pt 4f and Ni 2p of Pt3Ni1 catalyst

ECSA was tracked by CV in nitrogen saturated 0.1M HClO4 solution at 50 mV/Sec. Integrating the peak area of H_{upd} of different $Pt_{1-X}Ni_X$ showed reduction of peak area with alloying, indicating less active surface area possessed by the catalyst. Literature reports of Ni nanoparticles and/or Pt-alloyed Ni nanoparticles showed successful synthesis at elevated temperatures (100-150 °C), however, complete reduction with the presented chemistry herein seems to be thermodynamically or kinetically challenging at the given temperature (20-25 °C). Further investigation of the supernatant of centrifugation after Pt-Ni reduction, no color for green or red solution was observed (for Ni or Co precursors, respectively). As per the XRD data and owing to sensitively limit of XPS analysis (detection > 2% weight and thinner than 4 nm), there could be slight amount of Ni or Co doped within Pt crystal, large enough to change Pt-lattice parameter, but not significant to be detected by XPS. Yet, further

investigations with more sensitive elemental analysis technique (i.e. Inductive Coupled Plasma Mass Spectrometry (ICP-MS)) to confirm the formation of an alloy is needed.

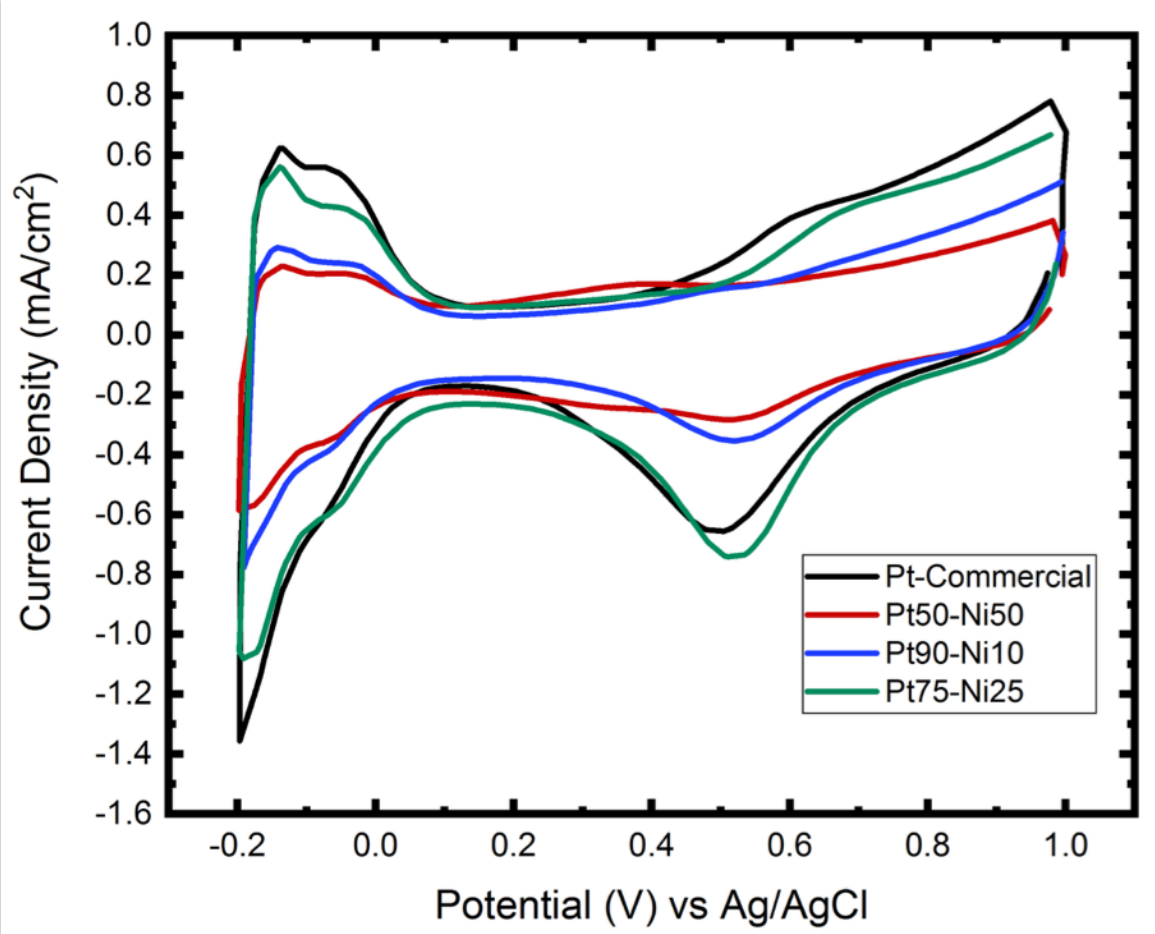

Figure 32: ECSA of Pt-Ni alloy nanoparticles in nitrogen-saturated 0.1M HClO4

5.4.2.3 Effect of reaction chemistry

The reducing agent is thoughtful to influence the morphology of Pt-nanoparticles significantly, which is believed to alter its ORR performance in return. Different ratios of reducing agents (i.e. formic acid) have been used to synthesize Pt-nanoparticles, as

shown in the table below, however, similar ratio of Pt precursor and sodium citrate have been remained fixed, as given for Pt-nanoflower in earlier section. Results showed complete reduction of Pt-nanoparticles for all ratios of formic acid. ORR activity probed using LSV, as described earlier showed reduction of ORR activity with half-wave potential shifting more negative (i.e. increase of overpotential for ORR) with increasing of formic acid ration from 100% to 120%. Further increase of formic acid ratio to 140% showed intermediate performance, as shown in Figure 33 below. Increasing formic acid, enhanced the kinetics of the reaction to reduce Pt nanoparticles, which might provide more time for Pt particles' growth. Optimal ORR activity was observed for 100% formic acid ratio.

Table 2: Pt-nanoparticles solution chemistry ingredients

Sample Label	Pt conc%	Sodium Citrate conc%	Formic Acid (i.e. R) conc%	Pt loading	Carbon support
Pt100_R100	100	100	**100**	40%	60%
Pt100_R120	100	100	**120**	40%	60%
Pt100_R140	100	100	**140**	40%	60%

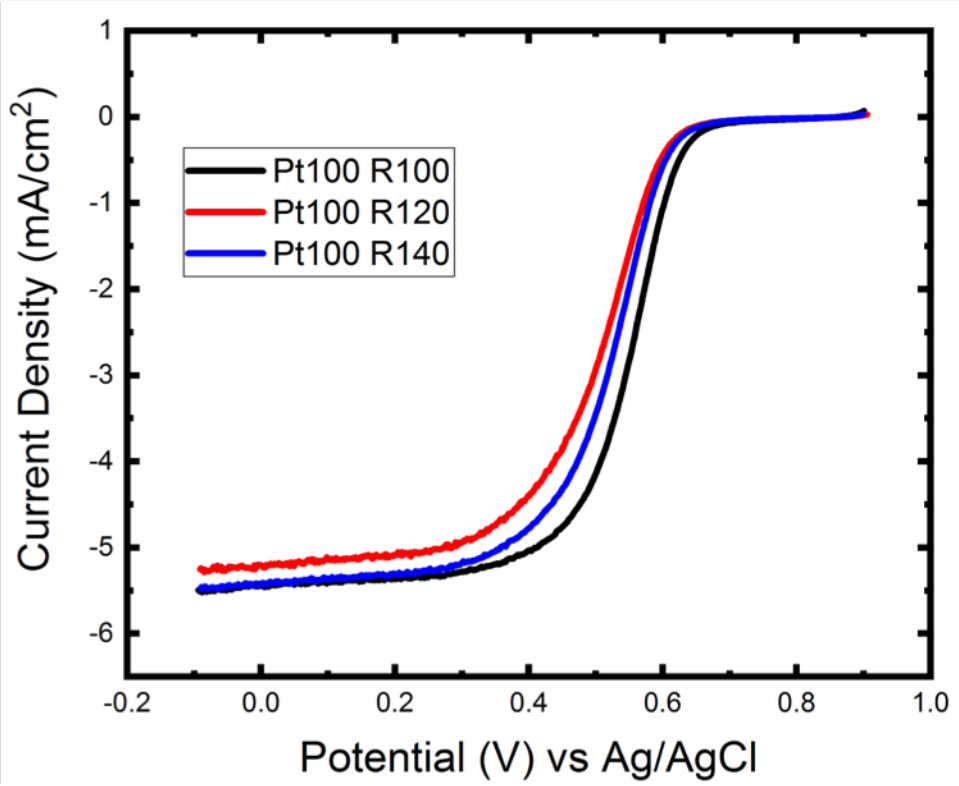

Figure 33: LSV of Pt nanoparticles synthesized with different volumetric ratio of reducing agent (i.e. formic acid)

a) Effect of carbon support (GR and HSAC)

Graphene demonstrated interesting platform to grow Pt catalyst architectures. Pt adatoms grown on graphene experienced a compressive strain enhanced ORR activity. In addition, catalyst lifetime was enhanced dramatically due to interfacial bonding between carbon of graphene and Pt adatoms, forming a covalently bonded Pt=C. Therefore, efforts presented in this section to develop commercially competitive Pt nano catalysts were expanded to include different carbon supports including graphene.

To maximize the loading of graphene per geometric area, 3D graphene architecture showed a huge promise in this regard. Graphene oxide (GO) sheets were synthesized following a modified hammers method.[69] Raman analysis showed typical spectrum of GO with pronounced D and G peaks, as shown in Figure 34.

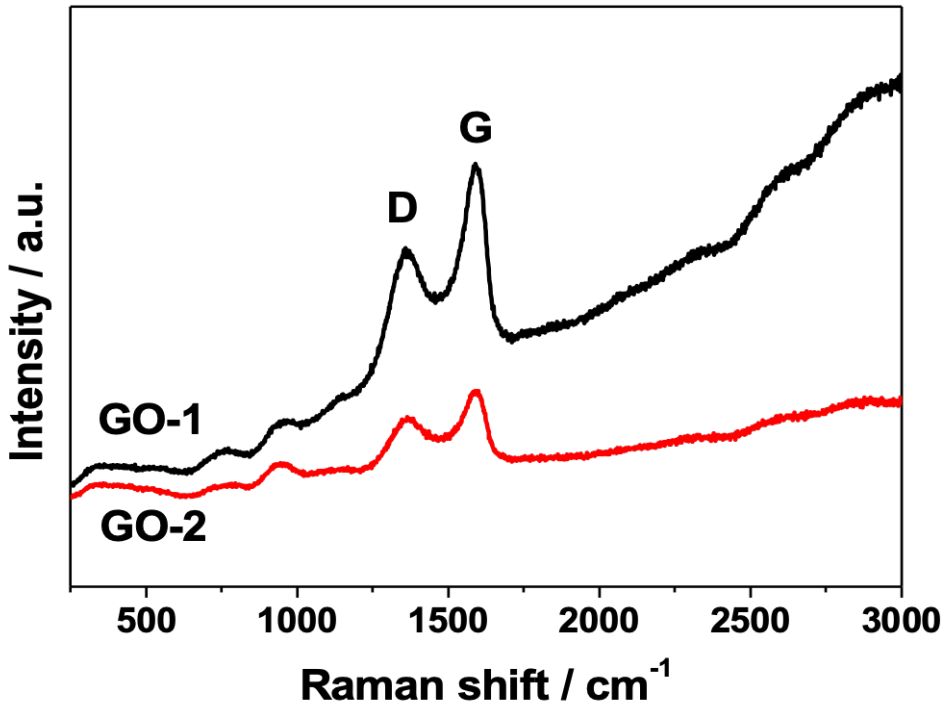

Figure 34: Raman spectra of graphene oxide samples synthesized following a modified hammer's method

Afterwards, 150 mg GO was dispersed in 15 mL water to form a concentrated GO suspension, followed by mixing with 1 mL formaldehyde solution (37% wt) and 0.35 g melamine. The mixture was then transferred into an autoclave and hydrothermally treated at 180 °C for 12 h. The obtained composite hydrogel was dried

at 120 °C for 24 h in an oven. The dry aerogel was subsequently calcined at 750 °C for 5 h in Ar atmosphere to obtain the final N-doped graphene flakes. Results showed a synthesis mass yield of ~70%. XPS analysis of N 1s and C 1s photoemissions showed pronounced nitrogen content with peak shift towards lower binding energies, where nitrogen doping into graphene structure is thoughtful. Nitrogen has higher electronegativity compared to carbon. Shifting of N 1s photoemissions to higher binding energies is an indication of electrons being donated to nitrogen, where the only possible source is carbon atoms of graphene.

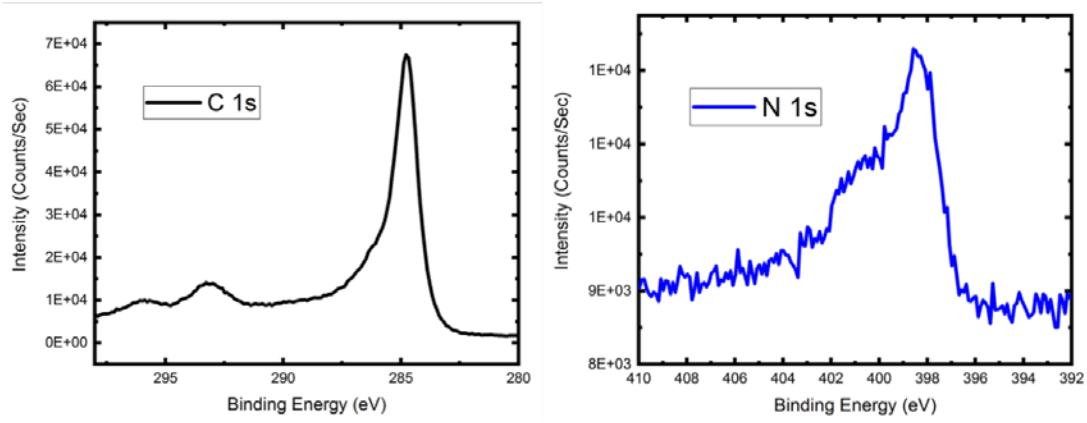

Figure 35: XPS spectra of carbon 1s and nitrogen 1s of N-doped graphene 3D network

Additional effort was spent to synthesize porous 3D N-doped graphene network. Graphene was grown by CVD on Cu foam. Fine tune of CH_4, H_2 and Ar flow rates enabled successful synthesis of 3 to multi-layer graphene on Cu foam. Thick graphene foam (~1.4 mm) was fully coated by graphene from surface to bottom struts, which

was confirmed by Raman analysis which showed very similar spectra of top foam side and bottom sides, as shown in Figure-36.

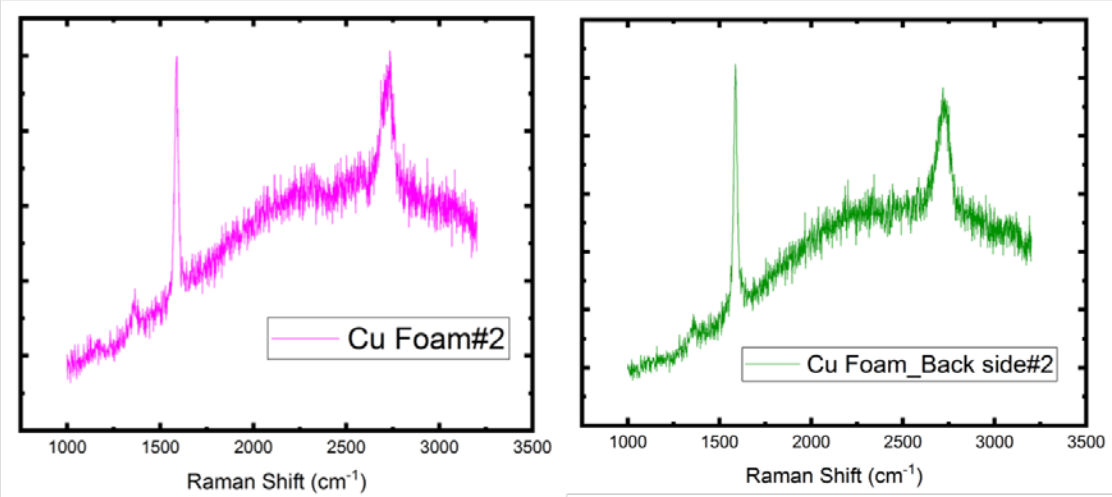

Figure 36: Raman analysis of top and bottom sides of Cu foam after Graphene CVD growth

Nitrogen doping within graphene 3D architecture can be achieved by either post annealing in nitrogen rich atmosphere or during CVD. NH_3 gas was used for post annealing of graphene on Cu foam at 700 °C. Raman and XPS analyses showed successful doping of nitrogen, however, with limited percentage. Nitrogen defects density is critical to preserve metal adatom morphology and activity. Too rich nitrogen doping can enable enormous amount of nucleation spots for Pt adatom growth, where the critical distance for Pt to Pt attraction is short enough to activate adatoms diffusion. Hence, active surface area is lost due to agglomeration. On the other hand, if nitrogen content is low, less active material will be bonded to graphene structure. Hence, enormous graphene is needed to achieve a considerable power output for a commercial application. Therefore, one setup was built to synthesis N-doped graphene by CVD

method. A bubbler with pyridine as a nitrogen source was added to the CVD system Ar-gas line. Fine tuning of Ar gas flow rate enabled addition of pyridine vapor to the CVD chemistry. XPS and Raman analyses showed successful doping of nitrogen with an average of 8% weight.

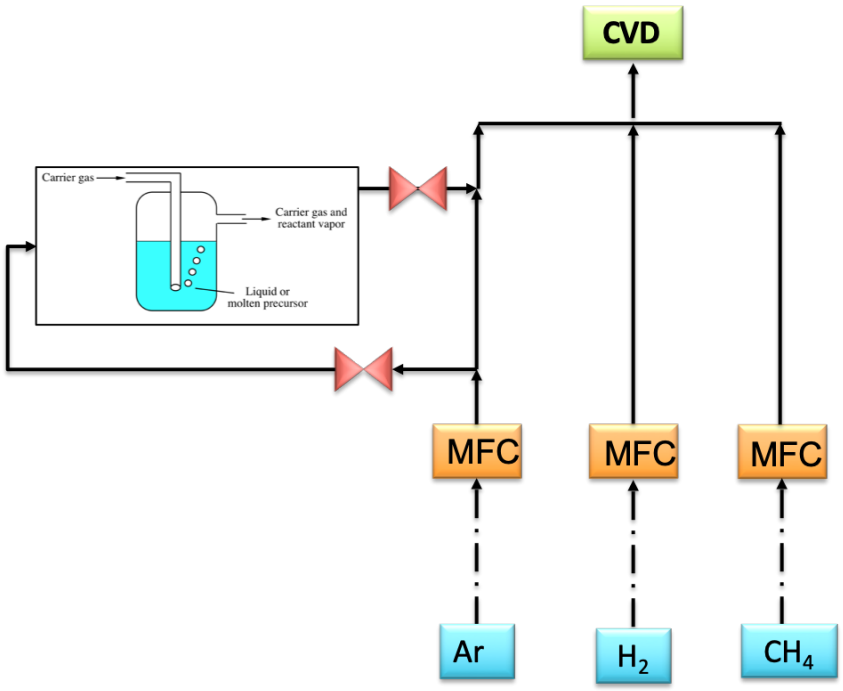

Figure 37: Schematic of CVD system with the addition of Pyridine bubbler to enable N-doped graphene synthesis

Pt-nanoflowers reported earlier were synthesized on N-doped graphene (N-GR) 3D networks, replacing commercial carbon black (Vulcan). Synthesis of Pt-nanoflower on N-GR was difficult, as synthesis chemistry is fully aqueous, however, N-GR is mostly hydrophobic. Tip sonicator was used to apply continuous pulses during synthesis of Pt-nanoflower, which limited the restacking of graphene, however, did not achieve uniform dispersion of N-GR in the solution. ORR was tested using RDE setup,

where Pt/N-GR ink was drop coated on the ink on glassy carbon electrode and left to dry for few hours. Visual observation showed non uniform coating of the ink on glass carbon disk. Graphene network was composed of large graphene sheets, where higher tendency to agglomeration was generated due to electrostatic attraction between graphene sheets. Ink solution was modified by alternating the ratio of IPA to DI-water to increase the solution hydrophobicity, where graphene dispersion is enhanced, and agglomeration is suppressed on the other hand. Visual observation showed slight enhancement of ink uniformity. To accelerate the drying of the ink and limit the restacking of graphene, a heating lamp was used to evaporate the IPA solution out of the ink after drop coating. Results showed slight enhancement, however, ink deposited still shown in islands, rather than a fully-wetted film covering the glassy carbon electrode, as shown in Figure 38. Nevertheless, ORR activity showed slightly lower activity of Pt-nanoflower synthesized using N-GR compared to similar nanoparticles synthesized on carbon black.

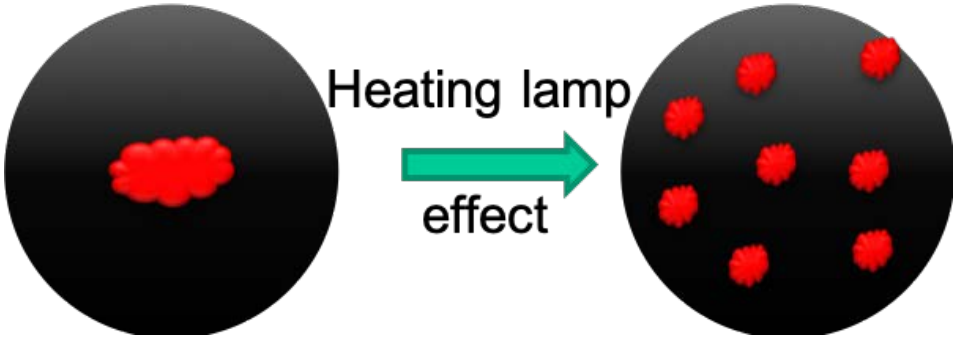

Figure 38: Schematic showing effect of heating lamp on catalyst ink (red) deposited on glassy carbon electrode (black) to avoid restacking and agglomeration of N-doped graphene

5.4.2.4 Effect of Reaction medium

Graphene, as a hydrophobic material is supposed to have better dispersion in organic mediums. Therefore, to avoid graphene agglomeration or restacking during Pt-nanoflower synthesis, reaction medium was changed from aqueous to organic using dimethyl-formamide (DMF) and dimethyl-sulfoxide (DMS) as widely used solvent for dispersion of carbon nanostructured materials (e.g. graphene and carbon nanotubes), and yet miscible with water.[136,137] Similar precursor and experimental setup of Pt-nanoflower reported earlier was followed while the solution is DFM or DMS instead of DI-water. No change of solution-color was observed for either reactions taking place in DMF or DMS over 72 hours. Hence, a mixture of DI-water and DMF or DMF was used to mitigate for difference in reaction mediums, as shown in table 3 below. No observation of solution-color change as an indication of no reduction of Pt precursor was observed for any sample, except for minor addition of organic solvent. A ten percent volume of DMF dissolved in DI-water (i.e. DMF-10), where reaction time was

recorded to occur between 16-18 hours. Similar result was observed for DMS-10, however, reduction time was recorded to be ~54 hours. The aforementioned observations suggest that synthesis of Pt-nanoflower as per the recipe given herein is very sensitive to reaction medium and type of the solvents used.

Table 3: Pt-nanoflower reaction precursors in dimethyl-formamide solution

Label	Pt (mL)	Sodium Citrate (mL)	Formic Acid (mL)	N-GR (mg)	DMF (mL)	DI-water (mL)	Reaction time (hours)
DMF-100	1	1	1	11.4	15	0	> 72
DMF-70	1	1	1	11.4	10	5	> 72
DMF-40	1	1	1	11.4	6.5	8.5	~52
DMF-10	1	1	1	11.4	1.5	13.5	16-18

Table 4: Pt-nanoflower reaction precursors in dimethyl-sulfoxide solution

Label	Pt (mL)	Sodium Citrate (mL)	Formic Acid (mL)	N-GR (mg)	DMS (mL)	DI-water (mL)	Reaction time (hours)
DMS-100	1	1	1	11.4	15	0	> 72
DMS-70	1	1	1	11.4	10	5	> 72

DMS-40	1	1	1	11.4	6.5	8.5	> 72
DMS-10	1	1	1	11.4	1.5	13.5	~54

N-doped graphene was used as a support to grow Pt-based catalyst following the recipe of Pt-nanoflower in 10% DMF solution. Oxygen reduction reaction is a function, as a typical electrocatalyst, in active surface area. The active surface area is determined by accessibility of reaction intermediates through electrolyte to the catalyst surface. Therefore, dispersion of catalyst material is a crucial factor to convert catalysts' intrinsic activity into a tangible performance. Pt catalyst synthesized on N-doped graphene, however, overcome the poor dispersion during synthesis procedure, suffered from restacking when drop coating the ink on glassy carbon or Nafion membrane for RDE and MEA analysis, respectively. Catalyst ink was modified by increasing the organic solvent ratios from 1:3 to 1:1 IPA:DI-water. Ink dispersion on glassy carbon electrode was further enhanced accordingly. Nevertheless, ORR activity probed by LSV showed drastically poor activity for catalyst prepared in mixed DMF/Di-water solution compared to catalyst prepared in pure aqueous solution, as shown in Figure-39.

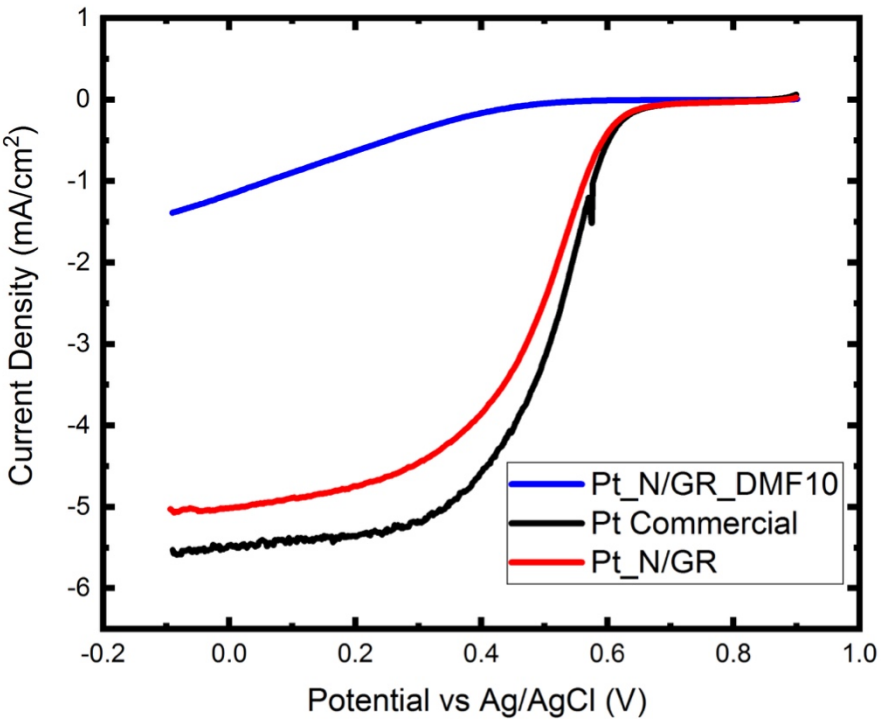

Figure 39: ORR activity of Pt-catalyst synthesized on N-doped graphene substrate in aqueous and mixed organic-aqueous solutions compared to state-of-the-art commercial Pt-carbon catalyst.

5.4.3 Discussion

5.4.3.1 Structural analysis

Structural analysis of Pt-nanoflower particles showed anisotropic particles morphology. This helps to provide strong anchoring of Pt particles to catalyst support. In addition, particles were surrounded by low-coordination atomic steps of high index planes (e.g. [310] & [020]). Low-coordination atoms of steps and kinks perturbs surface atoms order. Norskov et al. and others studied the relation between surface atomic-steps and strain induced on surface atoms.[138–141] DFT calculations modeled on perfect

Pt (111) surfaces with different densities of steps (i.e. distance between steps) showed an inversely proportion relation between strain sign and magnitude with distance between steps. As steps density increases, effective distance between two adjacent steps gets shorter Hence, more compressive strain is induced on terraces' surface atoms in between. In consequence, Pt atoms suffers from compressive strain to accommodate for perturbation. Compressive strain shifts Pt d-band center position away from the Fermi level, weakening the bonding of Pt with reaction intermediates (OH^-). Therefore, ORR activity is increased due to more availability of catalytic active sites. Synthesis temperature showed great influence not only on changing reaction time, but morphology, as well, as shown in Figure-40. Increasing synthesis temperature increased reaction kinetics, forced nanoparticles to shift from multi-branched morphology to nano-rods, which might happen due to facile nucleation of nanoparticles. On either case, it's widely common in literature that anisotropic nanoparticles showed higher electrocatalytic activity, however, multi branched structure gives higher activity due to larger surface area. XRD analysis of Pt-nanoflower showed major intense diffraction peaks at 39.8 °, 46.3 ° and 67.5 ° corresponding to (111), (200) and (220), respectively. Evaluating particles size using Scherrer's equation from FWHM of XRD peak, yield 4.3 nm avg size.

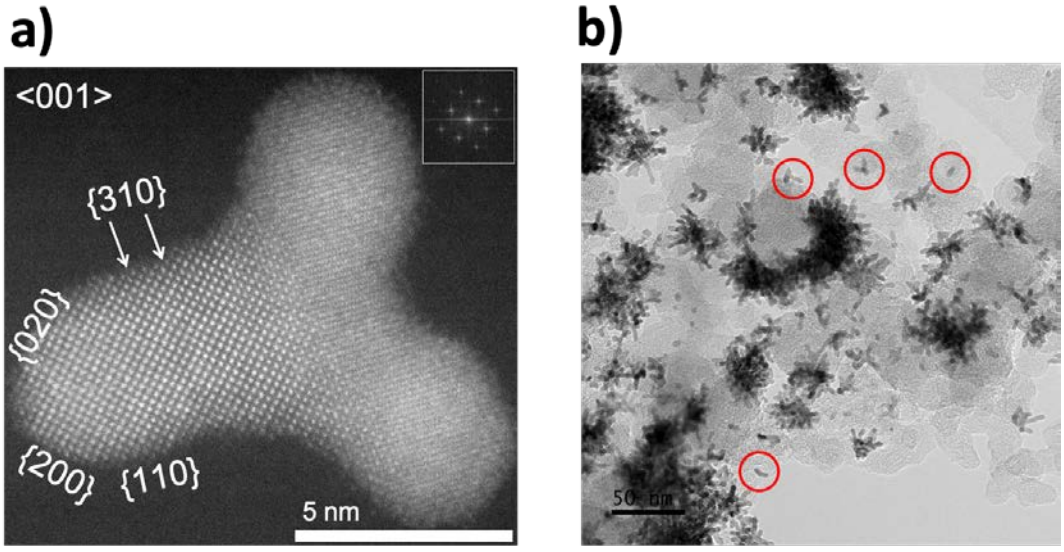

Figure 40: TEM images of Pt nanoparticles synthesized at different temperature. a) STEM image of Pt-nanoflower synthesized at 20-25 C showing series of high index planes at particles' surface {310} & {020}. b) TEM image of Pt-nanoflower particles showing nano-rods and multi-pods interconnects.

5.4.3.2 ORR Activity

ORR activity probed by LSV scans showed superior catalytic aptitude compared to state-of-the-art commercial Pt/carbon catalyst. However, many catalysts showed better laboratory testing advantage to Pt/carbon commercial. Yet, HISPEC4000 produced by JM company is the market dominant, regardless of its poor stability. Stability shortcoming originated from spherical morphology and easily corroded carbon support (i.e. Vulcan carbon-black). Our Pt-nanoflower has been tested in a full PEMFC setup. Testing of Membrane Electrode Assembly (MEA) was performed using Nafion-211 membrane, with Pt-nanoflower only applied as cathode

catalyst, while HISPEC4000 is the catalyst for anode side. Catalyst Ink was deposited through hot spray on the Nafion membrane. A net Pt catalyst loading of 0.1 and 0.05 mg/cm^2 was used for cathode and anode sides, respectively. Maximum operating current density obtained at 0.6 V was 1.40 and 1.05 A/cm^2 for Pt-nanoflower and Pt-carbon commercial catalysts, respectively, when used as cathode catalysts. Maximum power output was calculated to be 1.075 and 0.654 W/cm^2 for Pt-nanoflower and Pt-carbon commercial catalysts, respectively, when used as cathode catalysts.

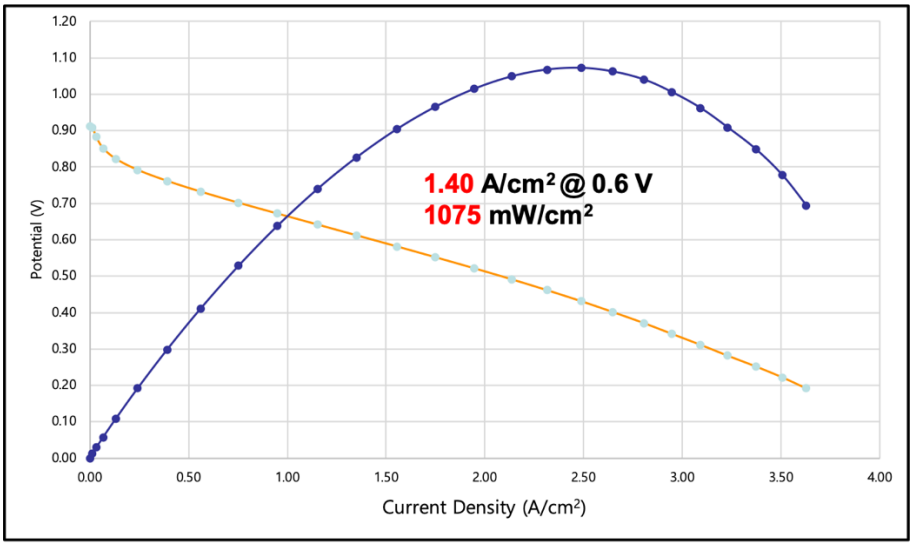

Figure 41: Pt-nanoflower MEA activity 0.1 mg/cm^2 as a cathode catalyst

Conclusion

Highly active Pt catalyst was synthesized using a simple one-pot temperature-controlled routine. Results showed that Pt morphology was influenced by reaction temperature, which consequently affected ORR activity, where higher temperature increased reduced ORR activity. Pt-nanoflower showed higher reactivity compared to commercial Pt-carbon due to possessing high density of low-coordination surface atoms. Low-coordination surface atoms of high-index family planes perturb surface short-range order causing compressive strain, which enhance ORR activity by shifting d-band center position away from the Fermi level. In addition, anisotropic and branched nature of Pt-nanoflower enhances ORR activity due to higher Pt utilization, with larger active surface area exposed.

5.5 Concluding Remarks

Hybrid graphene/Pt catalyst architectures showed interesting catalytic activity enhancement and significant improvement in catalyst lifetime under harsh PEMFC conditions. STEM analysis showed that Pt grown on graphene by electrochemical layer-by-layer deposition obtained (100) crystal orientation rather than more stable (111) direction. Graphene dictated Pt growth, providing a template for epitaxial adatom growth where Pt atoms sit at every-other bridge site between C=C bond. Furthermore, STEM analysis showed fully wetting of electrochemically grown Pt monolayers on graphene with sharp growth front, while ripening was avoided. XPS spectra for various Pt-deposition iterations showed systematic growth of Pt with each deposition iteration which indicated high control on Pt deposition at the atomic scale. In addition, full

graphene wetting with Pt adatoms was achieved at an ultra low-dimensional thickness of ~1 nm. DC-sputtered Pt ultra-small nanoparticles showed average size below 3 nm, where sputtering time increased particles density rather than particle's size, indicating less tendency towards agglomeration. STEM analysis showed that Pt adatoms sandwiched between two sets of graphene showed a halo of individual Pt atoms surrounding Pt nanoparticles circumference consistently.

EXAFS and TEM analysis confirmed the existence of induced compressive strain on Pt-Pt bond distance with approximately ~4%. Mechanical compressive strain induced by graphene altered the electronic configuration of Pt adatom. XPS analysis showed negative shift of Pt 4f orbitals to lower binding energy. This imply a down shift of the d-band center away from the Fermi level, as a consequence, ORR electrocatalytic activity was enhanced. Compressive strain caused a down shift of Pt d-band center, where reaction intermediates bonding to Pt surface became weaker. Hence, ORR products desorption was facilitated. Pt adatoms grown on graphene showed promising longevity of catalyst lifetime, owed to the formation of a covenant bonding between Pt and carbon of underlying graphene substrate, as suggested by EXAFS analysis.

Covering Pt with a single layer graphene enhanced catalyst durability with almost zero-losses of ECSA, as indicated by XPS and electrochemical CV after 1K ADT cycles. In addition, graphene capping did not negatively affect ORR activity, due to formation of hybrid graphene/Pt catalyst as showed by EXAFS and XPS analysis and reflected in maintaining no increase in ORR overpotential or reduction of current densities compared to graphene-cap-free counterparts. Pt adatoms sandwiched between two sets of graphene sheets showed further enhancement of catalyst stability. Capping

Pt with three atomic layers thick graphene boosted catalyst stability by surviving 74% of ECSA after 20K ADT cycles. Three atomic layers thick marked the optimal graphene-cap thickness. Thicker graphene layers (i.e. 5 layers) blocked ORR activity, however, stability was prolonged over 30K cycles. Five-layers thick graphene is plausible to provide a huge stability when used as a catalyst support instead of commercial carbon black. Degradation of catalyst activity was ascribed to Pt dissolution, which occurred during ADT. ADT induces point defects within graphene's structure through removal of carbon atoms. Point defects provide a tortuous path for Pt atoms to hop through towards the surface. DFT calculations suggested that Pt dissolution was activated by clustering of Pt at underneath the defect center, a Pt atom is trapped.

Replacing commercial carbon black with graphene is yet a problem to be resolved, as graphene's high surface area agitates restacking of graphene layers. Hence, effective ECSA drops down significantly. Therefore, more efforts have to be dedicated to modifying graphene's surface chemistry to hinder the restacking problem or by building 3D graphene support architectures (e.g. foam) on which metal catalyst adatoms can be synthesized.

5.6 Future Directions

Two distinctive routes can be followed to further investigate the role of 2D materials as a catalyst support and a protective cap for ORR catalyst materials for PEMFC applications. Frist direction is concerned with further investigation of hybridized 2D materials stacks (e.g. GR/hBN or GR/MXenes). Based on computational

analysis published elsewhere and outstanding findings from the presented thesis, strain tuning is a plausible route to enhance catalyst adatoms ORR activity. Support crystal structure and surface chemistry are two major factors influencing metal adatoms expitaxial growth. Hybrid 2D materials stacks showed significant effect on both electronic configuration and crystal structure of the top layer, which is going to form the expiatixal support from which metal adatom grows. Coupling of TMDCs, hBN or MXenes with graphene can induce compressive strain on Pt adatom, which leads to enhance their catalytic aptitude.

Second route is concerned with industrial scale optimization of GR/Pt/GR sandwich structure to produce a competitive MEA for PEMFC application. Synthesis of single atomically dispersed catalyst on 3D graphene structure is plausible to enhance mass activity, where larger surface area is obtained. Advancement in synthesis of graphene foam has been widely published in literature and briefly discussed by the presented thesis point out towards spending further efforts to modify graphene's surface chemistry though heteroatom doping. Precise and finely-tuned doping is essential to control defects concentration and distribution of heteroatom dopants of graphene. Higher concentration is desirable to maximize mass loading, however, increasing dopant concertation agitates ripening tendency, where catalyst single atoms are within close proximity relative to one-another shorter than critical diffusion length.

REFERENCES

1. Cox, P. M., Betts, R. A., Jones, C. D., Spall, S. A. & Totterdell, I. J. Acceleration of global warming due to carbon-cycle feedbacks in a coupled climate model. *Nature* (2000). doi:10.1038/35041539

2. Omar, M. M., Fawzy, S. M., El-Shabasy, A. B. & Allam, N. K. Large-diameter light-scattering complex multipodal nanotubes with graded refractive index: insights into their formation mechanism and photoelectrochemical performance. *J. Mater. Chem. A* (2017). doi:10.1039/C7TA08730F

3. Fawzy, S. M., Omar, M. M. & Allam, N. K. Photoelectrochemical water splitting by defects in nanostructured multinary transition metal oxides. *Sol. Energy Mater. Sol. Cells* (2019). doi:10.1016/j.solmat.2019.02.011

4. Abdelhafiz, A. A. *et al.* Defect engineering in 1D Ti-W oxide nanotube arrays and their correlated photoelectrochemical performance. *Phys. Chem. Chem. Phys.* (2018). doi:10.1039/c8cp01413b

5. Yang, L., Zuo, C., Wang, S., Cheng, Z. & Liu, M. A novel composite cathode for low-temperature SOFCs based on oxide proton conductors. *Adv. Mater.* (2008). doi:10.1002/adma.200702762

6. Xia, C. & Liu, M. Novel cathodes for low-temperature solid oxide fuel cells. *Adv. Mater.* (2002). doi:10.1002/1521-4095(20020404)14:7<521::AID-ADMA521>3.0.CO;2-C

7. Girishkumar, G., McCloskey, B., Luntz, A. C., Swanson, S. & Wilcke, W. Lithium-air battery: Promise and challenges. *J. Phys. Chem. Lett.* (2010). doi:10.1021/jz1005384

8. Tarascon, J. M. Key challenges in future Li-battery research. *Philosophical Transactions of the Royal Society A: Mathematical, Physical and Engineering Sciences* (2010). doi:10.1098/rsta.2010.0112

9. FUEL CELL TODAY. 'The Fuel Cell Industry Review 2012'. *Platin. Met. Rev.* (2012). doi:10.1595/147106712X657535

10. Vasileff, A., Zheng, Y. & Qiao, S. Z. Carbon Solving Carbon's Problems: Recent Progress of Nanostructured Carbon-Based Catalysts for the Electrochemical Reduction of CO2. *Advanced Energy Materials* **7**, (2017).

11. Todoroki, N., Asakimori, Y. & Wadayama, T. Effective shell layer thickness of platinum for oxygen reduction reaction alloy catalysts. *Phys. Chem. Chem. Phys.* (2013). doi:10.1039/c3cp53340a

12. Abdelhafiz, A., Vitale, A., Joiner, C., Vogel, E. & Alamgir, F. M. Layer-by-layer evolution of structure, strain, and activity for the oxygen evolution reaction in graphene-templated Pt monolayers. *ACS Appl. Mater. Interfaces* **7**, 6180–6188 (2015).

13. Eid, K. *et al.* Trimetallic PtPdRu Dendritic Nanocages with Three-Dimensional Electrocatalytic Surfaces. *J. Phys. Chem. C* **119**, 19947–19953 (2015).

14. Li, M. F. *et al.* Ultrafine jagged platinum nanowires enable ultrahigh mass activity for the oxygen reduction reaction. *Science (80-.).* **354**, 1414–1419 (2016).

15. He, Q. *et al.* Enhanced Pt stability in MO2(M = Ce, Zr or Ce0.9Zr0.1)-promoted Pt/C electrocatalysts for oxygen reduction reaction in PAFCs. *Appl. Catal. A Gen.* (2010). doi:10.1016/j.apcata.2010.03.044

16. Cheng, S., Rettew, R. E., Sauerbrey, M. & Alamgir, F. M. Architecture-dependent surface chemistry for Pt monolayers on carbon-supported Au. *ACS Appl. Mater. Interfaces* **3**, 3948–3956 (2011).

17. Shi, Y. C. *et al.* Dicationic ionic liquid mediated fabrication of Au@Pt nanoparticles supported on reduced graphene oxide with highly catalytic activity for oxygen reduction and hydrogen evolution. *Appl. Surf. Sci.* (2018). doi:10.1016/j.apsusc.2018.01.240

18. Park, H. Y., Park, J. H., Kim, P. & Yoo, S. J. Hollow PdCu2@Pt core@shell nanoparticles with ordered intermetallic cores as efficient and durable oxygen reduction reaction electrocatalysts. *Appl. Catal. B Environ.* (2018). doi:10.1016/j.apcatb.2017.11.052

19. Choi, S. *et al.* Catalytic behavior of metal catalysts in high-temperature RWGS reaction: In-situ FT-IR experiments and first-principles calculations. *Sci. Rep.* **7**, (2017).

20. Zheng, Y., Jiao, Y., Jaroniec, M., Jin, Y. & Qiao, S. Z. Nanostructured metal-free electrochemical catalysts for highly efficient oxygen reduction. *Small* (2012).

doi:10.1002/smll.201200861

21. Wu, L., Feng, H., Liu, M., Zhang, K. & Li, J. Graphene-based hollow spheres as efficient electrocatalysts for oxygen reduction. *Nanoscale* (2013). doi:10.1039/c3nr03794k

22. Abdelhafiz, A. *et al.* Epitaxial and atomically thin graphene–metal hybrid catalyst films: the dual role of graphene as the support and the chemically-transparent protective cap. *Energy Environ. Sci.* (2018). doi:10.1039/C8EE00539G

23. Nørskov, J. K. *et al.* Origin of the overpotential for oxygen reduction at a fuel-cell cathode. *J. Phys. Chem. B* (2004). doi:10.1021/jp047349j

24. Kulkarni, A., Siahrostami, S., Patel, A. & Nørskov, J. K. Understanding Catalytic Activity Trends in the Oxygen Reduction Reaction. *Chemical Reviews* (2018). doi:10.1021/acs.chemrev.7b00488

25. Rossmeisl, J., Karlberg, G. S., Jaramillo, T. & Nørskov, J. K. Steady state oxygen reduction and cyclic voltammetry. *Faraday Discuss.* (2009). doi:10.1039/b802129e

26. Pollet, B. G. *Power Ultrasound in Electrochemistry: From Versatile Laboratory Tool to Engineering Solution*. *Power Ultrasound in Electrochemistry: From Versatile Laboratory Tool to Engineering Solution* (2012). doi:10.1002/9781119967392

27. Quaino, P., Santos, E., Soldano, G. & Schmickler, W. Recent progress in hydrogen electrocatalysis. *Advances in Physical Chemistry* (2011). doi:10.1155/2011/851640

28. Marković, N. M., Adžić, R. R., Cahan, B. D. & Yeager, E. B. Structural effects in electrocatalysis: oxygen reduction on platinum low index single-crystal surfaces in perchloric acid solutions. *J. Electroanal. Chem.* (1994). doi:10.1016/0022-0728(94)03467-2

29. Yu, T., Kim, D. Y., Zhang, H. & Xia, Y. Platinum concave nanocubes with high-index facets and their enhanced activity for oxygen reduction reaction. *Angew. Chemie - Int. Ed.* (2011). doi:10.1002/anie.201007859

30. Abdelhafiz, A. *et al.* Epitaxial and atomically thin graphene-metal hybrid catalyst films: the dual role of graphene as the support and the chemically-transparent protective cap. *Energy Environ. Sci.* (2018). doi:10.1039/C8EE00539G

31. Zhang, H., Wang, H., Eid, K. & Wang, L. Nanoparticle in Nanocage: Au@Porous Pt Yolk-Shell Nanoelectrocatalysts. *Part. Part. Syst. Charact.* **32**, 863–868 (2015).

32. Eid, K. *et al.* Facile synthesis of porous dendritic bimetallic platinum-nickel nanocrystals as efficient catalysts for the oxygen reduction reaction. *Chem. - An Asian J.* **11**, 1388–1393 (2016).

33. Lu, S. *et al.* One-pot synthesis of PtIr tripods with a dendritic surface as an efficient catalyst for the oxygen reduction reaction. *J. Mater. Chem. A* **5**, 9107–9112 (2017).

34. Choi, S.-I. *et al.* Controlling the Size and Composition of Nanosized Pt–Ni Octahedra to Optimize Their Catalytic Activities toward the Oxygen Reduction Reaction. *ChemSusChem* **7**, 1476–1483 (2014).

35. Choi, S.-I. *et al.* Synthesis and Characterization of 9 nm Pt–Ni Octahedra with a Record High Activity of 3.3 A/mgPt for the Oxygen Reduction Reaction. *Nano Lett.* **13**, 3420–3425 (2013).

36. Sheng, W., Chen, S., Vescovo, E. & Shao-Horn, Y. Size Influence on the Oxygen Reduction Reaction Activity and Instability of Supported Pt Nanoparticles. *J. Electrochem. Soc.* (2012). doi:10.1149/2.009202jes

37. Shao, M., Peles, A. & Shoemaker, K. Electrocatalysis on platinum nanoparticles: Particle size effect on oxygen reduction reaction activity. *Nano Lett.* (2011). doi:10.1021/nl2017459

38. Wu, M. *et al.* Cu@Pt catalysts prepared by galvanic replacement of polyhedral copper nanoparticles for polymer electrolyte membrane fuel cells. *Electrochim. Acta* (2019). doi:10.1016/j.electacta.2019.03.111

39. Vitale, A., Murad, H., Abdelhafiz, A., Buntin, P. & Alamgir, F. M. Sandwiched Graphene Interdiffusion Barrier for Preserving Au@Pt Atomically Thin Core@Shell Structure and the Resulting Oxygen Reduction Reaction Catalytic Activity. *ACS Appl. Mater. Interfaces* (2019). doi:10.1021/acsami.8b17274

40. Jia, Q. *et al.* Activity descriptor identification for oxygen reduction on platinum-based bimetallic nanoparticles: In situ observation of the linear composition-strain-activity relationship. *ACS Nano* (2015). doi:10.1021/nn506721f

41. Jeon, T. Y. *et al.* Influence of oxide on the oxygen reduction reaction of carbon-supported Pt-Ni alloy nanoparticles. *J. Phys. Chem. C* (2009).

doi:10.1021/jp9076273

42. Stamenkovic, V. R. *et al.* Trends in electrocatalysis on extended and nanoscale Pt-bimetallic alloy surfaces. *Nat. Mater.* (2007). doi:10.1038/nmat1840

43. Song, J. *et al.* Surfactant-free room temperature synthesis of Pd x Pt y /C assisted by ultra-sonication as highly active and stable catalysts for formic acid oxidation. *Int. J. Hydrogen Energy* (2019). doi:10.1016/j.ijhydene.2019.03.169

44. Hwang, S. J. *et al.* Role of electronic perturbation in stability and activity of Pt-based alloy nanocatalysts for oxygen reduction. *J. Am. Chem. Soc.* (2012). doi:10.1021/ja307951y

45. Wang, Q., Cha, C. S., Lu, J. & Zhuang, L. The electrochemistry of ‘solid/water’ interfaces involved in PEM-H2O reactors: Part I. The ‘pt/water’ interfaces. *Phys. Chem. Chem. Phys.* (2009). doi:10.1039/b810429h

46. Wang, D. *et al.* Tuning oxygen reduction reaction activity via controllable dealloying: A model study of ordered Cu3Pt/C intermetallic nanocatalysts. *Nano Lett.* (2012). doi:10.1021/nl302404g

47. Stephens, I. E. L., Bondarenko, A. S., Grønbjerg, U., Rossmeisl, J. & Chorkendorff, I. Understanding the electrocatalysis of oxygen reduction on platinum and its alloys. *Energy and Environmental Science* (2012). doi:10.1039/c2ee03590a

48. Debe, M. K. *et al.* Extraordinary Oxygen Reduction Activity of Pt3Ni7. *J. Electrochem. Soc.* (2011). doi:10.1149/1.3595748

49. Guo, S. *et al.* FePt and CoPt nanowires as efficient catalysts for the oxygen reduction reaction. *Angew. Chemie - Int. Ed.* (2013). doi:10.1002/anie.201209871

50. Zhu, H., Zhang, S., Guo, S., Su, D. & Sun, S. Synthetic control of FePtM nanorods (M = Cu, Ni) to enhance the oxygen reduction reaction. *J. Am. Chem. Soc.* (2013). doi:10.1021/ja403041g

51. Rettew, R. E. *et al.* Near surface phase transition of solute derived Pt monolayers. in *Topics in Catalysis* **56**, 1065–1073 (2013).

52. Rettew, R. E., Guthrie, J. W. & Alamgir, F. M. Layer-by-Layer Pt Growth on Polycrystalline Au: Surface-Limited Redox Replacement of Overpotentially Deposited Ni Monolayers. *J. Electrochem. Soc.* **156**, D513 (2009).

53. Zhang, J., Vukmirovic, M. B., Xu, Y., Mavrikakis, M. & Adzic, R. R. Controlling the catalytic activity of platinum-monolayer electrocatalysts for oxygen reduction with different substrates. *Angew. Chemie - Int. Ed.* (2005). doi:10.1002/anie.200462335

54. Stolbov, S. & Zuluaga, S. Factors controlling the reactivity of catalytically active monolayers on metal substrates. *J. Phys. Chem. Lett.* (2013). doi:10.1021/jz4005174

55. Shao, M., Shoemaker, K., Peles, A., Kaneko, K. & Protsailo, L. Pt monolayer on porous Pd-Cu alloys as oxygen reduction electrocatalysts. *J. Am. Chem. Soc.* (2010). doi:10.1021/ja101966a

56. Stolbov, S. & Alcántara Ortigoza, M. Rational Design of Competitive

Electrocatalysts for Hydrogen Fuel Cells. *J. Phys. Chem. Lett.* **3**, 463–467 (2012).

57. Sasaki, K. *et al.* Highly stable Pt monolayer on PdAu nanoparticle electrocatalysts for the oxygen reduction reaction. *Nat. Commun.* (2012). doi:10.1038/ncomms2124

58. Gan, L., Heggen, M., Rudi, S. & Strasser, P. Core-shell compositional fine structures of dealloyed Pt(x)Ni(1-x) nanoparticles and their impact on oxygen reduction catalysis. *Nano Lett.* (2012). doi:10.1021/nl302995z

59. Liu, J. *et al.* High performance platinum single atom electrocatalyst for oxygen reduction reaction. *Nat. Commun.* (2017). doi:10.1038/ncomms15938

60. Sun, S. *et al.* Single-atom catalysis using Pt/graphene achieved through atomic layer deposition. *Sci. Rep.* (2013). doi:10.1038/srep01775

61. Choi, C. H. *et al.* Tuning selectivity of electrochemical reactions by atomically dispersed platinum catalyst. *Nat. Commun.* (2016). doi:10.1038/ncomms10922

62. Xie, P. *et al.* Nanoceria-Supported Single-Atom Platinum Catalysts for Direct Methane Conversion. *ACS Catal.* (2018). doi:10.1021/acscatal.8b00004

63. Yang, S., Tak, Y. J., Kim, J., Soon, A. & Lee, H. Support Effects in Single-Atom Platinum Catalysts for Electrochemical Oxygen Reduction. *ACS Catal.* (2017). doi:10.1021/acscatal.6b02899

64. Han, Y. *et al.* Hollow N-Doped Carbon Spheres with Isolated Cobalt Single Atomic Sites: Superior Electrocatalysts for Oxygen Reduction. *J. Am. Chem. Soc.* (2017). doi:10.1021/jacs.7b10194

65. Yang, L. *et al.* Unveiling the high-activity origin of single-atom iron catalysts for oxygen reduction reaction. *Proc. Natl. Acad. Sci.* (2018). doi:10.1073/pnas.1800771115

66. Li, F. *et al.* Boosting oxygen reduction catalysis with abundant copper single atom active sites. *Energy Environ. Sci.* (2018). doi:10.1039/C8EE01169A

67. An, B., Cheng, K., Wang, C., Wang, Y. & Lin, W. Pyrolysis of Metal-Organic Frameworks to Fe3O4@Fe5C2 Core-Shell Nanoparticles for Fischer-Tropsch Synthesis. *ACS Catal.* (2016). doi:10.1021/acscatal.6b00464

68. Park, Y. C., Tokiwa, H., Kakinuma, K., Watanabe, M. & Uchida, M. Effects of carbon supports on Pt distribution, ionomer coverage and cathode performance for polymer electrolyte fuel cells. *J. Power Sources* (2016). doi:10.1016/j.jpowsour.2016.02.091

69. Liu, Z. *et al.* Pt/graphene with intercalated carbon nanotube spacers introduced by electrostatic self-assembly for fuel cells. *Mater. Chem. Phys.* (2019). doi:10.1016/j.matchemphys.2018.12.100

70. Du, S., Lu, Y., Malladi, S. K., Xu, Q. & Steinberger-Wilckens, R. A simple approach for PtNi-MWCNT hybrid nanostructures as high performance electrocatalysts for the oxygen reduction reaction. *J. Mater. Chem. A* (2014). doi:10.1039/c3ta13608f

71. Yang, Z. *et al.* Sulfur-doped graphene as an efficient metal-free cathode catalyst for oxygen reduction. *ACS Nano* (2012). doi:10.1021/nn203393d

72. Soo, L. T., Loh, K. S., Mohamad, A. B., Daud, W. R. W. & Wong, W. Y. An overview of the electrochemical performance of modified graphene used as an electrocatalyst and as a catalyst support in fuel cells. *Applied Catalysis A: General* (2015). doi:10.1016/j.apcata.2015.03.008

73. Wu, J., Zhang, D., Wang, Y. & Wan, Y. Manganese oxide-graphene composite as an efficient catalyst for 4-electron reduction of oxygen in alkaline media. *Electrochim. Acta* (2012). doi:10.1016/j.electacta.2012.05.005

74. Yu, S. *et al.* Graphene–CeO2 hybrid support for Pt nanoparticles as potential electrocatalyst for direct methanol fuel cells. *Electrochim. Acta* (2013). doi:10.1016/j.electacta.2013.01.149

75. Liu, Y., Ishihara, A., Mitsushima, S., Kamiya, N. & Ota, K. Transition Metal Oxides as DMFC Cathodes Without Platinum. *J. Electrochem. Soc.* (2007). doi:10.1149/1.2734880

76. Takasu, Y., Suzuki, M., Yang, H., Ohashi, T. & Sugimoto, W. Oxygen reduction characteristics of several valve metal oxide electrodes in HClO4 solution. *Electrochim. Acta* (2010). doi:10.1016/j.electacta.2010.05.019

77. Yin, F., Takanabe, K., Kubota, J. & Domen, K. Polymerized Complex Synthesis of Niobium- and Zirconium-Based Electrocatalysts for PEFC Cathodes. *J. Electrochem. Soc.* (2010). doi:10.1149/1.3267041

78. Imai, H. *et al.* Structural defects working as active oxygen-reduction sites in partially oxidized Ta-carbonitride core-shell particles probed by using surface-sensitive

conversion-electron-yield x-ray absorption spectroscopy. *Appl. Phys. Lett.* (2010). doi:10.1063/1.3430543

79. Easton, E. B., Bonakdarpour, A., Yang, R., Stevens, D. A. & Dahn, J. R. Magnetron Sputtered Fe–C–N, Fe–C, and C–N Based Oxygen Reduction Electrocatalysts. *J. Electrochem. Soc.* (2008). doi:10.1149/1.2899013

80. Tauster, S. J., Fung, S. C. & Garten, R. L. Strong Metal-Support Interactions. Group 8 Noble Metals Supported on TiO2. *J. Am. Chem. Soc.* (1978). doi:10.1021/ja00469a029

81. Selvarani, G. *et al.* A methanol-tolerant carbon-supported pt-au alloy cathode catalyst for direct methanol fuel cells and its evaluation by DFT. *J. Phys. Chem. C* (2009). doi:10.1021/jp810970d

82. Liu, X. *et al.* Metals on graphene: Correlation between adatom adsorption behavior and growth morphology. *Phys. Chem. Chem. Phys.* (2012). doi:10.1039/c2cp40527j

83. He, H. & Gao, C. Graphene nanosheets decorated with Pd, Pt, Au, and Ag nanoparticles: Synthesis, characterization, and catalysis applications. *Sci. China Chem.* (2011). doi:10.1007/s11426-010-4191-9

84. Adzic, R. R. *et al.* Platinum monolayer fuel cell electrocatalysts. *Top. Catal.* (2007). doi:10.1007/s11244-007-9003-x

85. Tang, Y., Yang, Z. & Dai, X. Noble metals induced magnetic properties of graphene. *J. Magn. Magn. Mater.* (2011). doi:10.1016/j.jmmm.2011.05.004

86. Adzic, R. R. Platinum Monolayer Electrocatalysts: Tunable Activity, Stability, and Self-Healing Properties. *Electrocatalysis* (2012). doi:10.1007/s12678-012-0112-3

87. Huang, C., Li, C. & Shi, G. Graphene based catalysts. *Energy Environ. Sci.* (2012). doi:10.1039/c2ee22238h

88. MacHado, B. F. & Serp, P. Graphene-based materials for catalysis. *Catalysis Science and Technology* (2012). doi:10.1039/c1cy00361e

89. Li, M. *et al.* Ultrafine jagged platinum nanowires enable ultrahigh mass activity for the oxygen reduction reaction. *Science (80-.).* (2016). doi:10.1126/science.aaf9050

90. Salmi, Z. *et al.* Electroinduced Intercalation of Tetraalkylammonium Ions at the Interface of Graphene Grown on Copper, Platinum, and Iridium. *ChemElectroChem* (2016). doi:10.1002/celc.201600424

91. Lewera, A. *et al.* Core-level binding energy shifts in Pt-Ru nanoparticles: A puzzle resolved. *Chem. Phys. Lett.* (2007). doi:10.1016/j.cplett.2007.08.068

92. Zhao, X. *et al.* Simultaneous Improvements in Performance and Durability of an Octahedral PtNix/C Electrocatalyst for Next-Generation Fuel Cells by Continuous, Compressive, and Concave Pt Skin Layers. *ACS Catal.* (2017). doi:10.1021/acscatal.7b00964

93. Escudero-Escribano, M. *et al.* Tuning the activity of Pt alloy electrocatalysts by means of the lanthanide contraction. *Science (80-.).* (2016). doi:10.1126/science.aad8892

94. Lv, L. *et al.* A Universal Method to Engineer Metal Oxide-Metal-Carbon Interface for Highly Efficient Oxygen Reduction. *ACS Nano* (2018). doi:10.1021/acsnano.8b01056

95. Tian, X. *et al.* High-Performance Core-Shell Catalyst with Nitride Nanoparticles as a Core: Well-Defined Titanium Copper Nitride Coated with an Atomic Pt Layer for the Oxygen Reduction Reaction. *ACS Catal.* (2017). doi:10.1021/acscatal.7b00366

96. Chen, S. & Kucernak, A. Electrocatalysis under Conditions of High Mass Transport Rate: Oxygen Reduction on Single Submicrometer-Sized Pt Particles Supported on Carbon. *J. Phys. Chem. B* (2004). doi:10.1021/jp036831j

97. Heinzel, A. & Steele, B. C. Materials for fuel-cell technologies. *Nature* (2001).

98. Vogt, C., Monai, M., Kramer, G. J. & Weckhuysen, B. M. The renaissance of the Sabatier reaction and its applications on Earth and in space. *Nature Catalysis* (2019). doi:10.1038/s41929-019-0244-4

99. Shao, M., Chang, Q., Dodelet, J. P. & Chenitz, R. Recent Advances in Electrocatalysts for Oxygen Reduction Reaction. *Chemical Reviews* (2016). doi:10.1021/acs.chemrev.5b00462

100. Eid, K. *et al.* One-step solution-phase synthesis of bimetallic PtCo nanodendrites with high electrocatalytic activity for oxygen reduction reaction. *J. Electroanal. Chem.* (2015). doi:10.1016/j.jelechem.2015.10.035

101. Wei, C. *et al.* A Three-Dimensionally Structured Electrocatalyst: Cobalt-Embedded

Nitrogen-Doped Carbon Nanotubes/Nitrogen-Doped Reduced Graphene Oxide Hybrid for Efficient Oxygen Reduction. *Chem. - A Eur. J.* **23**, 637–643 (2017).

102. Song, J. *et al.* Surfactant-free room temperature synthesis of PdxPty/C assisted by ultra-sonication as highly active and stable catalysts for formic acid oxidation. *Int. J. Hydrogen Energy* **44**, 11655–11663 (2019).

103. Choi, S. Il *et al.* Synthesis and Characterization of 9-nm Pt-Ni Octahedra with a Record High Activity of 3.3 A/mgPt for the Oxygen Reduction Reaction. *Nano Lett.* online asap (2013).

104. Oezaslan, M., Hasche, F. & Strasser, P. Pt-Based Core-Shell Catalyst Architectures for Oxygen Fuel Cell Electrodes. *J. Phys. Chem. Lett.* **4**, 3273–3291 (2013).

105. Wu, M. *et al.* Cu@Pt catalysts prepared by galvanic replacement of polyhedral copper nanoparticles for polymer electrolyte membrane fuel cells. *Electrochim. Acta* **306**, 167–174 (2019).

106. Norskov, J. K., Bligaard, T., Rossmeisl, J. & Christensen, C. H. Towards the computational design of solid catalysts. *Nat Chem* **1**, 37–46 (2009).

107. Toyoda, E. *et al.* The d-band structure of Pt nanoclusters correlated with the catalytic activity for an oxygen reduction reaction. *J. Phys. Chem. C* (2011). doi:10.1021/jp206360e

108. Pang, J. *et al.* Direct synthesis of graphene from adsorbed organic solvent molecules over copper. *RSC Adv.* (2015). doi:10.1039/c5ra09405d

109. Limbu, T. B. *et al.* A Novel Approach to the Layer-Number-Controlled and Grain-Size-Controlled Growth of High Quality Graphene for Nanoelectronics. *ACS Appl. Nano Mater.* (2018). doi:10.1021/acsanm.7b00410

110. Kim, K. *et al.* Raman spectroscopy study of rotated double-layer graphene: Misorientation-angle dependence of electronic structure. *Phys. Rev. Lett.* (2012). doi:10.1103/PhysRevLett.108.246103

111. Ogasawara, H. & Ito, M. Hydrogen adsorption on Pt(100), Pt(110), Pt(111) and Pt(1111) electrode surfaces studied by in situ infrared reflection absorption spectroscopy. *Chem. Phys. Lett.* (1994). doi:10.1016/0009-2614(94)00247-9

112. Zhang, L. *et al.* Platinum-based nanocages with subnanometer-thick walls and well-defined, controllable facets. *Science (80-.).* **349**, 412–416 (2015).

113. Kim, J. *et al.* Highly Durable Platinum Single-Atom Alloy Catalyst for Electrochemical Reactions. *Adv. Energy Mater.* (2018). doi:10.1002/aenm.201701476

114. Yang, S., Kim, J., Tak, Y. J., Soon, A. & Lee, H. Single-atom catalyst of platinum supported on titanium nitride for selective electrochemical reactions. *Angew. Chemie - Int. Ed.* (2016). doi:10.1002/anie.201509241

115. Zhou, M., Dick, J. E. & Bard, A. J. Electrodeposition of Isolated Platinum Atoms and Clusters on Bismuth - Characterization and Electrocatalysis. *J. Am. Chem. Soc.* (2017). doi:10.1021/jacs.7b10646

116. Zheng, X. *et al.* The Raman redshift of graphene impacted by gold nanoparticles. *AIP Adv.* (2015). doi:10.1063/1.4921316

117. Ganesan, K. *et al.* A comparative study on defect estimation using XPS and Raman spectroscopy in few layer nanographitic structures. *Phys. Chem. Chem. Phys.* (2016). doi:10.1039/c6cp02033j

118. Hodkiewicz, J. Characterizing Graphene with Raman Spectroscopy. *Thermo Sci.* (2010). doi:10.1371/journal.pcbi.1002542

119. Eckmann, A. *et al.* Probing the nature of defects in graphene by Raman spectroscopy. *Nano Lett.* (2012). doi:10.1021/nl300901a

120. Lucchese, M. M. *et al.* Quantifying ion-induced defects and Raman relaxation length in graphene. *Carbon N. Y.* (2010). doi:10.1016/j.carbon.2009.12.057

121. Cançado, L. G. *et al.* Quantifying defects in graphene via Raman spectroscopy at different excitation energies. *Nano Lett.* (2011). doi:10.1021/nl201432g

122. Martins Ferreira, E. H. *et al.* Evolution of the Raman spectra from single-, few-, and many-layer graphene with increasing disorder. *Phys. Rev. B - Condens. Matter Mater. Phys.* (2010). doi:10.1103/PhysRevB.82.125429

123. Kresse, G. & Hafner, J. *Ab initio* molecular dynamics for liquid metals. *Phys. Rev. B* (1993). doi:10.1103/PhysRevB.47.558

124. Kresse, G. & Hafner, J. Ab initio molecular-dynamics simulation of the liquid-metalamorphous- semiconductor transition in germanium. *Phys. Rev. B* (1994).

doi:10.1103/PhysRevB.49.14251

125. Perdew, J. P., Burke, K. & Ernzerhof, M. Generalized gradient approximation made simple. *Phys. Rev. Lett.* (1996). doi:10.1103/PhysRevLett.77.3865

126. Grimme, S. Semiempirical GGA-type density functional constructed with a long-range dispersion correction. *J. Comput. Chem.* (2006). doi:10.1002/jcc.20495

127. Joubert, D. From ultrasoft pseudopotentials to the projector augmented-wave method. *Phys. Rev. B - Condens. Matter Mater. Phys.* (1999). doi:10.1103/PhysRevB.59.1758

128. Banhart, F., Kotakoski, J. & Krasheninnikov, A. V. Structural defects in graphene. *ACS Nano* (2011). doi:10.1021/nn102598m

129. Zhang, W. *et al.* Migration of gold atoms in graphene ribbons: Role of the edges. *Phys. Rev. B - Condens. Matter Mater. Phys.* (2010). doi:10.1103/PhysRevB.81.125425

130. Tang, Y. *et al.* The electronic and diffusion properties of metal adatoms on graphene sheets: A first-principles study. *RSC Adv.* (2017). doi:10.1039/c7ra04519k

131. Hardcastle, T. P. *et al.* Mobile metal adatoms on single layer, bilayer, and trilayer graphene: An ab initio DFT study with van der Waals corrections correlated with electron microscopy data. *Phys. Rev. B - Condens. Matter Mater. Phys.* (2013). doi:10.1103/PhysRevB.87.195430

132. Gan, Y., Sun, L. & Banhart, F. One- and two-dimensional diffusion of metal atoms

in graphene. *Small* **4**, 587–591 (2008).

133. Toda, T., Igarashi, H. & Watanabe, M. Role of Electronic Property of Pt and Pt Alloys on Electrocatalytic Reduction of Oxygen. *J. Electrochem. Soc.* **145**, 4185–4188 (1998).

134. Tao, L. *et al.* Edge-rich and dopant-free graphene as a highly efficient metal-free electrocatalyst for the oxygen reduction reaction. *Chem. Commun.* (2016). doi:10.1039/c5cc09173j

135. Liu, J., Takeshi, D., Sasaki, K. & Lyth, S. M. Defective Graphene Foam: A Platinum Catalyst Support for PEMFCs. *J. Electrochem. Soc.* (2014). doi:10.1149/2.0231409jes

136. Pu, N. W. *et al.* Dispersion of graphene in aqueous solutions with different types of surfactants and the production of graphene films by spray or drop coating. *J. Taiwan Inst. Chem. Eng.* (2012). doi:10.1016/j.jtice.2011.06.012

137. Uddin, M. E. *et al.* Effects of various surfactants on the dispersion stability and electrical conductivity of surface modified graphene. *J. Alloys Compd.* (2013). doi:10.1016/j.jallcom.2013.01.127

138. Zambelli, T., Wintterlin, J., Trost, J. & Ertl, G. Identification of the 'active sites' of a surface-catalyzed reaction. *Science (80-.).* (1996). doi:10.1126/science.273.5282.1688

139. Patrone, P. N., Einstein, T. L. & Margetis, D. From atoms to steps: The microscopic

origins of crystal evolution. *Surf. Sci.* (2014). doi:10.1016/j.susc.2014.02.015

140. Jiang, T. *et al.* Trends in CO oxidation rates for metal nanoparticles and close-packed, stepped, and kinked surfaces. *J. Phys. Chem. C* (2009). doi:10.1021/jp811185g

141. Dahl, S. *et al.* Role of steps in N2 activation on Ru(0001). *Phys. Rev. Lett.* (1999). doi:10.1103/PhysRevLett.83.1814